

C.2

72

CANADA • Inland Waters Directorate
72 SCIENTIFIC SERIES

72 (C2)

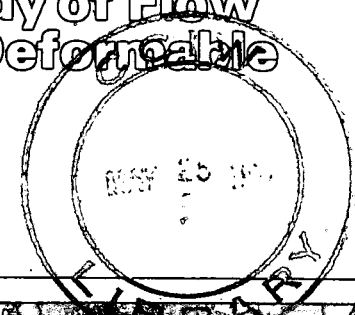


Fisheries
and Environment
Canada

Pêches
et Environnement
Canada

A Numerical, Field and Laboratory Study of Flow in Rocks with Deformable Fractures

John Edward Gale



A NUMERICAL, FIELD AND LABORATORY STUDY OF FLOW IN ROCKS WITH DEFORMABLE FRACTURES

GALE

SCIENTIFIC SERIES NO. 72
(Résumé en français)

INLAND WATERS DIRECTORATE,
WATER RESOURCES BRANCH,
OTTAWA, CANADA, 1977.

GB
707
C335
no. 72
c.2



Fisheries
and Environment
Canada

Pêches
et Environnement
Canada

A Numerical, Field and Laboratory Study of Flow in Rocks with Deformable Fractures

John Edward Gale

SCIENTIFIC SERIES NO. 72
(Résumé en français)

**INLAND WATERS DIRECTORATE,
WATER RESOURCES BRANCH,
OTTAWA, CANADA, 1977.**

© Minister of Supply and Services Canada 1978

Cat. No. EM36-502/72

ISBN 0-662-01805-2

Contract No. KL229-7-1040

THORN PRESS LIMITED

Contents

	Page
ACKNOWLEDGMENTS.....	xi
ABSTRACT.....	xiii
RÉSUMÉ.....	xv
NOMENCLATURE.....	xvii
CONVERSION FACTORS.....	xix
1. INTRODUCTION.....	1
Description of problem.....	1
Objectives and scope.....	3
Previous work.....	4
Flow in fractured rocks.....	4
Experimental work on flow in fractures.....	8
Fracture deformation.....	10
2. THEORY OF FLUID FLOW IN DEFORMABLE FRACTURE SYSTEMS.....	12
Introduction.....	12
Governing equations.....	13
Flow in a single fracture - the parallel plate analogy.....	13
Flow in a fracture system.....	16
Stress and strain analysis of a fractured rock mass.....	18
Rock blocks.....	18
Fractures.....	19
Finite-element formulation.....	22
Method of weighted residuals.....	22
Application of the Galerkin method.....	25
Procedure for analyzing flow in deformable fracture systems.....	33
General approach.....	33
Results from a simple axisymmetric model.....	36
Fluid injection and fluid withdrawal in a deformable fracture system.....	40
Fluid pressure distributions and flow rates in a horizontal fracture system.....	40
Fluid pressure distributions and flow rates in a vertical fracture system.....	43
Effects of nonuniform fracture apertures.....	49
3. FIELD MEASUREMENTS OF FRACTURE DEFORMATION DUE TO FLUID PRESSURE CHANGES.....	54
Introduction.....	54
Study area and fracture system.....	54
Location and description.....	54
Geology.....	55
Surface measurements.....	56
Downhole measurements.....	59
Material properties.....	64
Hydraulic characteristics.....	66
Injection tests.....	66
Calculated equivalent fracture apertures.....	73
Distribution of fluid pressures in the fracture plane.....	77
Constant flow rate injection test.....	83
Withdrawal tests.....	85

Contents (cont.)

	Page
Aperture deformation resulting from fluid pressure changes.....	86
Withdrawal test.....	87
Injection tests.....	89
4. NUMERICAL SIMULATION OF THE FRACTURE SYSTEM AT SAMBRO, NOVA SCOTIA.....	99
Comparison of measured changes in fracture apertures with numerical model results.....	99
Effect of fracture deformation and fracture location on simulated pump test results.....	103
Summary.....	109
5. LABORATORY STUDY OF INJECTION AND WITHDRAWAL TESTS USING LARGE-DIAMETER ROCK CORES.....	111
Introduction.....	111
Description of experiment.....	111
Sample preparation.....	111
Material properties.....	114
Test procedure - sample instrumentation.....	115
Results of fluid injection and withdrawal tests.....	120
Saw-cut fracture surface - "uniform aperture".....	121
Saw-cut and sandblasted fracture surface - "nonuniform aperture".....	124
Tension fracture and nonuniform fracture.....	127
Tension fracture.....	130
Summary.....	132
6. SUMMARY AND CONCLUSIONS.....	134
REFERENCES.....	137
APPENDIX. PROPOSED MODIFICATION OF INFLATABLE PACKER ASSEMBLY FOR DETERMINING THE PERMEABILITY PROFILE OF A WELL.....	144

Tables

1. Results from injection and withdrawal in a simple axisymmetric model..	39
2. Flow rates for injection and withdrawal in an orthogonal fracture system with different fracture stiffness values.....	47
3. Flow rates for equivalent uniform and nonuniform fracture apertures...	52
4. Flow rates for fluid injection in the nonuniform and equivalent uniform fracture apertures.....	53
5. Pressure and flow rate data and calculated equivalent uniform apertures for injection tests in well S1.....	70
6. Pressure and flow rate data from wells S4, S6 and S7.....	74
7. Fracture data and equivalent fracture apertures for selected fractures at Sambro.....	78

Tables (cont.)

	Page
8. Nonuniform fracture apertures calculated from injection test results..	83
9. <i>In situ</i> fracture deformation test data, September 14, 1973.....	91
10. Pressure history test data for fracture deformation test, September 14, 1973.....	92
11. Comparison of field measurements and numerical model results of fracture deformation for the fracture at the 29-ft level.....	104
12. Comparison of field measurements and numerical model results of fracture deformation for the fracture at the 20-ft level.....	105
13. Properties of the fracture system used in simulated pump tests.....	106
14. Results of simulated pump test with nonuniform apertures.....	106
15. Results of simulated pump test with nonuniform apertures with fractures at 10-ft and 40-ft levels interchanged.....	107
16. Results of simulated pump test with equivalent uniform apertures.....	107
17. Results of simulated pump test with equivalent uniform apertures with fractures at 10-ft and 40-ft levels interchanged.....	108
18. Results of cyclic compression tests on Sierra White Granite.....	115

Illustrations

Figure 1. Typical results of field water tests.....	2
Figure 2. Flow in a single fracture.....	14
Figure 3. Flow in a fracture with parallel sides.....	17
Figure 4. Joint element of Goodman, Taylor and Brekke (1968).....	20
Figure 5. Constitutive model for displacement of a joint under normal stress.....	21
Figure 6. Constitutive model for displacement of a joint under shear stress.....	22
Figure 7. Triangular element.....	24
Figure 8. Line element.....	26
Figure 9. Axisymmetric element showing stress and strain components.....	29
Figure 10. Flow chart for coupled stress-flow analysis.....	35
Figure 11. Simple axisymmetric model.....	37

Illustrations (cont.)

	Page
Figure 12. Finite-element model.....	41
Figure 13. Comparison of flow rates for fluid injection and withdrawal in a fracture system for two different fracture strengths.....	42
Figure 14. Fluid pressure profiles for fluid injection and withdrawal in rigid and deformable fracture systems.....	43
Figure 15. Distribution of stresses in a rock mass containing two vertical orthogonal fracture sets (withdrawal).....	45
Figure 16. Distribution of stresses in a rock mass containing two vertical orthogonal fracture sets (injection).....	45
Figure 17. Comparison of fluid pressure distribution along the centre fracture for injection and withdrawal in rigid and deformable orthogonal fracture systems.....	46
Figure 18. Distribution of fluid pressure for fluid injection and fluid withdrawal in a slightly deformable orthogonal fracture system.....	46
Figure 19. Effect of fracture intersection angle on pressure distribution.	48
Figure 20. Schematic of pressure profiles for flow in pipes with equivalent uniform and nonuniform cross sections.....	49
Figure 21. Fluid pressure profiles for injection and withdrawal in fractures with uniform and nonuniform apertures.....	50
Figure 22. Fracture deformation owing to fluid injection and fluid withdrawal in uniform and nonuniform fracture apertures.....	50
Figure 23. Fluid pressure profiles and changes in fracture apertures owing to fluid injection (+3,264 psf) in uniform and nonuniform fracture apertures.....	52
Figure 24. Study area.....	55
Figure 25. Bedrock exposure at Sambro test site showing preferred orientation of feldspar phenocrysts.....	56
Figure 26. General topography of Sambro area.....	57
Figure 27. Upper hemisphere equal-area polar projection of poles to fracture planes measured in Sambro area.....	58
Figure 28. Plane-table map of Sambro test site.....	58
Figure 29. Fracture log for well S1.....	60
Figure 30. Fracture log for well S2.....	61
Figure 31. Fracture logs for wells S4, S5, S6 and S7.....	62

Illustrations (cont.)

	Page
Figure 32. Detailed borehole periscope observations of fractures at 13-ft level in wells S1 and S2.....	63
Figure 33. Load-displacement curve for a sample of the quartz monzonite porphyry.....	65
Figure 34. Load-displacement curve for a sample of the fine-grained quartz monzonite.....	65
Figure 35. Close-up view of core from 9.36 ft below ground surface in well S1.....	66
Figure 36. Schematic of injection test.....	67
Figure 37. Packer arrangements for injection tests.....	67
Figure 38. Calibration curves for flow manometers.....	68
Figure 39. Pressure transducer equipment.....	69
Figure 40. Fluid pressures in various fracture planes.....	72
Figure 41. Fluid temperature profiles measured at beginning of field season.....	73
Figure 42. Flow from cavity to fracture.....	75
Figure 43. Percentage change in hydraulic head for laminar axisymmetric flow from borehole.....	79
Figure 44. Distribution of fluid pressures in the fracture plane.....	81
Figure 45. Pressure-time data for constant flow rate injection test.....	84
Figure 46. Pump test data.....	86
Figure 47. Results of fracture deformation measurements during withdrawal test.....	88
Figure 48. Results from an injection test in well S1 with the fracture deformation gauge locked across the fracture at the 29-ft level in S1.....	90
Figure 49. Results from an injection test in well S2 with the fracture deformation gauge locked across the fracture at the 20-ft level in S1.....	95
Figure 50. Results from an injection test in well S1 with the fracture deformation gauge locked across the fracture at the 20-ft level in S1.....	96
Figure 51. Finite-element model of fracture system at Sambro.....	100
Figure 52. Force (fluid pressure) - normal displacement relationships determined from field data for fractures at 29-ft and 20-ft levels.....	102

Illustrations (cont.)

	Page
Figure 53. Drawdown data measured in the pumping well during two separate pumping tests on two separate wells.....	109
Figure 54. Granite core (38-in. diameter) at Cold Springs Co. quarry near Raymond, California.....	112
Figure 55. Both halves of 38-in. diameter core showing anchor and splitting holes.....	113
Figure 56. Schematic diagram of core showing location of centre hole and four LVDTs.....	113
Figure 57. Location of splitting holes and reference guides for rematching tension fracture.....	114
Figure 58. Partial stress-strain curve for sample No. 1.....	116
Figure 59. Complete stress-strain curve for three samples of Sierra White Granite from Raymond, California.....	116
Figure 60. Large-diameter core prepared for testing.....	117
Figure 61. Close-up of LVDT mounted across saw-cut fracture.....	118
Figure 62. Large-diameter core ready for assembly in triaxial cell.....	119
Figure 63. Schematic of sandblasted saw-cut fracture surface in nonuniform aperture.....	120
Figure 64. Fracture and rock deformation in saw-cut fracture surface.....	121
Figure 65. Changes in flow rate and fracture aperture as a function of effective stress in saw-cut fracture surface.....	122
Figure 66. Changes in flow rate and fracture aperture for different injection and withdrawal pressures with a constant axial stress of 200 psi in saw-cut fracture surface.....	123
Figure 67. Percentage of pressure measured at 5 in. from edge of centre borehole for different injection and withdrawal pressures.....	124
Figure 68. Fracture and rock deformation in sandblasted saw-cut surface...	125
Figure 69. Changes in flow rate and fracture aperture as a function of effective stress in sandblasted saw-cut fracture surface.....	125
Figure 70. Changes in flow rate and fracture aperture for different injection and withdrawal pressures with a constant axial stress of 200 psi in sandblasted saw-cut surface.....	126
Figure 71. Tension fracture.....	127
Figure 72. Fracture and rock deformation in tension fracture.....	128

Illustrations (cont.)

	Page
Figure 73. Changes in flow rate and fracture aperture as a function of effective stress in both tension and sandblasted saw-cut fractures.....	129
Figure 74. Changes in flow rate and fracture aperture for different injection and withdrawal pressures with a constant axial stress of 200 psi in tension fracture and sandblasted saw-cut fracture	129
Figure 75. Percentage of pressure measured at 5 in. from edge of centre borehole for different injection and withdrawal pressures.....	130
Figure 76. Change in flow rate and fracture aperture as a function of effective stress in tension fracture only.....	131
Figure 77. Changes in flow rate and fracture aperture for different injection and withdrawal pressures and a constant axial stress of 200 psi in tension fracture only.....	131
Figure 78. Percentage of pressure measured at 5 in. from edge of centre borehole for different injection and withdrawal pressures.....	132

Acknowledgments

The author wishes to express his appreciation of the support and encouragement provided by Professor P.A. Witherspoon during all phases of this Ph.D. study at the University of California, Berkeley. His active interest contributed significantly to the successful outcome of this research program. Professor D.T. Snow strongly encouraged the author in his attempts at the seemingly impossible task of obtaining *in situ* field measurements. Professor Snow's interest in the outcome of the entire research program is greatly appreciated. The assistance of Professor R.L. Taylor was essential to the successful completion of the numerical investigations.

The author owes special thanks to J. A. Welhan for his indispensable help and contributions in the preparation for and during the field program. The author also wishes to thank P. Delaney, I. Gale and H. Cross for their assistance in the field. With respect to instrument development and fabrication, the assistance and contributions of the personnel of the Instrumentation Section, Inland Waters Directorate, Department of Fisheries and the Environment, especially those of J. Kruus, are gratefully acknowledged. The author extends his sincere thanks to C. Chan and M. Brock for their help and advice during the laboratory phase of this study.

At Berkeley, the author benefited considerably from the suggestions and constructive criticisms of friends and colleagues, especially T. Maini, M. Lippman, T.N. Narasimhan and D. Watkins. The author wishes to thank W. Quitiquit, E. McKeon and D. Honigman as well as the secretarial staff of the Department of Fisheries and the Environment, particularly G. Blackwood, for their assistance in typing the manuscript. The patience and careful drafting of the figures by G. Pelatowski are greatly appreciated.

The author gratefully acknowledges the generous financial support of the field program and the author's studies by the Hydrology Research Division, Department of Fisheries and the Environment. Financial assistance was also received from the Jane Lewis Fellowship and Geological Engineering Foundation funds. The laboratory phase of this report was supported under research Contract No. 14-08-0001-14583 from the United States Geological Survey to Professor P.A. Witherspoon.

Abstract

The main objectives of this study were to determine whether fractures open or close because of changes in fluid pressure and what effect such changes in fracture aperture might have on fluid pressure distributions and flow rates within the fracture system. The research program consisted of (1) numerical, (2) field and (3) laboratory studies.

A numerical model is presented that simulates the steady-state interaction of fluid pressures and stresses in fractured rock masses. This simulation requires the combination of two nonlinear equations and the use of two finite-element techniques, one for fluid flow in fractures and the other for stress analysis of the jointed rock mass. The finite-element formulations are developed directly from the appropriate governing equations using the Galerkin method.

The numerical model can simulate general two-dimensional plane strain problems in either vertical or horizontal sections as well as the axisymmetric case of flow to a well intersecting a system of horizontal fractures. Model studies with idealized fracture systems showed that fractures open during injection and close during withdrawal and that injection rates are much greater than the withdrawal rates for corresponding pressure gradients. Also, the model studies showed that because of the difference in fluid pressure distribution, fractures with nonuniform apertures cannot be replaced with a system of fractures having equivalent uniform apertures.

A borehole instrument (fracture deformation gauge) was developed and used to make *in situ* measurements of the changes in individual fracture apertures during fluid injection and withdrawal tests at Sambro, Nova Scotia. For a fracture located 29 ft below the ground surface a decrease in fluid pressure of ≈ 7.5 psi gave a fracture closure of $\approx 5 \times 10^{-5}$ ft. The same fracture opened by $\approx 3 \times 10^{-4}$ ft on account of an increase in fluid pressure of ≈ 20 psi. Very good agreement was obtained between the field measurements and the results of a numerical model study of the test site. It is shown that the fracture deformation gauge can be used to obtain *in situ* measures of the normal stiffness values (K_N) of individual fractures.

Laboratory measurements of changes in fracture apertures owing to changes of fluid pressure verified the numerical and field results. It is shown that the fluid pressure profile within a fracture plane is very sensitive to fracture opening and closing, and thus may provide an indirect means of detecting fracture deformation in field situations.

Résumé

Dans la présente étude, on se propose essentiellement de déterminer si des fractures peuvent s'ouvrir ou se fermer lorsque la pression exercée par des fluides varie, et d'évaluer les effets que ces variations d'ouverture des fractures pourraient avoir sur la répartition de la pression des fluides et les vitesses d'écoulement à l'intérieur du réseau de fractures. Le programme de recherche consiste en des études (1) numériques, (2) effectuées sur le terrain et (3) en laboratoire.

On présente ici un modèle numérique, qui simule l'interaction en régime permanent des pressions exercées par les fluides, et des contraintes qui existent dans les masses rocheuses fracturées. Pour cette simulation, il est nécessaire de combiner deux équations non linéaires et d'utiliser deux techniques différentes des éléments finis, l'une applicable à l'écoulement fluide dans les fractures, et l'autre à l'analyse des contraintes dans la masse rocheuse diaclasée. La formulation des éléments finis est établie directement à partir des équations directrices appropriées, par la méthode de Galerkin.

Le modèle numérique peut simuler des problèmes généraux de contraintes planes (bidimensionnelles), dans des coupes verticales ou horizontales, ainsi que des problèmes d'écoulement autour d'un puits traversant un réseau de fractures horizontales (modèle avec symétrie par rapport à un axe). Les études de modèles effectuées sur des réseaux de fractures idéalisés ont démontré que les fractures s'ouvrent au cours de l'injection et se ferment au cours du retrait, et que les vitesses d'injection sont bien supérieures aux vitesses de retrait, aux gradients de pression correspondants. En outre, les études de ces modèles ont indiqué qu'il est impossible de remplacer un réseau de fractures à ouvertures non uniformes par un réseau de fractures à ouvertures uniformes équivalentes, en raison des différences de répartition de la pression des fluides.

On a mis au point un appareil de sondage (jauge de déformation des fractures), et on l'a utilisé pour effectuer des mesures sur le terrain des variations d'ouverture des fractures individuelles, au cours des tests d'injection et de retrait des fluides réalisés à Sambro (Nouvelle-Écosse). Dans le cas d'une fracture située à 29 pi au-dessous de la surface du sol, une diminution de ≈ 7.5 psi de la pression des fluides a provoqué une fermeture des fractures de $\approx 5 \times 10^{-5}$ pi. La même fracture s'est ouverte de $\approx 3 \times 10^{-4}$ pi, par suite d'une augmentation de ≈ 20 psi de la pression des fluides. On a observé une excellente concordance entre les mesures effectuées sur le terrain, et les résultats obtenus par étude

numérique d'un modèle du site expérimental. On démontre ainsi qu'il est possible d'utiliser la jauge de déformation des fractures pour obtenir des mesures sur le terrain des valeurs normales de rigidité (K_N) des fractures individuelles.

Les mesures effectuées en laboratoire, des variations d'ouverture des fractures engendrées par des variations de pression des fluides, ont confirmé les résultats obtenus des études numériques et sur le terrain. On a ainsi démontré que le profil de pression des fluides à l'intérieur d'un plan de fractures réagit très rapidement à l'ouverture et à la fermeture des fractures, ce qui peut constituer une méthode indirecte de détection sur le terrain de la déformation des fractures.

Nomenclature

$A ()$	Linear operator	k	Hydraulic conductivity of fracture
$[B]$	Submatrix of stiffness matrix	k_p	Area permeability
$[B_j]$	Submatrix of joint stiffness matrix	L	Length, also denotes fracture length
b	One-half fracture aperture	ℓ	Incremental distance along fracture
b^0	One-half initial fracture aperture	$[N]$	Two-dimensional element shape function
C	Cohesion	NN	Number of structural nodal points
$[D]$	Moduli matrix	NP	Number of flow nodal points
$\frac{D ()}{Dt}$	Total derivative	n_x, n_y	Direction cosines of the outward normals
ds	Elemental boundary	$\{P\}$	Fluid pressure at flow nodal points
dv	Elemental region	P_1	Fluid pressure in centre borehole
E	Young's modulus	P_2	Fluid pressure surrounding rock sample
$\{F\}$	Force vector	P_I	Injection pressure
f_i	Components of body force per unit mass	P_W	Withdrawal pressure
g	Acceleration owing to gravity	ΔP	Pressure differential ($= P_1 - P_2$)
H	Hydraulic head	p	General fluid pressure term
H_b	Hydraulic head on the boundary	p^m	Fluid pressure distribution within fracture system
H_w	Hydraulic head in the borehole	Q	Measured flow rate
I	Identity matrix	Q_D	Flow rate in deformable fracture
i, j, k, ℓ	Nodal points	Q_R	Flow rate in rigid fracture
$[K]$	Stiffness matrix	q	Flow rate in fractures
$[K]^e$	Element stiffness matrix	\bar{q}	Prescribed flow rate
$[K]^r$	Stiffness matrix for rock block	R	Residual
$[K_f]$	Fluid conductivity matrix	r	Radial coordinate
$[K_j]$	Joint moduli matrix	r_b	Radial distance to flow boundary or radius of influence
K_N	Normal stiffness: ratio of the normal force acting on a joint to the normal displacement across the joint	r_w	Radius of well
K_p	Fracture flow term when expressed in terms of pressure gradients	S	Total surface area
K_S	Shear stiffness: ratio of the shear stress acting on the joint to the shear displacement along the joint	S_p	Surface on which fluid pressure or flow rates are prescribed
		S_t	Surfaces on which stresses are

	prescribed; include interior surfaces where fluid pressures are applied	α_i	Linear interpolation constants ($i = 1$ to 6)
S_u	Surface area over which displacement is specified	γ_f	Specific weight of fluid
T	Time, or transpose (when used as superscript)	γ_{rz}	Shear strain, polar coordinates
$\{t\}$	Traction forces, including fluid pressure effects on the rock surface	γ_{xy}	Shear strain, Cartesian coordinates
$\{t_0\}$	Initial traction forces	Δ	Area of triangle
\bar{t}	Prescribed traction forces	$\Delta 2b$	Change in fracture aperture
$\{t_B\}$	Traction forces acting on the bottom side of the joint element	δ	Nodal point displacements
$\{t_T\}$	Traction forces acting on the top side of the joint element	δ_R	Displacement because of rock strain
$\{u\}$	Displacement vector	δ^g	Displacement owing to gravity
\bar{u}	Prescribed displacements	δ^n	Initial displacements
u_s	Displacement parallel to the joint plane	$\{\delta\}^e$	Nodal point displacements
u^T	Transpose of displacement vector	ϵ	Strain
$u(x,y)$	Displacement in x direction	$[\epsilon]$	General form of the strain tensor
$v(x,y)$	Displacement in y direction	μ	Dynamic viscosity of fluid
V	Region of interest	ν	(1) Kinematic viscosity (2) Poisson's ratio
V_a	Average fluid velocity	ρ_f	Fluid density
V_i	Velocity components in the coordinate directions ($i = 1, 2, 3$)	ρ_s	Density of rock blocks
V_p	Domain of the fluid	σ	Stress
V_u	Domain of the rock mass	$[\sigma]$	General form of the stress tensor
v_n	Displacements perpendicular to the joint plane	σ_0	Residual stresses
W_i	Weighting function	$[\sigma^0]$	Initial stress tensor
X_1, X_2, X_3	Global coordinates; X_3 axis parallel to the direction in which the gravity force acts	σ_e	Effective normal stress
x_1, x_2, x_3	Local coordinates; axis directions related to fracture orientations	σ_n	Normal stress
(X_i, Y_i)	Global coordinates of flow or structural nodal point i	τ	Shear stress
(x'_i, y'_i)	Local coordinates of flow nodal point i	τ_f	Shear stress at failure
z	Vertical coordinate in axisymmetric systems	τ_{rz}	Shear stress, polar coordinates
		τ_{xy}	Shear stress, Cartesian coordinates
		ϕ	(1) Force potential (2) Shape function for flow elements
		ϕ	Angle of friction in the fracture plane
		∇	Gradient operator
		$\nabla \cdot ()$	Divergence of ()
		∇^2	Laplacian operator

Conversion Factors

The units of measurement used in this report can be converted to Standard International (SI) units in the following way.

<u>Multiply</u>	<u>By</u>	<u>To Obtain</u>
Inches	2.540	centimetres
Feet	0.305	metres
Miles	1.700	kilometres
Square inches	6.45	square centimetres
Square feet	0.093	square metres
Cubic inches	16.4	cubic centimetres
Cubic feet	0.028	cubic metres
Gallon (U.S.)	3.80	litres
Pounds	0.454	kilograms
Tons	907.2	kilograms
One-pound force	4.45	newtons
Pounds per square foot	47.9	newtons per square metre
Pounds per square inch	6.9	kilonewtons per square metre

Introduction

DESCRIPTION OF PROBLEM

In metamorphic and crystalline rock masses, fractures (discontinuities) represent the primary flow paths. Fractures generally occur in sets, and most fractured rock masses contain at least two or three fracture sets. In many parts of the world fractured rock aquifers are the main source of domestic groundwater supplies. Production from individual wells is in part a function of the number of fractures intersected by the well and the permeability of each fracture.

It has been found that the standard methods of pump test analysis developed for isotropic, porous media cannot be applied to wells completed in fractured rock aquifers (Lewis and Burgy, 1964). This may be largely because the assumptions on which the methods of analysis are based are not applicable to pump tests in fractured rock aquifers. In addition, if fractures deform with changes of fluid pressure the resulting decrease in fracture permeability with increased drawdown in the pumping well may also be a contributing factor.

Bernaix (1967) has shown in laboratory tests that a significant increase in the effective stress and the resulting closure of a fracture are reflected in a significant decrease in the permeability. This stress-permeability relationship has been inferred from pumping tests on the Rocky Mountain Arsenal well near Denver, Colorado. Evans (1966) reported that the well drawdown was rapid during pumping (increase in effective stress), but that the fractured metamorphic rock aquifer in which the well was located accepted large flow rates during injection (decrease in effective stress), suggesting that the fracture permeability increased with more pressure in the well.

In unconsolidated aquifers the deformations resulting from a decrease in pressure have been the subject of several theoretical discussions, e.g., Verruijt (1969) and Helm (1974). The surface displacements produced by the pumping of unconsolidated aquifers are significant and have been measured by Davis, Peterson and Halderman (1969), Wolff (1970) and Helm (1974).

Karanjac (1971) has discussed the effects of pressure changes on storage and permeability in porous elastic aquifers. In the case of fractured rock aquifers where there is effectively no primary permeability, very little work, if any, has been done on

the effect of a deformable fracture system on the behaviour of a well completed in such a system. Snow (1968a) developed an equation of groundwater flow for deformable fracture systems based on a linear relationship between the change in contact load between rock blocks (or the change in fluid pressure) and the change in aperture. A similar equation was developed by Serafim (1968). Shehata (1971) modified Snow's equation to account for his laboratory determined semilogarithmic relationship between applied load and change in fracture aperture. No rigorous attempt has been made to apply these equations to problems of well behaviour in fractured rock systems.

Direct field observations of fracture deformation resulting from fluid pressure changes are limited. Snow (1968a) described an 80-ft deep water supply well at the Cecil H. Green Observatory, Bergen Park, Colorado. This well is drilled in highly fractured metamorphic rock; a 30-ft drawdown in the well produced radial and tangential ground strains of 10^{-7} to 10^{-8} at distances up to 250 ft to 300 ft from the well.

Using conventional packer injection tests, attempts to evaluate the hydraulic characteristics of saturated fractured rock systems, where the rock blocks are essentially impermeable, have in some instances demonstrated a nonlinear relationship between pressure and flow rate (Louis, 1969; Snow, 1968a). Maini (1971) has suggested that this nonlinearity can be attributed to

- (a) kinetic energy effects,
- (b) nonlinear pressure-flow laws,
- (c) leakage past packers, and
- (d) increase in fracture aperture.

Maini evaluated the relative importance of these four factors but did not conclusively determine the dominant factor. If we consider the pressure-flow rate results of Louis and Maini (1970) for very deformable and normal rock (Fig. 1), we are led to the conclusion that fracture deformation can be an important factor in some field situations.

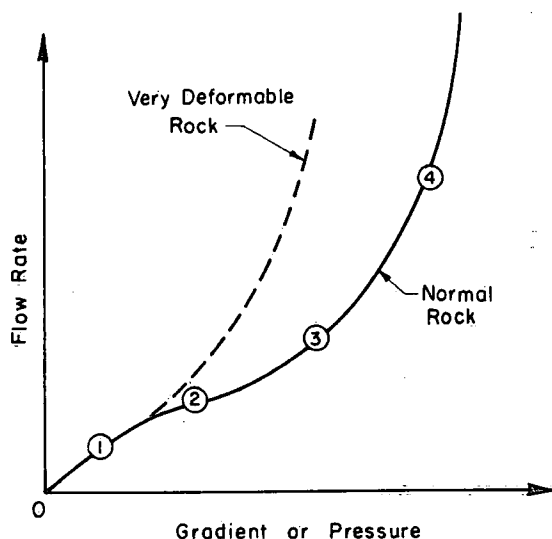


Figure 1. Typical results of field water tests: (1) laminar flow, (2) turbulence effect, (3) turbulence offset by fissure expansion, (4) predominance of fissure expansion effects (after Louis and Maini, 1970).

Most workers (Wilson and Witherspoon, 1970; Louis, 1969; Snow, 1965) have used the parallel plate analogy to determine an expression for fracture permeability which states that the hydraulic conductivity of a fracture is a function of the aperture squared. The flow rate per unit cross-sectional area of the fracture is a function of the aperture cubed.

Thus it can be appreciated that a small change in fracture aperture will have a considerable influence on the discharge from that fracture. When fluid is injected into or withdrawn from a well the greatest pressure change occurs at and in the immediate vicinity of the well bore. Therefore it is important to know whether the fracture apertures will open or close significantly as a result of fluid pressure changes during injection or withdrawal tests. Also, if deformation does occur it is important to know whether it is recoverable or nonrecoverable or a combination of both, since this would determine whether the permeability of the fractures intersecting the well would be permanently changed.

OBJECTIVES AND SCOPE

A three-part program of research was undertaken with two objectives: (1) to determine whether fractures do deform as a result of changes of fluid pressure within the fracture plane and (2) if the fractures deform, to determine what effect fracture deformation has on fluid pressure distribution, fracture permeability and flow rate within a fractured rock mass. The research program consisted of

- (1) a numerical model study of the interaction of fluid pressures and rock stresses;
- (2) a field experiment to measure *in situ* the changes in fracture aperture owing to changes of fluid pressure; and
- (3) a laboratory study of fracture deformation using large-diameter rock cores.

The numerical model consists of two finite-element programs: a two-dimensional plane strain program to model the displacements and stresses in the rock blocks and fractures, and a one-dimensional program to model flow in the fractures (Noorishad, Witherspoon and Brekke, 1971). The programs are coupled by the interaction of the rock stresses and fluid pressures. The rock mass is idealized as a system of rock blocks and discrete fractures. The blocks are assumed to be impermeable and thus flow occurs only in the fractures. For the flow analysis the fractures have been idealized as parallel plate openings.

The computer program can simulate both two-dimensional vertical and horizontal sections and axisymmetric fractured rock bodies. The emphasis in this study is on the axisymmetric case. Thus later in this report, flow to a well intersecting a system of horizontal fractures is simulated.

The field experiment consisted of attempting to measure in boreholes the changes in fracture aperture because of varying fluid pressures resulting from injection and withdrawal. The necessary borehole equipment was designed and fabricated. The experimental nature of the equipment limited the tests to fractures within the first 50 ft of the ground surface. The equipment arrangement did not permit a precise determination of the changes of flow rate for given changes in fracture aperture. In addition, the flow boundaries could not be accurately determined in the field.

To determine simultaneously the fluid pressure, flow rate, aperture changes and applied load under known boundary conditions, a laboratory study was undertaken with a 3-ft diameter rock core, 6 ft long. Artificial fractures were formed normal to the axis of the core. This presented a situation that could be simulated using the numerical model. It should be noted that the artificially created fractures have fresh surfaces that have strength characteristics different from the weathered fractures found in most field situations.

Using the large rock core and test equipment available at the Richmond field station of the University of California, it is possible to simulate injection and withdrawal in a horizontal fracture system for compressive stresses up to 4,000 psi and changes in fluid pressures of up to 1,000 psi. Thus a variety of pumping conditions at depths that would be out of reach for any field experiment can be simulated. Comparison of the numerical model and laboratory results serves to verify the numerical model and increase confidence in the field measurements.

PREVIOUS WORK

Flow in Fractured Rocks

Wilson and Witherspoon have thoroughly reviewed the work on fluid flow through fractured rocks, in the fields of both groundwater hydrology and petroleum engineering. Their work includes an extensive set of references that is essentially complete to 1970. A brief summary of the work done prior to 1970 will give an appropriate background for the more detailed discussion that is presented later of the work published since then.

In this report, following the convention of Wilson and Witherspoon, the term "fracture" is used for most discontinuities within a rock mass. The word "joint" will be generally employed in connection with the finite-element joint model to conform to the convention of the original authors (Goodman, Taylor and Brekke, 1968).

Snow (1965) has presented a comprehensive review of fracturing or discontinuities based on the existing geological literature. Hodgson's (1961a, 1961b) careful study of fracture characteristics provides a basic framework for describing fractures in the field and does much to extend the understanding of how fractures can act as conduits. Snow (1965), Király (1969) and Mahtab *et al.* (1972) have contributed to the statistical description of the orientation of fracture systems. Parsons (1972) has used the approach of Snow and Király in a study of the contribution of flow in fractures to the regional groundwater flow system. A review of the literature shows the necessity for a consistent terminology with which to describe and map fracture characteristics and fracture systems in the field for groundwater purposes.

Mathematical modelling of fluid flow in fractured rock masses has been in two directions: (1) deterministic models where the geometry of the fracture system is assumed to be known and (2) statistical models where the geometry of the fracture system is represented by appropriate statistical distributions.

The approach in the statistical work has been to develop an equivalent porous medium model that describes the hydraulic behaviour of the fracture system. If the rock blocks are porous it is generally assumed that they provide nearly all of the storage, while the fractures act as the main conduits (Barenblatt, Zheltov and Kochina, 1960). The major contributors in the statistical approach have been Snow (1965) and Romm and Pozinenko (1963). In both papers the properties of the fracture system (fracture orientation, spacing and apertures) are used to develop a permeability tensor describing the hydraulics of the rock mass. This approach is dependent on determining the fracture aperture distribution. Snow (1965) has contributed to this area by using the statistics of borehole injection tests to obtain the aperture distribution parameters (Snow, 1968b and 1969). An attempt by Bianchi and Snow (1968) to measure fracture apertures directly by using a photographic technique on bedrock exposures verified Snow's (1965) assumed log normal distribution for the apertures. The aperture distribution parameters determined from the field study, however, were considerably larger than the distribution parameters calculated for similar rock types using Snow's injection test approach. Bianchi and Snow have attributed this difference to weathering and stress relief at the surface. Thus the size of the apertures is the most difficult parameter to measure and remains one of the most important parameters in any analysis of flow in fractured rock masses.

In the deterministic models, each fracture is modelled separately using an approach based on network analysis. The cost of obtaining the necessary data for such models is high but related to the accuracy required. Louis and Pernot (1972) used drill holes and adits to determine the geometry and nature of the discontinuities at a proposed dam site in France. With improved borehole technology and the greater emphasis on safety, this sort of investigation will become routine, providing considerable input data for

deterministic models. The decision to use either a deterministic or a statistical model is dependent on the scale of the structure or area relative to the spacing and size of the important discontinuities as well as on the ability to collect the appropriate fracture data.

Wilson and Witherspoon developed a finite-element deterministic model of discrete fracture systems. The fractures were assumed to be rigid. This approach was used to investigate several different flow problems including the effects of fracture aperture size on flow under a dam and the effect of tunnel size on groundwater inflow.

Considerable work has been done by the petroleum industry on the movement of fluids in fractured reservoirs. Much of this work has been statistical (Law, 1944; Warren and Price, 1961). From core-analysis and pressure test data, Warren and Price concluded that the most probable behaviour of a heterogeneous system with single-phase flow is similar to that of a homogeneous system having a permeability equal to the geometric mean of the permeability distribution for the heterogeneous system.

Warren and Root (1963) extended this approach to naturally fractured reservoirs using a two-porosity model similar to that of Barenblatt, Zheltov and Kochina; their model contained a primary porosity (intergranular) and a secondary porosity (fractures, joints and vugs). The primary porosity was considered to contribute significantly to storage but negligibly to conductivity; the opposite is true for the fractures or secondary porosity.

The model of Warren and Root consists of an array of homogeneous, isotropic, rectangular parallelepipeds, bounded by an orthogonal system of continuous, uniform fractures. Each fracture is parallel to one of the principal axes of permeability; the fractures normal to each of the principal axes are uniformly spaced and are of constant width. They observed that the time required to achieve approximate steady-state conditions in a heterogeneous reservoir is one or two orders of magnitude greater than it is in a homogeneous reservoir.

Parsons (1966) studied two separate cases of fractured rock systems using two-dimensional mathematical models. In the first case, a regular fracture model was developed. This model could have any number of regular vertical fracture sets, with the restriction that the fractures in each set must have the same orientation, width and spacing. The parallel plate law was the governing flow equation. If, for the situation above, the matrix is assumed to be permeable and fluid is permitted to move freely between the fractures and the rock blocks, then this model, according to Parsons, is equivalent to a homogeneous anisotropic medium. Parsons assumed that the pressure fields in the two systems were identical and that superposition of the two systems would cause flow in each to behave as if the other were not present.

Parsons also studied a heterogeneous fracture model with fractures having varying hydraulic conductivity but placed in a given pattern in an impermeable medium. He considered this model to be equivalent to a heterogeneous network of resistors. His results verified the conclusion of Warren and Price that for orthogonal fracture patterns when the conductivity values are not too dispersed, the geometric mean of the conductivity distribution is a fair approximation to the overall conductivity.

Kazemi (1969) extended the work of Warren and Root to unsteady flow in a finite circular reservoir consisting of a set of uniformly spaced horizontal fractures with an intervening permeable matrix. Flow to the well is assumed to take place largely through the high-capacity fractures. The results obtained from Kazemi's model essentially verified the results obtained by Warren and Root. Kazemi concluded that the behaviour of a fractured reservoir approaches that of an equivalent homogeneous reservoir at large times.

In a sequel to Kazemi (1969), Kazemi, Seth and Thomas (1969) applied the double porosity model of Warren and Root to the interpretation of interference tests in naturally fractured reservoirs assuming a uniform fracture distribution. Results of their analyses demonstrated the marked anisotropy of the reservoir in that for early time responses, an equivalent homogeneous model does not adequately depict interference effects in naturally fractured reservoirs. For later times, however, the agreement was good, which corresponds to the results of Kazemi.

Hantush (1966), assuming that fractured rock aquifers can be represented as equivalent anisotropic aquifers, presented a method for analyzing pump test results for the case of an infinite homogeneous anisotropic leaky (fractured rock) aquifer. Using the same approach, Hantush and Thomas (1966) developed a similar method for analyzing pump tests in nonleaky aquifers. To obtain significant results from the solutions above, observations should be made in at least two linear arrays of observation wells if the principal directions of anisotropy are known. Three linear arrays are needed if the principal directions are not known. These observation wells are necessary in order to define completely the elliptical shape of the drawdown cone from which the major and minor axes, corresponding to the principal axes of anisotropy, can be determined graphically. The cost of such arrays of wells could prove to be a decisive limiting factor.

A more practical method was presented by Papadopoulos (1967) for the two-dimensional case of a well discharging from an infinite homogeneous anisotropic aquifer. The anisotropy is assumed to be the result of joint patterns causing permeability variations in different directions. The final form of the solution obtained by Papadopoulos contains three independent components of the transmissivity tensor and the storage coefficient. Thus, a minimum of three observation wells oriented in a selected pattern with respect to the orientation of the fracture system is required.

Rofail (1967) also proposed a method for analyzing pump tests in fractured rocks based on the radial flow equation developed by Polubarinova-Kochina (1962). Using the solution to this equation, Rofail plotted type curves for the well function. The method appears to be somewhat restricted by the use of coefficients, borrowed from Barenblatt, Zheltov and Kochina, to describe the fracture geometry. Also, the method proposed does not appear to account for a noncircular drawdown cone, since it is suggested that drawdown data from one observation well or one array of wells would be adequate for determining the aquifer parameters.

An extension of work in the petroleum industry is that of Gringarten and Witherspoon (1972) in which Green's functions were used to model flow to a well that intersects a single fracture. Using type curves, the authors were able to distinguish between aquifers with horizontal and vertical fractures by using drawdown data from either the pumping well or some nearby observation well. This approach is greatly improved by the collection of drawdown data during the early part of the pump test.

Experimental Work on Flow in Fractures

One of the earliest and most extensive laboratory experiments on flow in fractures was conducted by Lomize (1951). Lomize used plates to model fractures with variable cross sections and curvilinear outlines. Louis (1969), in a study (based on Lomize's work) of the stability of fractured rock slopes, performed a series of laboratory experiments with single fractures. Louis pointed out the importance of fracture roughness for flow in fractures and he formulated a series of flow laws to account for several different fracture roughnesses. From numerical and laboratory results, Louis (1969) concluded that turbulence would not have an important effect on the flow or pressure distribution in a fracture system.

From the results of laboratory tests on a single natural fracture, Sharp (1970) questioned the theoretical relationship that flow in a fracture varies as the cube of the aperture. Sharp assumed that his fracture was closed when a measurable flow rate was still occurring. He investigated the effects of changing the aperture size by measuring the flow rates from which he subtracted the reference flow rate for the "effective zero" opening. Sharp concluded that the discharge was related to the aperture by some exponential factor less than three. A review of his data, however, suggests that the cubed relationship was still valid for his experimental conditions if one takes the flow rate corresponding to the "effective zero" opening into account.

The basic parallel plate flow model, as applied to fracture flow, is derived from the Navier-Stokes equation by assuming an average flow velocity. One should not attempt to account for the reduced flow rates in fractures where roughness of the fracture walls is a

significant factor by varying the basic cubic relationship. Instead, one should either alter the size of the aperture, making it a function of the space coordinates, or expand the basic parallel plate relationship by adding a compatible term to compensate for the deviation of the fracture in question from the concept of smooth parallel walls.

Sharp also completed an extensive study of the different methods of draining fractured rock slopes, using both digital and analog models.

Maini used a transparent modelling material to duplicate a natural fracture. By injecting dyes into the flow field Maini was able to demonstrate clearly the discontinuous nature of the flow field within the fracture plane. Maini also discussed the application of different methods of collecting and interpreting field data on the hydraulics of fractured media. More recently, a similar approach has been used by Louis (1974), which when combined with a knowledge of the fracture geometry, permits the determination of the three principal components of the permeability tensor. It should be noted that a rigorous solution to the calculation of the permeability tensor using data obtained from injection tests in oriented drill holes has been presented by Snow (1966).

Jouanna (1972) conducted both laboratory tests and small-scale field tests on finely fissured mica schist. In the laboratory, the samples were placed under biaxial loading conditions and the changes in flow rate were measured. In the field, the flow rates for different levels of applied normal stress were measured. It is interesting to note that his test results show a nonrecoverable deformation for repeated stress levels. Jouanna has presented a considerable volume of field and laboratory data on the effects of mechanical loads on flow in finely fissured media. Jouanna's work was extended by Rayneau (1972) to the study of flow in a single artificial fracture subject to changing external loads.

Recent work by Sarda, Le Tirant and Baron (1974) also shows the dependence of flow on effective stress and the nonreversible nature of the flow during repeated stress cycles.

Ohnishi and Goodman (1974) reported the results of triaxial and direct shear laboratory tests on artificial fractures in sandstones during which no drainage into or out of the sample was allowed. They measured induced pore pressures that were 10% to 15% of the deviator stress at peak load in triaxial experiments and 10% to 20% of the peak shear stress during direct shear experiments. Thus the induced pore pressures could significantly reduce the effective normal stress across a fracture and hence its shear strength.

Fracture Deformation

As pointed out earlier in this Chapter, direct evidence of fracture deformation owing to changes of fluid pressure in the fracture system is limited. One of the first direct measurements of fracture deformation was performed by Davis and Moore (1965). They placed deformation gauges across a fracture at approximately 85 ft below the ground surface in a cave. They were able to measure relative movements (a few microns) of the fracture walls produced by earth tides. Snow (1968a) described an 80-ft deep water supply well at the Cecil H. Green Geophysical Observatory, Bergen Park, Colorado. This well, drilled in metamorphic rock, produced radial and tangential surface ground strains of 10^{-7} to 10^{-8} at distances of up to 250 ft to 300 ft from the well for a drawdown of 30 ft. In addition, a two-hour time lag was observed on the strain records every time the well was pumped. The measuring devices in this case were 80-ft long quartz rod strain meters.

More indirect evidence of fracture deformation, mentioned earlier, is the difference between pumping into and out of a well (Evans) and the nonlinear relationship between fluid pressure and flow rate during injection tests (Snow, 1965; Louis and Maini, 1970). Shehata postulated the closing of fractures to account for reverse water level fluctuations in an observation well while a well in a nearby shear zone was being pumped.

Laboratory measurements of fracture deformation have generally been associated with the determination of the deformability characteristics of fractures. Goodman (1974) has provided an extensive review of this work. Shehata presents the results of a limited number of laboratory tests in which he measured the force-displacement relationship for one natural and two artificial fractures.

Theoretical and numerical studies of fluid flow in fractured rock masses, taking into account the deformable nature of the fractures, have been conducted by Noorishad, Witherspoon and Brekke (1971), Rodatz and Wittke (1972) and Morgenstern and Guthrie (1972). Noorishad, Witherspoon and Brekke (1971) and Rodatz and Wittke (1972) modelled the fractures as discrete elements. Morgenstern and Guthrie assumed that the fractured rock mass could be replaced by an equivalent porous media. How this assumption affects the fluid pressure distribution and flow rate in nonuniform fracture apertures is investigated in Chapter 2.

Noorishad, Witherspoon and Brekke combined two finite-element programs: a steady-state line element program to model flow through the fracture system, and a plane strain structural program incorporating joint elements to model displacements and stresses within the rock mass. The fluid pressures were allowed to interact with the rock blocks to simulate a coupled stress-flow phenomenon. Using this program, Noorishad, Witherspoon and Brekke have demonstrated the feasibility of studying the effects of fluid pressures on

changes in fracture apertures. This approach has been modified here in order to model general two-dimensional plane strain and axisymmetric problems. The modification is described in Chapter 2.

Recently, Duguid (1973) modelled nonsteady flow in porous fractured rocks using the finite-element method. His theoretical development is based on the two-porosity model of Barenblatt, Zheltov and Kochina and the elastic theory of Biot (1940). The fractures are described as a statistical distribution and flow in the fracture system is coupled to that in the porous blocks by a storage equation. Duguid presents some very interesting results in which he shows how the ratio of the fracture permeability to the permeability of the porous rock blocks affects the time required to reach a steady-state fluid pressure distribution. His approach, if combined with a discrete deformable fracture model, would provide a powerful analytical tool.

Theory of Fluid Flow in Deformable Fracture Systems

INTRODUCTION

The steady-state distribution of fluid pressures owing to flow in a rigid fractured rock mass, for given boundary conditions, is determined by the distribution of fracture apertures (Wilson and Witherspoon, 1970). In a deformable fractured rock mass, the distribution of fracture apertures is equally important, but the distribution of fluid pressures is affected by the interaction of flow forces, body forces, initial stress conditions and boundary loads. The effective stress concept requires that the fluid pressure distribution must be compatible with the state of stress in the rock mass. A change in the fluid pressure changes the effective normal stress acting across a fracture. Since the fractures are assumed to be deformable, a change in the effective normal stress causes the fractures to deform (open or close), affecting both the pressure distribution and the flow rates within the fracture system.

The method of analysis used in this study to investigate the interaction between fluid pressures and rock stresses is a modification and extension of an approach presented by Noorishad, Witherspoon and Brekke. The basic approach consists of using two finite-element programs: (1) a one-dimensional line element program to model steady-state flow in the fracture system and (2) a two-dimensional plane strain program to determine the displacements and stresses in the fractured rock mass. The computer program has been modified to permit the modelling of irregularly shaped, two-dimensional, vertical and horizontal sections and has also been extended to simulate axisymmetric bodies of fractured rocks. In the vertical and horizontal sections, any number of fracture sets having arbitrary orientations can be simulated. In the axisymmetric cases, the process of generating the elements in the horizontal plane restricts the model to horizontal or near-horizontal fractures.

As will be shown later, the two finite-element programs are coupled by the interaction of the fluid pressures and the displacements within the rock mass. The displacement and flow problems will be formulated using the more direct approach of the Galerkin method rather than the variational approach used by Noorishad, Witherspoon and Brekke.

Fluid flow in the fracture systems is assumed to be governed by Darcy's law where the permeability term, or the hydraulic conductivity (LT^{-1}), is derived by idealizing the fractures as parallel plate openings.

The Reynolds numbers and flow velocities are computed as an average for a given fracture element. In general, the averaged Reynolds numbers were calculated to be well below 200, which is the upper limit for laminar flow in a fracture with parallel sides where the roughness does not exceed 0.5 (Louis, 1969). Nevertheless, because of the variation of velocity in the radial direction, turbulent flow may exist near a well.

GOVERNING EQUATIONS

Flow in a Single Fracture - The Parallel Plate Analogy

Equations describing fluid flow between two parallel plates have been derived by Polubarinova-Kochina (1962), Snow (1965), Louis (1969), Noorishad, Witherspoon and Brekke (1971), Bear (1972) and several others in the field of fracture flow. The derivation of the equation presented here closely follows that of the previous authors.

The Navier-Stokes equation for the flow of a viscous incompressible fluid may be written in the form [e.g., Bear (1972)]

$$\frac{D V_i}{Dt} = f_i - \frac{1}{\rho_f} \text{grad } p + \nu \nabla^2 V_i \quad (1)$$

where $\frac{D ()}{Dt}$ = the total derivative

V_i = the velocity components in the coordinate directions ($i = 1, 2, 3$)

f_i = the components of the body force per unit mass of the fluid

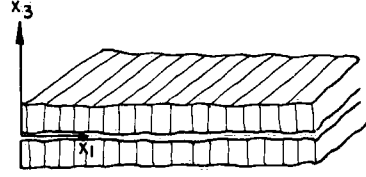
ρ_f = the fluid density

p = the fluid pressure

ν = the kinematic viscosity

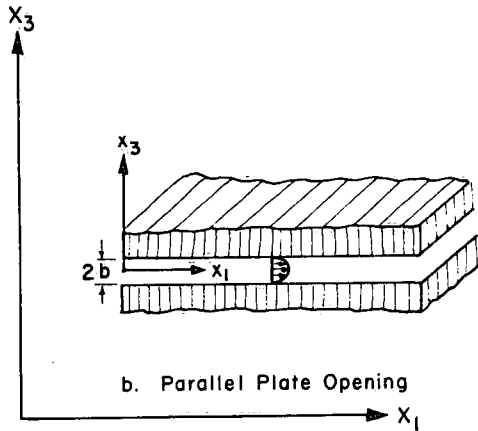
∇^2 = the Laplacian operator.

The left-hand side of equation (1) represents the inertial term in the Navier-Stokes equation. For flow between two parallel plates (Fig. 2) and low fluid velocities (within the laminar regime) or fluids with high viscosities, the inertial terms can be disregarded because the viscous forces are much greater than the inertial forces. Thus



a. Natural Fracture

Figure 2. Flow in a single fracture.



b. Parallel Plate Opening

the only active body force is gravity (g) and the gravity force potential can be written as $\text{grad}(-gx_3)$. Therefore equation (1) becomes

$$\nu \nabla^2 v_i = g \text{grad} \left(x_3 + \frac{p}{\rho_f g} \right) \quad (2)$$

For one-dimensional flow parallel to the x_1 axis,¹ equation (2) reduces to

$$\nu \frac{\partial^2 v_{x_1}}{\partial x_3^2} = g \text{grad} \left(x_3 + \frac{p}{\rho_f g} \right) \quad (3)$$

where $\text{grad} x_3$ is a constant and represents the projection of the local coordinate x_3 on the vertical axis of the global coordinate system.

¹The local coordinate system is x_1, x_2, x_3 ; the orientation of the coordinate axes is related to the fracture orientation (Fig. 2).

From physical considerations (Fig. 2), it can be shown that grad p is independent of x_2 and x_3 (i.e., the flow is laminar and $2b$, the fracture aperture, is very small when compared with the fracture length). Integrating equation (3) with respect to x_3

$$V_{x_1} = \frac{g}{\nu} \text{grad } H \left(\frac{x_3^2}{2} \right) + C x_3 + D \quad (4)$$

where H equals $(x_3 + \frac{p}{\rho_f g})$, the hydraulic head.

For a viscous fluid, the fluid velocity profile between two parallel plates (Fig. 2) approximates a parabolic curve. If the plates are separated by a constant width ($2b$) over their entire length, the velocity gradients in the x_1 and x_2 directions are equal to zero. Thus for one-dimensional flow, the boundary conditions are

$$V_{x_1} = 0 \quad \text{for } x_3 = b \quad (5)$$

and
$$V_{x_1} = 0 \quad \text{for } x_3 = -b \quad (6)$$

As a consequence of equations (5) and (6)

$$\frac{\partial V_{x_1}}{\partial x_3} = 0 \quad \text{for } x_3 = 0 \quad (7)$$

Applying condition (7) to equation (4) it is found that $C = 0$, and hence from equation (5)

$$D = - \frac{g}{2\nu} \text{grad } H b^2 \quad (8)$$

Thus equation (4) becomes

$$V_{x_1} = \frac{g}{2\nu} \text{grad } H (x_3^2 - b^2) \quad (9)$$

and describes the velocity profile in a planar conduit.

Integration of equation (9) between the limits of $\pm b$ gives the discharge q ($L^3 T^{-1}$) of fluid through a cross-sectional area [parallel plate opening ($2b$) multiplied by a unit length parallel to the x_2 axis]:

$$q = - g \frac{(2b)^3}{12\nu} \text{grad } H \cdot (\text{unit length}) \quad (10)$$

or
$$q = - \frac{\rho_f g}{12\mu} (2b)^3 \text{ grad } H. \text{ (unit length)} \quad (11)$$

where
$$k_p = \frac{\rho_f g}{12\mu} (2b)^3. \text{ (unit length)} \quad (12)$$

is defined as the "area permeability" (Noorishad, Witherspoon and Brekke, 1971); v in equation (10) has been replaced by the relationship

$$v = \frac{\mu}{\rho_f} \quad (13)$$

where μ is the dynamic viscosity of the fluid.

The average velocity of flow parallel to the x_1 axis becomes

$$v_a = - \frac{\rho_f g}{12\mu} (2b)^2 \frac{\partial H}{\partial x_1} \quad (14)$$

It can be seen that this expression describing flow between two parallel plates is analogous to Darcy's law and thus for flow in a planar smooth-walled fracture the hydraulic conductivity ($L T^{-1}$) is defined by

$$k = \frac{\rho_f g}{12\mu} (2b)^2 \quad (15)$$

which describes both the capacity of the fracture to transmit fluid $\frac{(2b)^2}{12}$ and the fluid itself $\frac{\rho_f}{\mu}$.

Since in this study flow is considered either in horizontal sections through vertical fractures or in horizontal fractures (axisymmetric bodies), it is convenient to express equations (10) and (14) in terms of pressure instead of hydraulic head. Thus equation (12) is replaced by

$$K_p = \frac{(2b)^3}{12\mu} . \text{ (unit length)} \quad (16)$$

When K_p is multiplied by the pressure gradient the units obtained are the same as those in equation (12), i.e., $L^3 T^{-1}$.

Flow in a Fracture System

The differential equations governing steady-state flow of an incompressible viscous fluid in a fracture or joint are approximated from the Navier-Stokes equation by

$$q = -K_p \frac{\partial p}{\partial \ell} \quad (17)$$

and

$$\frac{\partial}{\partial \ell} \left(K_p \frac{\partial p}{\partial \ell} \right) = 0 \quad (18)$$

where equations (17) and (18) are the constitutive and continuity equations, respectively, $K_p \frac{\partial p}{\partial \ell}$ is the volume of flow per unit of time through a cross-sectional area of the fracture, p is the fluid pressure and ℓ is the distance along the fracture or joint.

Assuming parallel plate flow, the fluid pressures p_i and p_j can be determined at each end of a fracture segment (Fig. 3), and hence the distribution of fluid pressures within the fractures. The fluid pressure is assumed to vary linearly within each fracture element. The boundary conditions are expressed by specifying either pressure or flow rate at the appropriate nodal points.

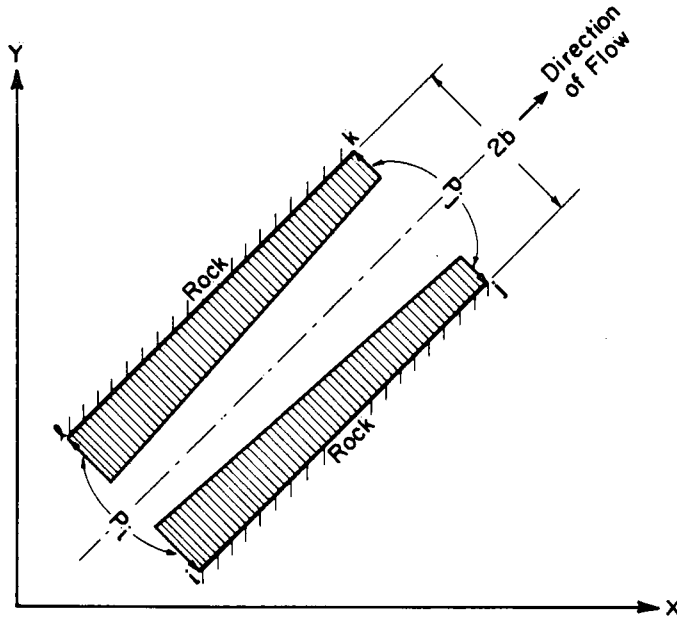


Figure 3. Flow in a fracture with parallel sides.

In analyzing fluid flow through a given fracture system, it is assumed that the geometry and permeability of individual fractures are known and that the system is divided into a network of fracture elements. Flow nodal points can be specified at any point along a fracture segment, but they must always include all intersections of fracture elements with each other and with the boundaries. An appropriate equation to describe the flow in each element is sought, and by summing the equations for all flow nodal points in the network, a matrix of equations can be developed that describes flow through the whole system. Solving the equations simultaneously provides a solution for the effects of flow at every point in the network.

Stress and Strain Analysis of a Fractured Rock Mass

Metamorphic and granitic rock bodies can be idealized as a system of intact rock blocks bounded by discontinuities (faults, seams, joints, fractures, etc.). The stability and deformation of both natural and engineered rock structures are controlled to a large extent by the orientation and nature of the discontinuities in the rock mass. In this study to determine the displacements and stresses, the rock mass is divided into two constituent parts: (a) a homogeneous continuum which is idealized as a linear elastic solid and (b) fractures or joints which are idealized by planar surfaces on which both normal and tangential deformations can occur.

Rock Blocks

The general form of the equilibrium equation for the continuum phase of the rock mass is

$$\nabla \cdot [\sigma] + \rho_s (f) = 0 \quad (19)$$

where ∇ is the gradient operator, $\nabla \cdot ()$ is the divergence of $()$, $[\sigma]$ is the stress tensor, ρ_s is the density of the rock blocks and (f) is the body force per unit mass. The strain-displacement relationships are

$$[\epsilon] = \frac{1}{2} [\nabla\{u\} + (\nabla\{u\})^T] \quad (20)$$

and the constitutive equation based on a linear elastic assumption becomes

$$[\sigma] = [D] [\epsilon] + [\sigma^0] \quad (21)$$

where $[\epsilon]$ is the strain tensor, $[D]$ is the moduli matrix of the material, $[\sigma^0]$ is the initial stress tensor and $\{u\}$ is the displacement vector. In its general form, $[D]$ is a fourth rank tensor, but for linear elastic isotropic materials under plane strain boundary conditions $[D]$ reduces to

$$[D] = \frac{E(1-\nu)}{(1+\nu)(1-2\nu)} \begin{bmatrix} 1 & \frac{\nu}{1-\nu} & 0 \\ \frac{\nu}{1-\nu} & 1 & 0 \\ 0 & 0 & \frac{1+2\nu}{2(1-\nu)} \end{bmatrix} \quad (22)$$

where E is the Young's modulus of the material and ν is the Poisson's ratio. The material relationships for axisymmetric rock bodies are given in most textbooks on rock mechanics or stress analysis (e.g., Zienkiewicz, 1971, p. 79).

For the particular problems under consideration, the appropriate boundary conditions are

$$\left. \begin{aligned} \{u\} &= \bar{u} \quad \text{on } S_u \\ \{t\} &= \bar{t} \quad \text{on } S_t \end{aligned} \right\} \quad (23)$$

where $\{t\}$ indicates traction forces including fluid pressure effects on the rock surface, $(\bar{})$ denotes a prescribed quantity, S_u is the surface area over which displacement is specified, and S_t indicates the surfaces on which stresses are prescribed including interior surfaces where fluid pressures are applied. The total surface area is given by

$$S = S_u + S_t \quad (24)$$

Fractures

The material characteristics of fractures, in comparison with their spatial distribution, have only recently been the subject of detailed laboratory investigations (John, 1969; Goodman, 1970; Ohnishi, 1973; Goodman, 1974). Goodman, Taylor and Brekke list the characteristics of fractures that should be incorporated in a finite-element representation. These characteristics are summarized here:

- (1) The dimensions of a fracture are much greater in two of its dimensions than in the third dimension normal to the fracture plane. Thus fractures closely resemble an irregular line rather than a zone of any appreciable thickness.
- (2) Fractures have no strength in tension but offer high resistance to compression. Normal deformation occurs under normal compressive stresses and may partly consist of plastic deformation.
- (3) Shear displacement along a fracture is a function of the normal stress. At low normal stresses the fractures may open as a result of shear displacement and thus the shear strength is due to friction. At high normal pressures, shear stresses induce shearing through the irregularities in the fracture plane and thus the shear strength is a function of both cohesion and friction. In this report, shear stresses parallel to the fracture surface are very small and thus the opening (dilatancy) under low normal stress and the cohesion aspects of fractures under high normal stress can be disregarded. Laboratory tests have shown that small shear displacements (elastic deformation) do occur before shear failure takes place.
- (4) The constitutive model for a fracture can be taken as an elastic-plastic model where failure in compression is specified according to a Mohr-Coulomb hypothesis

$$\tau_f = C + \sigma_n \tan \phi \quad (25)$$

where τ_f is the shear stress at failure, C is the cohesion, σ_n is the normal stress and ϕ is the angle of friction in the fracture plane.

Joint element models that closely approximate the observed joint or fracture characteristics have been developed by Goodman, Taylor and Brekke (1968) and Ghaboussi, Wilson and Isenberg (1973). In this analysis, the joint element model of Goodman, Taylor and Brekke has been used (Fig. 4). This element was found to simulate joint behaviour satisfactorily for the range of stresses investigated. Their joint element model was derived from a potential energy equation, and the stress, displacement and constitutive relationships that were assigned to the element are summarized below.

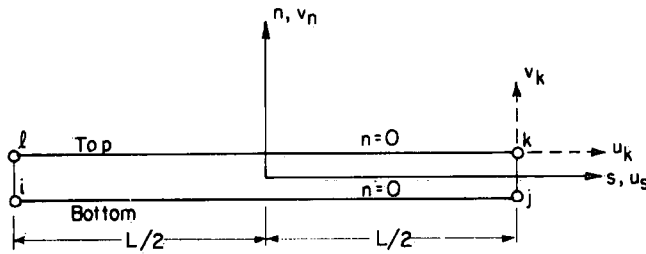


Figure 4. Joint element of Goodman, Taylor and Brekke (1968); u_k and v_k are displacements parallel and perpendicular to the joint plane at nodal point k.

To describe the joint or fracture phase of a rock mass, the traction forces $\{t\}$ are defined as

$$\{t\} = \langle \sigma_n, \tau \rangle \quad (26)$$

where σ_n is the stress acting normal to the plane of the joint and τ is the shear stress acting parallel to the joint surface. The condition of equilibrium to be satisfied becomes

$$\{t_T\} - \{t_B\} = 0 \quad (27)$$

where $\{t_T\}$ and $\{t_B\}$ refer to the forces acting on the top and bottom sides of the joint element. The strain-displacement relationship is given by

$$\{\epsilon\} = \begin{bmatrix} \text{top} & \text{bottom} \\ u_s & -u_s \\ \text{top} & \text{bottom} \\ v_n & -v_n \end{bmatrix} \quad (28)$$

where u_s and v_n are displacements in the directions parallel to and perpendicular to the joint plane, respectively (Fig. 4). This relationship leads to the constitutive equation

$$\{t\} = [K_J] \{\epsilon\} + \{t_0\} \quad (29)$$

where

$$[K_J] = \begin{bmatrix} K_S & 0 \\ 0 & K_N \end{bmatrix} \quad (30)$$

and K_N is the ratio of the normal force acting on the joint to the normal displacement across the joint and K_S is the ratio of the shear stress acting on the joint to the shear displacement along the joint. The initial forces acting on the joint are represented by $\{t_0\}$. The normal and shear stiffness values of the joint K_N and K_S , respectively, are defined as the slope of the force-displacement curves (Figs. 5 and 6). The solid lines in Figures 5 and 6 show the actual behaviour of joints approximated from field and laboratory tests. The broken lines indicate the force-displacement relationships used in the numerical model for the given stress conditions.

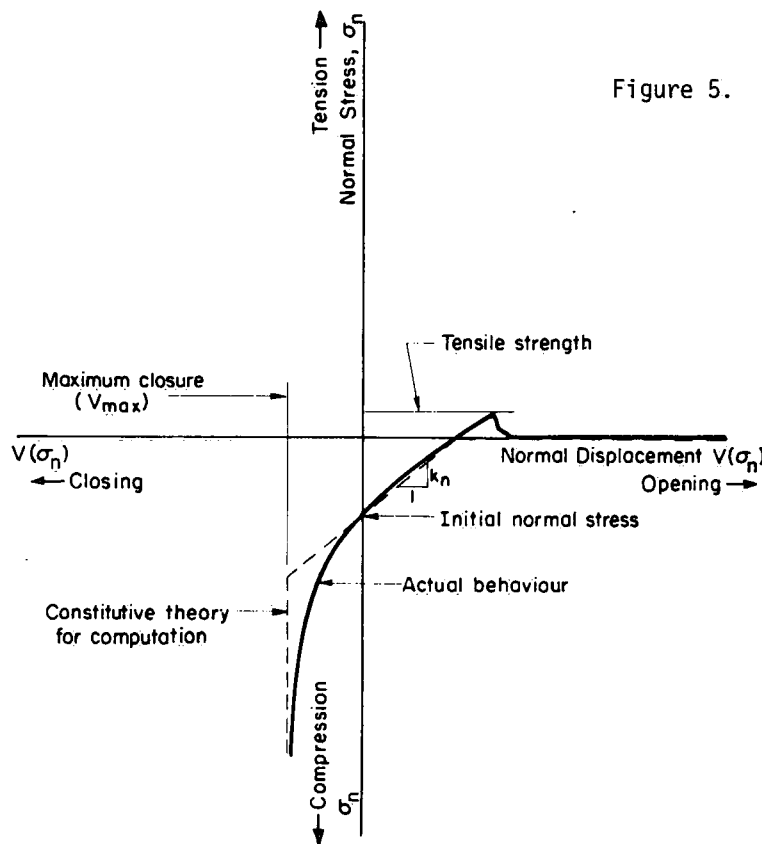


Figure 5. Constitutive model for displacement of a joint under normal stress (after Goodman and Dubois, 1972).

If a fracture is subjected to an initial normal stress (Fig. 5) with some initial fracture aperture and the magnitude of the initial normal stress is altered, then the size of the fracture opening changes (as shown in Fig. 5). For example, if the water pressure within the fracture plane is increased, the effective normal stress decreases and according to the constitutive curve in Figure 5, the fracture opens. In a similar manner, if the water pressure in the fracture plane is decreased the effective normal stress increases and

the fracture closes. From equation (25) it can be shown that this change in effective normal stress alters the shear strength of the fracture.

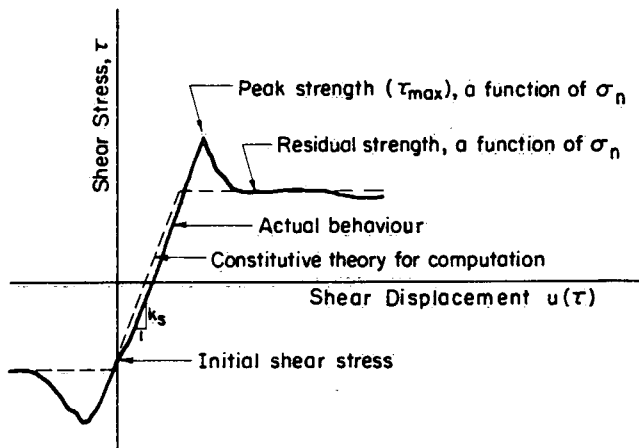


Figure 6. Constitutive model for displacement of a joint under shear stress (after Goodman and Dubois, 1972).

FINITE-ELEMENT FORMULATION

Method of Weighted Residuals

An early approach in finite-element formulation was to replace the problem being considered by finding a functional, the minimization of which gave the correct solution to the original problem. This approach is based on variational calculus and depends on proving the existence of an appropriate variational principle (Zienkiewicz, 1971).

It is possible to reach the finite-element representation of a problem directly from the governing differential equations. These direct approaches do not require the existence of a variational principle, and thus they can be extended to a wide range of problems for which variational principles have not yet been found.

The direct approaches lead to a set of integral equations and are known as the weighted residual methods (Finlayson, 1972; Zienkiewicz, 1971). The general description of the weighted residual methods given here follows that of Zienkiewicz (1971, p. 39).

The approximate solution of a set of differential equations with unknown displacement function $\{u\}$ in a region V must be determined. The governing equation is

$$A(\{u\}) = 0 \quad (31)$$

where A is some linear operator. The boundary condition to be satisfied is

$$C(\{u\}) = 0 \quad (32)$$

on the boundary S.

A trial solution can be written in the general form

$$\{u\} = [N] \{\delta\} \quad (33)$$

which satisfies the boundary conditions. Specified linearly independent coordinate functions are [N] and $\{\delta\}$ is a set of values, e.g., the nodal point displacements in plane strain problems. Substitution of the trial solution in equation (31) does not usually produce an exact solution. Instead, it is found that

$$A(\{u\}) = R \neq 0 \quad (34)$$

The best solution can be reached by reducing the residual R to some minimum value at all points in the region V. This can be done by forcing R to be zero at every point V. To achieve this some weighting function, W_i , which is a function of the coordinates, is selected for each point for which the value of $\{\delta\}$ is required. Thus a system of simultaneous equations can be written in the form

$$\int_V W_i R \, dv = \int_V W_i A([N] \{\delta\}) \, dv = 0 \quad (35)$$

from which the values of $\{\delta\}$ at the points of interest (i.e., nodal points) can now be obtained.

The choice of the weighting function, W_i , determines the weighted residual method used (Zienkiewicz, 1971, p. 40). In this study the Galerkin method, in which the weighting function is made equal to the shape function, has been used to develop the equations for the finite-element approximation.

At this point a general description of the nature and relationship of the shape functions to the unknown functions is necessary. Since the analysis of displacements in a rock mass is involved, the displacement vector $\{u(x,y)\}$ has been chosen as the unknown function. A typical triangular finite-element of the rock mass with nodal points i, j and k (Fig. 7) is considered. It is assumed that the displacements at any point within the element are defined by

$$\{u\} = [N] \{\delta\}^e \quad (36)$$

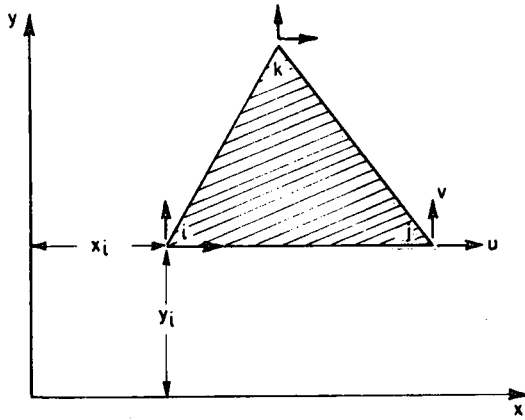


Figure 7. Triangular element.

where the components of $[N]$ are general functions of the coordinates and $\{\delta\}^e$ are the nodal point displacements. Note that in the mathematical sense there is no differentiation between the true solution as defined by equation (19) and the approximate solution defined by equation (36). For plane strain

$$\{u\} = \begin{Bmatrix} u(x,y) \\ v(x,y) \end{Bmatrix} \quad (37)$$

where $u(x,y)$ and $v(x,y)$ represent horizontal and vertical movements, respectively, of a typical point within the element and

$$\{\delta_i\} = \begin{Bmatrix} u_i \\ v_i \end{Bmatrix} \quad (38)$$

represents the corresponding displacements of a node i . The functions N_i , N_j and N_k are chosen to have a value of unity at the nodal points in question and zero at all other nodal points, i.e.,

$$N_i(x_i, y_i) = 1 \quad (39)$$

$$\text{while} \quad N_i(x_j, y_j) = N_i(x_k, y_k) = 0 \quad (40)$$

Thus from equation (36) it can be seen that substitution of the coordinates of a given node on the left-hand side of the equation gives the appropriate displacements for that node.

The functions $[N]$ are called shape functions, and it will be shown later that they play a very important role in finite-element analysis (Zienkiewicz, 1971, p. 19).

The Galerkin method is described and discussed in some detail by Kantorovich and Krylov (1958), Finlayson (1972), Douglas and Dupont (1970), Mikhlin (1964) and Hutton and Anderson (1971). The requirements for convergence of the Galerkin approximation are discussed by Kantorovich and Krylov (1958, p. 273), who point out that the requirements on the error bound can be relaxed with respect to the highest partial derivatives of the function. Thus taking the average error obtained by integrating over the domain rather than the maximum error obtained by comparing each point separately gives a satisfactory, but weakened, solution to the governing equation.

The basic objective of the finite-element approach is to cast the problem in the general form of "structural" or "stiffness" equations (Zienkiewicz, 1971, p. 2), which for a simple structural problem have the form

$$[K] \{\delta\} - \{F\} = 0 \quad (41)$$

where $[K]$ is referred to as the stiffness matrix and consists of terms describing the geometry and material properties of the system and includes the appropriate shape functions, $\{\delta\}$ is the function whose values are sought at given points and $\{F\}$ is the force vector. The same form of the equations exists for fluid problems with $\{\delta\}$ being replaced by either fluid pressure, hydraulic head or fluid potential and $\{F\}$, by the flow rate. Having obtained the appropriate set of equations, application of the boundary conditions leads to the required solution. The derivation of the stiffness matrix is an important part of the finite-element process.

Application of the Galerkin Method

To determine the effects of the interaction of fluid pressures and rock stresses, a finite-element model is constructed to simulate both the flow in the fractures and the displacements in the rock mass. The problem is formulated using the Galerkin approach where pressure and displacements are the primary variables. The governing equations are (18) and (19)

$$\frac{\partial}{\partial \ell} \left(K_p \frac{\partial p}{\partial \ell} \right) = 0$$

and

$$\nabla \cdot [\sigma] + \rho_s (f) = 0$$

where equation (18) describes the steady-state flow in the fractures and equation (19) is the equilibrium equation for the continuum phase of the rock mass.

An approximate solution of the flow problem is sought in the form of

$$\{p\} = \sum_{i=1}^{NP} [\phi] \{P\} \quad (42)$$

and for the displacements in the rock mass in the form of

$$\{u\} = \sum_{i=1}^{NN} [N] \{\delta\} \quad (43)$$

where $[\phi]$ and $[N]$ are the appropriate shape functions and NP and NN are the number of flow nodal points and structural nodal points, respectively. The general characteristics of the shape functions have been described in this Chapter and are such that they have unit value at the node in question and are zero at all other nodes.

Flow in fractures is simulated using line elements. The development of the shape functions for the line elements follows that of Wilson and Witherspoon where the fluid pressure p is assumed to vary linearly between nodal points i and j (Fig. 8) such that

$$p(x') = A + B x' \quad (44)$$

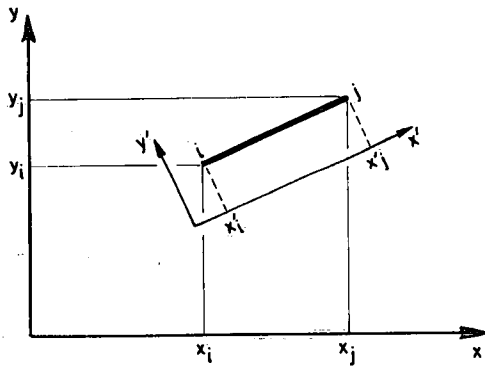


Figure 8. Line element.

If P_i and P_j are considered the fluid pressures at nodal points i and j

$$A = P_i x'_j - P_j x'_i \quad (45)$$

and

$$B = \frac{P_j - P_i}{x'_j - x'_i} \quad (46)$$

Thus from the general definition relating the variation of the function over the element to the nodal values, after substitution for A and B,

$$p(x') = \phi_i P_i + \phi_j P_j \quad (47)$$

where

$$\phi_i = \frac{x'_j - x'}{x'_j - x'_i} \quad (48)$$

and

$$\phi_j = \frac{x' - x'_i}{x'_j - x'_i} \quad (49)$$

Transformation to the global coordinates follows from recognizing that $x'_j - x'_i$ equals the length L and then putting

$$L = \sqrt{(x_j - x_i)^2 + (y_j - y_i)^2} \quad (50)$$

Since line elements have no actual width, a fictitious cross section is assigned to each element and this permits the determination of volumetric flow rate, q, in the governing equation.

The basic component of the plane strain finite-element program used to model the continuum phase of the rock mass is the triangular element (Fig. 7). The shape function for this element has been derived by Desai and Abel (1972), Zienkiewicz and others. The derivation given here follows that of Zienkiewicz. The element is defined by three nodal points, i, j and k, numbered in a counterclockwise order. The displacements at each nodal point have two components:

$$\{\delta_i\} = \begin{Bmatrix} u_i \\ v_i \end{Bmatrix} \quad (51)$$

Each element has a total of six components of displacement:

$$\{\delta\}^e = \begin{Bmatrix} u_i \\ v_i \\ u_j \\ v_j \\ u_k \\ v_k \end{Bmatrix} \quad (52)$$

A linear relationship for displacements within the element is assumed in the form of

$$\begin{cases} u = \alpha_1 + \alpha_2 x + \alpha_3 y \\ v = \alpha_4 + \alpha_5 x + \alpha_6 y \end{cases} \quad (53)$$

where α_1 through α_6 are unknown coefficients. By substituting the coordinates of the nodal points and the appropriate nodal displacements and solving the resulting simultaneous equations, the general form of the displacements can be obtained.

The displacement functions in standard form are

$$\begin{Bmatrix} u \\ v \end{Bmatrix} = [N] \{\delta\} = [I N'_1, I N'_1, I N'_k] \{\delta\}^e \quad (54)$$

where I is a two by two identity matrix and

$$N'_i = (a_i + b_i x + c_i y) / 2 \Delta \quad (55)$$

with

$$\begin{cases} a_i = x_j y_k - x_k y_j \\ b_i = y_j - y_k \\ c_i = x_k - x_j \end{cases} \quad (56)$$

By cyclic permutation in equation (56) of the subscripts i, j and k , one may obtain a_j, b_j, c_j, a_k, b_k and c_k , and Δ equals the area of the triangle.

The shape function for the axisymmetric case is identical with that for the plane strain case with x and y being replaced by r and z in equations (55) and (56).

In the plane strain case, the appropriate components of strain are

$$\{\epsilon\} = \begin{Bmatrix} \epsilon_x \\ \epsilon_y \\ \gamma_{xy} \end{Bmatrix} = \begin{Bmatrix} \partial u / \partial x \\ \partial v / \partial y \\ \frac{\partial u}{\partial y} + \frac{\partial v}{\partial x} \end{Bmatrix} \quad (57)$$

where γ_{xy} is the shear strain and the independent terms of the stress tensor are

$$\{\sigma\} = \begin{Bmatrix} \sigma_x \\ \sigma_y \\ \tau_{xy} \end{Bmatrix} \quad (58)$$

where τ_{xy} is the shear stress.

In the axisymmetric situation, four components of strain have to be considered (Fig. 9)

$$\{\epsilon\} = \begin{Bmatrix} \epsilon_z \\ \epsilon_r \\ \epsilon_\theta \\ \gamma_{rz} \end{Bmatrix} = \begin{Bmatrix} \partial v / \partial z \\ \partial u / \partial r \\ u/r \\ \frac{\partial u}{\partial z} + \frac{\partial v}{\partial r} \end{Bmatrix} \quad (59)$$

and the corresponding four stresses

$$\{\sigma\} = \begin{Bmatrix} \sigma_z \\ \sigma_r \\ \sigma_\theta \\ \tau_{rz} \end{Bmatrix} \quad (60)$$

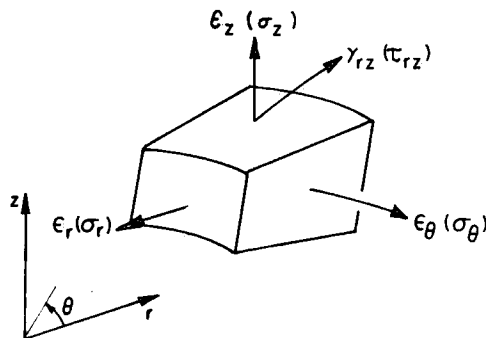


Figure 9. Axisymmetric element showing stress and strain components.

With the form of the shape functions known, the problem can be formulated. Using the method of weighted residuals, equations (18) and (19) can be written as

$$\int_V W_i \left(K_p \frac{\partial^2 p}{\partial x^2} \right) dv = 0 \quad (61)$$

$$\int_V W_i \left[\nabla \cdot [\sigma] + \rho_s (f) \right] dv = 0 \quad (62)$$

where W_i is the weighting factor. To simplify the calculations and to reduce the continuity requirements on the shape functions, the second differentials can be removed by partial integration. Thus equation (61) becomes

$$-\int_{V_p} \frac{\partial W_i}{\partial \ell} \left(K_p \frac{\partial p}{\partial \ell} \right) dv + \int_{S_p} W_i K_p \frac{\partial p}{\partial \ell} ds = 0 \quad (63)$$

where V_p is the domain of the fluid and S_p is the boundary on which fluid pressure is specified. Similarly, after replacement of $[\sigma]$ by $D \nabla \{u\}$ and integration by parts, equation (62) in terms of displacement becomes

$$\int_{V_u} \left\{ \left[D \left(\frac{\partial W_i}{\partial x} \frac{\partial u}{\partial x} + \frac{\partial W_i}{\partial y} \frac{\partial u}{\partial y} \right) \right] - W_i \rho_s (f) \right\} dx dy$$

$$- \int_{S_t} W_i \left(\frac{\partial u}{\partial x} n_x + \frac{\partial u}{\partial y} n_y \right) ds = 0 \quad (64)$$

where n_x and n_y are the direction cosines of the outward normals and V_u is the domain of the rock mass.

At this point, by application of the Galerkin method, by letting W_i in equation (63) equal ϕ_i and substituting the relationship given in equation (42), equation (63) becomes

$$\int_{V_p} \frac{\partial \phi_i}{\partial \ell} \left[K_p \frac{\partial}{\partial \ell} \left((\phi) \{P\} \right) \right] dv - \int_{S_p} \phi_i K_p \frac{\partial}{\partial \ell} \left((\phi) \{P\} \right) ds = 0 \quad (65)$$

Equation (65) can be written as

$$\int_{V_p} K_p \frac{\partial \phi_i}{\partial \ell} \left(\frac{\partial \phi_i}{\partial \ell} P_i + \frac{\partial \phi_j}{\partial \ell} P_j \right) dv - \int_{S_p} \phi_i \bar{q} ds = 0 \quad (66)$$

where \bar{q} is a prescribed flow rate. Advantage has been taken of the condition that the integral over the external surface does not contribute anything to the equations that are written for the internal flow nodal points. Thus, when the nodal point lies on the boundary, either the flow rate or the fluid pressure is known at that point and thus equation (66) can be solved at all nodal points. The contribution of all the elements to the integrals given in equation (66) can be expressed in matrix form as

$$[K_f] \{P\} - \{Q\} = 0 \quad (67)$$

where $[K_f]$ is the fluid conductivity matrix written as

$$[K_f] = \sum \sum K_p \frac{\partial \Phi}{\partial \ell} \left(\frac{\partial \Phi_i}{\partial \ell} + \frac{\partial \Phi_j}{\partial \ell} \right) \quad (68)$$

and is summed over the entire region.

From equations (48) and (49)

$$\frac{\partial \Phi_i}{\partial \ell} = -\frac{1}{L} \text{ and } \frac{\partial \Phi_j}{\partial \ell} = \frac{1}{L} \quad (69)$$

In a similar manner, Galerkin's method can be applied to equation (64) where W_i equals N_i , and making use of equation (43)

$$\int_{V_u} \left[D \left(\frac{\partial [N_i]}{\partial x} \frac{\partial ([N] \{\delta\})}{\partial x} + \frac{\partial [N_i]}{\partial y} \frac{\partial ([N] \{\delta\})}{\partial y} \right) \right] dx dy - \int_{V_u} [N_i]^T \rho_s (f) dx dy - \int_{S_t} [N_i]^T \left(\frac{\partial [N] \{\delta\}}{\partial x} n_x + \frac{\partial [N] \{\delta\}}{\partial y} n_y \right) ds = 0 \quad (70)$$

The stiffness matrix of element $i j k$ is defined as

$$[K]^e = \int [B]^T [D] [B] dx dy \quad (71)$$

where

$$[B] = \begin{bmatrix} \frac{\partial N_i'}{\partial x} & 0 & \frac{\partial N_j'}{\partial x} & 0 & \frac{\partial N_k'}{\partial x} & 0 \\ 0 & \frac{\partial N_i'}{\partial y} & 0 & \frac{\partial N_j'}{\partial y} & 0 & \frac{\partial N_k'}{\partial y} \\ \frac{\partial N_i'}{\partial y} & \frac{\partial N_i'}{\partial x} & \frac{\partial N_j'}{\partial y} & \frac{\partial N_j'}{\partial x} & \frac{\partial N_k'}{\partial y} & \frac{\partial N_k'}{\partial x} \end{bmatrix} \quad (72)$$

is obtained by differentiating equation (57). The second integral in equation (70) represents the nodal forces owing to the body forces, and the third integral represents the distributed forces acting on the surfaces. For the entire region

$$[K]^r = \sum [K]^e \quad (73)$$

Thus equation (70) can be expressed in matrix form as

$$[K]^r \{\delta\} - \{F\} = 0 \quad (74)$$

By using the direct stiffness method, the contribution of the joints to deformation in the rock mass can be added to equation (74). As discussed earlier, the stiffness matrix for the joint element was derived by Goodman, Taylor and Brekke from an energy equation. The displacements $\{u\}$ are expressed in terms of nodal point displacements $\{\delta\}$ by a linear interpolation formula. The stiffness matrix in standard form is

$$[K]^e = [B_J]^T [K_J] [B_J] \quad (75)$$

where

$$[B_J] = \begin{bmatrix} -A & 0 & -B & 0 & B & 0 & A & 0 \\ 0 & -A & 0 & -B & 0 & B & 0 & A \end{bmatrix}$$

with

$$A = 1 - \frac{2x}{L} \quad \text{and} \quad B = 1 + \frac{2x}{L}$$

Since the joint nodal points have the same number of degrees of freedom as the nodal points for the rock block elements bounding the joint or fracture, the contribution of the joints can be added directly to equation (74), thus giving the general equation for displacements in the rock mass

$$[K] \{\delta\} - \{F\} = 0 \quad (76)$$

The normal forces owing to flow in the fractures are derived by equating the fluid pressures in the fractures to equivalent nodal point forces (Noorishad, Witherspoon and Brekke, 1971). The same forces are assigned to opposite nodal points in a fracture element. The tangential forces within the fracture as a result of shear stresses in the fluid can be disregarded.

Since fractures are deformable, an increase or decrease in fluid pressure changes the width of the fractures. Thus the fluid conductivity matrix is dependent on the displacements in the rock mass. Also, the fluid pressures contribute to the nodal point forces. The two matrix equations describing flow in the fractures and displacements in the rock mass can be written as

$$[K_f(\delta)] \{P\} - \{Q\} = 0 \quad (77)$$

and $[K] \{\delta\} - \{F(P)\} = 0 \quad (78)$

These two equations are coupled in terms of the fluid pressures and displacements and are highly nonlinear. Thus these equations cannot be solved simultaneously and an iterative method of solution must be used. The iterative method employed is described in the following section.

PROCEDURE FOR ANALYZING FLOW IN DEFORMABLE FRACTURE SYSTEMS

General Approach

Using a numerical approach as outlined in this Chapter, an analysis of fluid flow in a deformable fracture system can be made that depends on the availability of data, the geometry of the fractures and their material characteristics. Determination of the flow characteristics for the fractures must also be possible. Thus the first step in the computer analysis is to describe the geometry of the fracture system. This is accomplished either by using available field data on fracture orientation and spacing or by assuming a certain fracture geometry. The computer program can handle multiple fracture sets with any orientation and spacing. The amount of computer storage available is the limiting factor. A finite-element mesh is prepared in which each fracture is represented by one or more fracture elements, depending on the degree of mesh refinement required. This subdivision or mesh refinement can also be applied to the finite-element representation of the individual rock blocks. The description of the finite-element mesh is supplied to the computer by assigning the spatial coordinates of nodal points and a list of the nodal points that define each finite element.

The material characteristics of the rock blocks can be assessed by performing appropriate laboratory tests or field tests on suitably prepared samples of the intact rock. The mechanical behaviour of the fractures can be ascertained both in the field and in laboratory tests. It is very difficult to obtain a rock sample enclosing an undisturbed natural fracture. Field sampling techniques have improved greatly in the past few years (Goodman, 1974), but nearly all sampling techniques result in some disturbance of the fracture surface. As shown in Chapter 3, instrumentation developed during this investigation may permit the determination of the normal force-displacement relationship of a fracture *in situ*.

The averaged flow characteristics of the individual fractures can be determined from injection tests (Snow, 1965; Maini, 1971; Louis, 1974), with the best results being obtained when the injection holes are oriented orthogonally to the fracture sets. As pointed out by Maini and Louis, the excess injection pressure used in performing such tests should be only a small percentage of the initial fluid pressure at the injection point. Based on the injection test results, initial fracture apertures can be assigned either individually or by specifying the parameters of a random distribution. For idealized systems, the usual practice is to assign an initial set of uniform fracture apertures.

The structural and flow boundary conditions for the problem being considered are specified by assigning either initial boundary loads or displacements at structural nodal points and either pressures or flow rates at specified flow nodal points. In addition, the boundaries can be constrained to move only in a given direction.

The initial stresses in the rock mass being studied can be incorporated in the finite-element model. This is accomplished in horizontal sections by assigning to each rock block and fracture element the appropriate values of the stresses parallel to both global coordinate axes. These stresses interact with the specified shear stresses to produce a stress field of the correct magnitude and orientation. The normal stresses acting across the fractures are modified to account for the initial fluid pressures within the fracture system. In this manner, an initial effective normal stress is assigned to the entire fracture system. The same approach is used for vertical sections and axisymmetric bodies except that the stresses are calculated and assumed to be due to gravity forces, although additional forces such as high horizontal stresses can be included.

Figure 10 presents the general iterative procedure for the coupled numerical stress-flow analysis of a fractured rock mass subject to gravity loads. As discussed above, the initial conditions are described first. The analysis is started by obtaining a solution for the displacements that are due to gravity forces. In the analysis of two-dimensional horizontal sections, this step is omitted as are all other steps in the flow

chart that refer to gravity loads. From this point, problems involving gravity loads and horizontal sections are solved in the same manner. The discussion that follows primarily covers problems resulting from gravity loads.

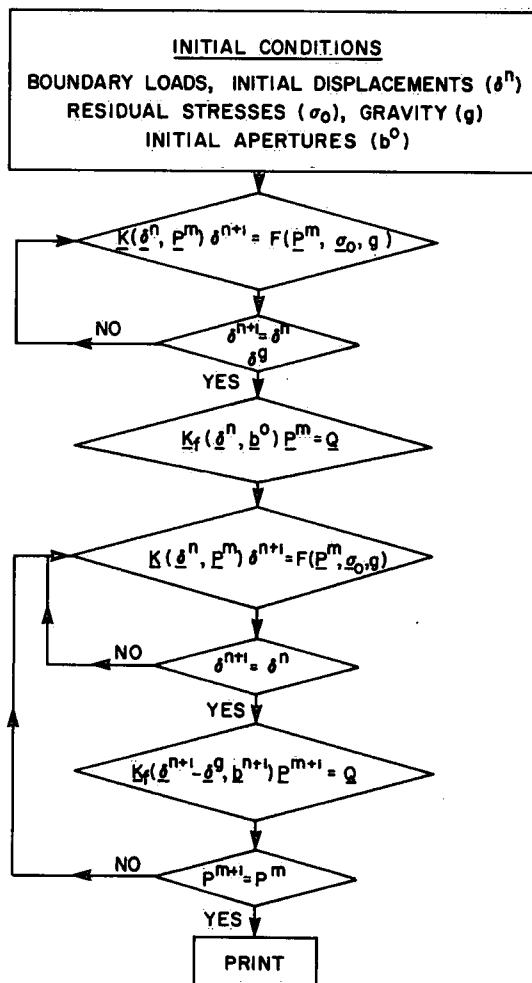


Figure 10. Flow chart for coupled stress-flow analysis.

After having obtained the displacements that are due to gravity (δ^g), the second step in the analysis is to determine the fluid pressure distribution (P^m) within the fracture system, based on the initial set of fracture apertures (b^0) and the given flow boundary conditions (Q). It should be noted that this pressure distribution is equivalent to that which would be calculated if we assumed that the fractures were rigid.

The third step is to use the pressure distribution (P^m) to calculate generalized nodal point forces at each of the corresponding structural nodal points. A displacement analysis of the fractured rock mass, based on the initial stress and displacement conditions and the forces created by the fluid pressures and gravity loads, is then made in order to calculate the displacement field. It should be noted that since the finite-element method

used in this analysis is formulated in terms of the displacement approach, the stresses are determined by considering the relative displacements of all the structural nodal points in a given element.

Since the fractures have a nonlinear behaviour (Figs. 5 and 6), a solution cannot be reached in one step. Therefore a joint (fracture) perturbational technique of Heuzé, Goodman and Borenstein (1971) is utilized in which the fracture properties are continuously updated depending on the latest state of deformation in the system. Accordingly, the displacement field determined by each analysis is compared with the previous value and convergence is assumed when the difference between two consecutive results is less than a specified tolerance. The displacements owing to gravity forces, which were calculated in the first analysis, are then subtracted from the final displacement field obtained in this third step. This modified displacement field ($\delta^{n+1} - \delta^g$) represents the displacements on account of the fluid pressures and is used to determine a new set of fracture apertures (b^{n+1}).

The fourth step is a repetition of the second step, but the fluid pressures are now determined for the new set of fracture apertures (b^{n+1}). If this new fluid pressure distribution (p^{m+1}) differs by a significant amount from the previous set of fluid pressures (p^m), then step three is repeated using the generalized nodal point forces determined from the new set of fluid pressures (p^{m+1}). This process is repeated until the difference between two consecutive pressure distributions decreases to an acceptable level. At this point, the final steady-state solution is assumed. The computer program then prints the displacements at each structural nodal point, the magnitude and orientation of the principal stresses within each rock block, and the effective normal and shear stress within each fracture element, as well as changes in fracture apertures, fluid pressures at all flow nodal points of the network and flow rates at the boundaries. An additional option in the program permits plotting of the mesh and the stress vectors within each element.

The rate of convergence of this iterative approach is quite rapid and depends largely on the relative stiffness of the rock-fracture system and the ratio of the existing state of stress to the change in fluid pressure. For the fractured rock systems investigated, three or four iterations were sufficient to obtain a solution.

This numerical approach will now be used to study the effects of fracture deformation on fluid pressure distribution and flow rates for both fluid injection and fluid withdrawal in several idealized fracture systems.

Results from a Simple Axisymmetric Model

Finite-element analyses of systems with complex configurations present difficulty in comprehension of the physics involved and understanding of the method of analysis used.

Thus a simple axisymmetric model is presented here to introduce the principles involved in a study of fluid injection and fluid withdrawal in an axisymmetric, deformable, fractured rock mass subject to gravity body loads.

The demonstration model consists of a single horizontal fracture bounded by two rock blocks. The finite-element mesh and the structural and flow boundary conditions are shown in section A of Figure 11. The upper and lower rock blocks are divided into 20 rock elements, and the horizontal fracture is divided into 5 fracture elements. The radius of the well is 0.125 ft and the structural and flow boundaries are assumed to be located at a radial distance of 100 ft. The well is assumed to penetrate to a depth of 40 ft and the fracture is located at a depth of 20 ft. The bottom corner of the model, farthest from the well, is fixed in space. Horizontal and vertical movements are permitted at all other structural nodal points except that vertical movement is not permitted along the bottom of the model and horizontal movement is not permitted on the outer boundaries. Flow in the fracture was induced by increasing (injection) or decreasing (withdrawal) the fluid pressure at the flow nodal point formed by the intersection of the fracture with the well.

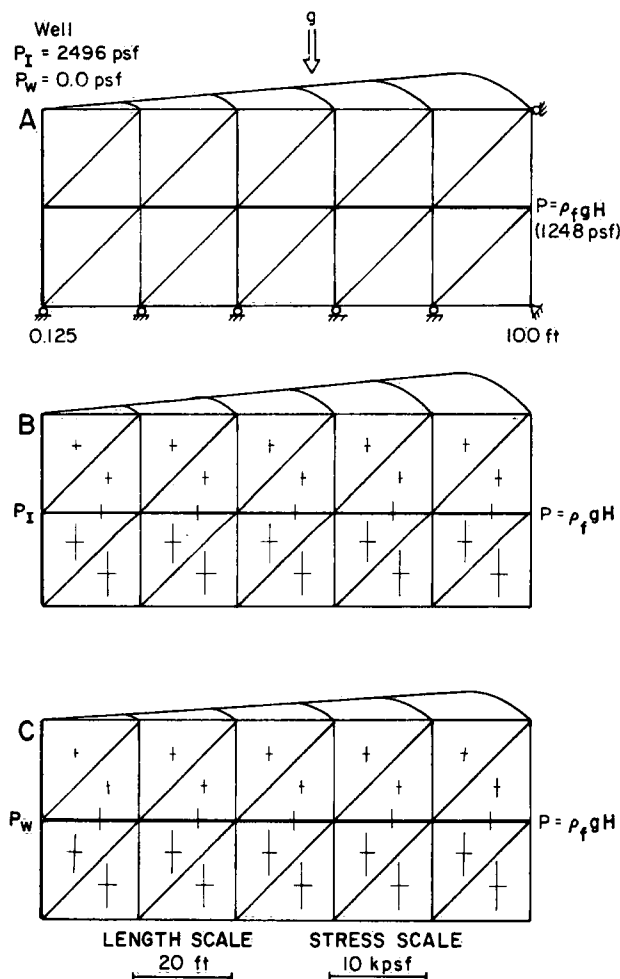


Figure 11. Simple axisymmetric model:
 A - structural and flow boundary conditions;
 B - effects of fluid injection;
 C - effects of fluid withdrawal.
 Maximum and minimum principal stresses are shown by scaled line vectors within each block; effective normal stress is depicted by vertical line segment across each fracture.

The radius of influence is assumed to be equal to 100 ft, where the fluid pressure is approximately hydrostatic.

The fracture was given an initial aperture of 0.001 ft. Two different fracture strengths were investigated by setting the normal stiffness of the fractures equal to (a) 4.72×10^7 psf/ft and (b) 4.72×10^6 psf/ft. The shear stiffnesses were set equal to the normal stiffnesses, since the changes in shear stress were very small in the examples studied. Other material properties were kept constant. The rock matrix was assigned a Young's modulus of 4.72×10^8 psf and a Poisson's ratio of 0.28. A value of 165 lb/ft³ was used for the specific weight of the rock. The fracture stiffness values were, respectively, one and two orders of magnitude less than the rock matrix modulus, so that the fractures could be considered slightly deformable and very deformable, respectively (Goodman, Taylor and Brekke, 1968). The angle of friction in the joint plane was set at 38°.

The results of the model studies are presented as scaled computer plots in Figure 11 (sections B and C). The orientation and magnitude of the maximum and minimum principal stresses are plotted as scaled line segments within each solid block. The normal stress minus the average fluid pressure is plotted for each fracture. The tangential stresses within the fracture are not shown. These plots have been modified to a pie-shaped wedge, where each element forms a body of revolution, indicating the axisymmetric nature of the model.

Injection of fluid in this model was simulated by assigning an excess pressure of 1,248 psf to the flow nodal point at the well. This is equal to a change in hydraulic head of 20 ft. The principal compressive stresses plotted in section B of Figure 11 were calculated as a result of the gravity body loads and the forces developed by fluid injection. Note the decrease in the effective normal stress acting across the fracture elements near the well.

The withdrawal of fluids from the fracture was simulated by assigning a fluid pressure of 0.0 psf to the flow nodal point at the well. This change in fluid pressure is equal to the pressure that would be developed by a 20-ft drawdown. The principal compressive stresses that resulted from the interaction of the change in fluid pressures owing to fluid withdrawal and the gravity body loads are shown in section C of Figure 11. Both stress plots are for the slightly deformable fracture system.

Comparison of the plots in sections B and C of Figure 11 demonstrates that there is an increase in the effective normal stress across the fractures during fluid withdrawal and a decrease in effective normal stress during fluid injection. Table 1 shows the changes in aperture at the well bore and the calculated flow rates corresponding to the effects of

injection and withdrawal in both deformable fracture systems. For comparison, the results for the corresponding rigid fracture system are also included. The changes in aperture at the well bore, based on calculated structural nodal point displacements, are of the order of $\pm 10^{-4}$ ft.

Table 1. Results from Injection and Withdrawal in a Simple Axisymmetric Model

	Slightly deformable ($K_N = 4.72 \times 10^7$ psf/ft)		Very deformable ($K_N = 4.72 \times 10^6$ psf/ft)		Rigid fracture
	Injection	Withdrawal	Injection	Withdrawal	
Change in aperture 2b at well (10^{-3} ft)	+0.05529	-0.05572	+0.11198	-0.1007	0.0
Q (10^{-3} cfs)	+4.282	-4.0065	+5.1823	-3.3408	± 4.1421
Change in pressure at well (psf)	+1,248	-1,248	+1,248	-1,248	$\pm 1,248$

For the slightly deformable fracture system, the flow rates tabulated in Table 1 indicate that the flow rate during injection is 7% greater than that during withdrawal for an equivalent change in fluid pressure at the well bore. In addition, the flow rate calculated for an equivalent rigid fracture system differs by only $\pm 3\%$ from the flow rates associated with injection and withdrawal.

With a decrease in fracture strength of one order of magnitude, the difference between injection and withdrawal in a rigid and a deformable fracture system becomes more obvious. For the very deformable fracture system, the change in aperture at the well bore is approximately twice that calculated for the slightly deformable system for the same pressure changes. This is reflected in the flow rates by an increase of 55% in the volume of fluid accepted by the fracture on injection as compared with that produced on withdrawal. In addition, the flow rates associated with injection and withdrawal in the very deformable fracture system differ by approximately +25% and -19%, respectively, from those calculated for an equivalent rigid fracture system.

Thus it is obvious that injection and withdrawal are not reversible processes in deformable fracture systems. This suggests that the behaviour of an injection well cannot be predicted from pumping-out tests and the yield of a production well cannot be estimated from injection tests unless the change in fluid pressure at the well bore is kept at a minimum.

FLUID INJECTION AND FLUID WITHDRAWAL IN A DEFORMABLE FRACTURE SYSTEM

The foregoing simple model serves only to introduce some of the principles involved in this study. Two, more complex, fractured rock models will now be used to study the distribution of fluid pressure within the fracture system and the corresponding flow rates. These are (1) an axisymmetric model of a horizontal fracture system and (2) a two-dimensional horizontal section containing two vertical, orthogonal fracture sets.

Fluid Pressure Distributions and Flow Rates in a Horizontal Fracture System

The fracture model selected is depicted in Figure 12. The distribution of fractures is similar to that observed at the field test site near Sambro, Nova Scotia. The fracture system and the test site are discussed in some detail in Chapter 3. The fracture system has been idealized as seven discrete horizontal fractures intersecting a 50-ft deep well. Although the fracture distribution in this model is similar to that observed at Sambro, the model is not intended to duplicate the field behaviour; this is done in Chapter 4.

For the purposes of this study, it has been assumed that this sequence is representative of the fracture system intersected by a well over a range of depths from 200 ft to 250 ft below the ground surface. Thus, the forces owing to gravity acting on the system correspond to the forces at that depth. It is assumed that each fracture has a uniform opening of 0.001 ft. The material properties of the rock blocks are assumed similar to the properties of some granitic rocks, i.e., a Young's modulus of 4.72×10^8 psf and a Poisson's ratio of 0.28. The initial fluid pressure within the fracture system is assumed to be hydrostatic with the water table at the ground surface, i.e., $P = \gamma_f H$, where H is the depth below the ground surface and γ_f is the unit weight of water. The well has a diameter of 0.25 ft. In this example it is assumed that a constant head boundary exists at a radial distance of 150 ft.

Two hypothetical fracture stiffness values, $K_N = 9.72 \times 10^7$ psf/ft and $K_N = 4.72 \times 10^7$ psf/ft, were used, and these fractures are referred to as stiff and slightly deformable, respectively. The shear stiffness was set equal to the normal stiffness for each fracture system. The angle of friction within the fracture plane was set at 38° .

This model has been used to investigate how the flow rates in a deformable fracture system differ from those in a rigid system. Figure 13 shows the ratio of the total flow in the deformable fractures to that in the rigid system versus the change in hydraulic head (water level) at the well for both fluid injection and withdrawal. For

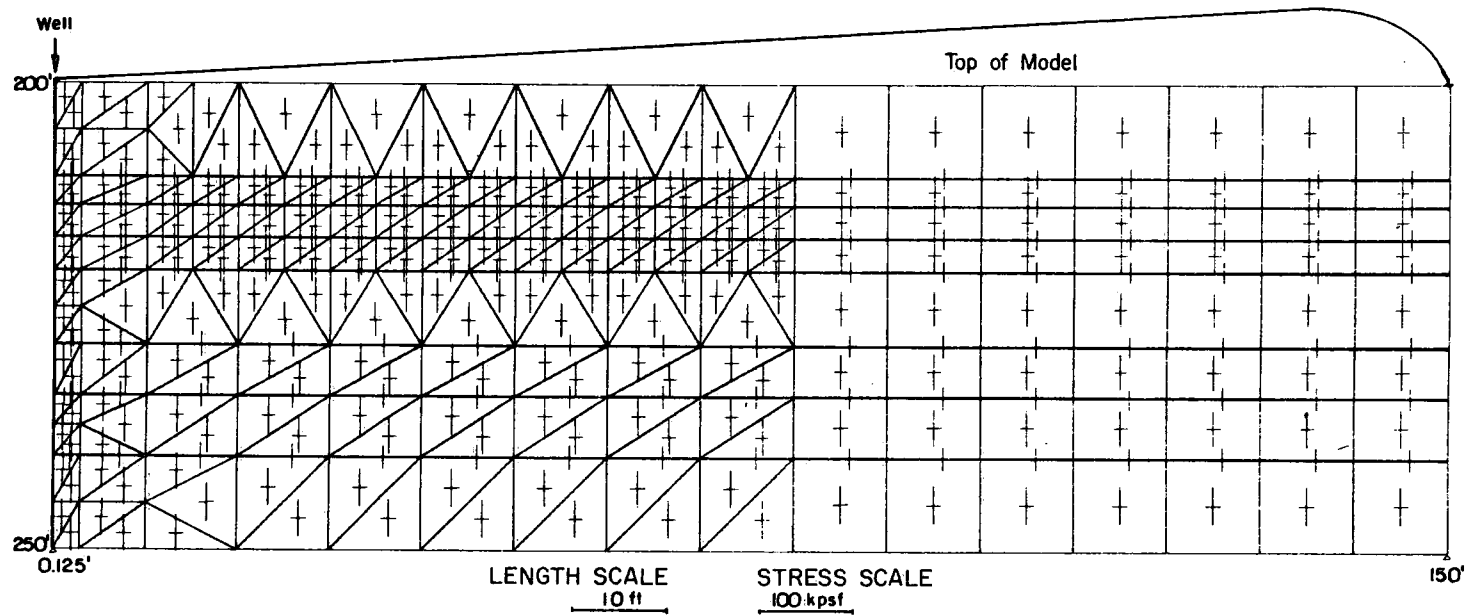


Figure 12. Finite-element model showing the distribution of principal stresses in the rock blocks and the effective normal stresses acting across the fractures. Maximum and minimum principal stresses are shown by scaled line vectors within each block; effective normal stress is indicated by vertical line segment across each fracture.

reference purposes, the flow into or out of the rigid system for each change in hydraulic head is also tabulated in Figure 13.

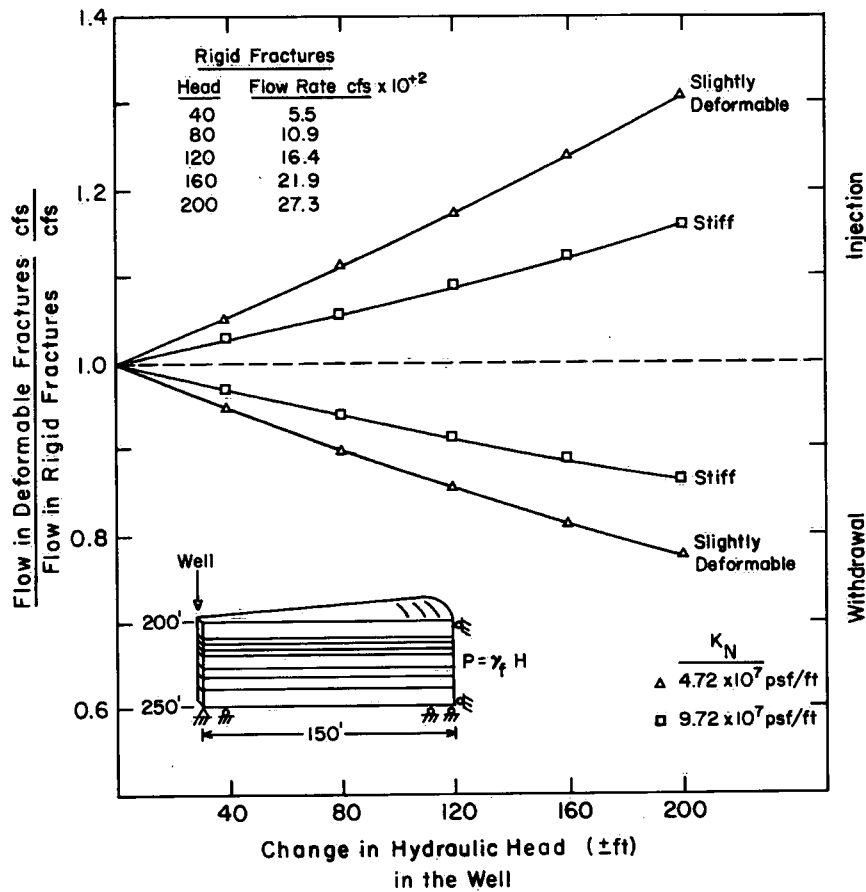


Figure 13. Comparison of flow rates for fluid injection and withdrawal in a fracture system for two different fracture strengths.

In Figure 13 there is a significant change in the flow rate with a change in fracture stiffness. Also, injection and withdrawal of fluid are not reversible processes. For a pressure increase equivalent to 200 ft of water, there is approximately a 30% increase in the volume of water injected in the case of the slightly deformable fracture system as compared with that of the rigid system. But when the water level in the well is lowered by 200 ft, there is only a 22% decrease in the flow rate.

Figure 14 shows pressure variation with radial distance from the well expressed as a percentage of the injection or withdrawal pressure for a change in the water level at the well of ± 200 ft. In Figure 14 the pressure profiles for injection and withdrawal in

a rigid fracture system are mirror images. This is no longer true if the fractures are allowed to deform. In the case of fluid injection, the fractures open up and the pressures are propagated a greater distance from the well. In the case of fluid withdrawal, the opposite is true; the decrease in pressure increases the effective normal stress acting across the fracture and hence the fractures near the well close to some extent. This results in an increase in the pressure gradients near the well and hence a reduction away from the well.

The results for the stiff fracture system are not given on Figure 14, since they fall between those of the rigid and the slightly deformable fracture systems.

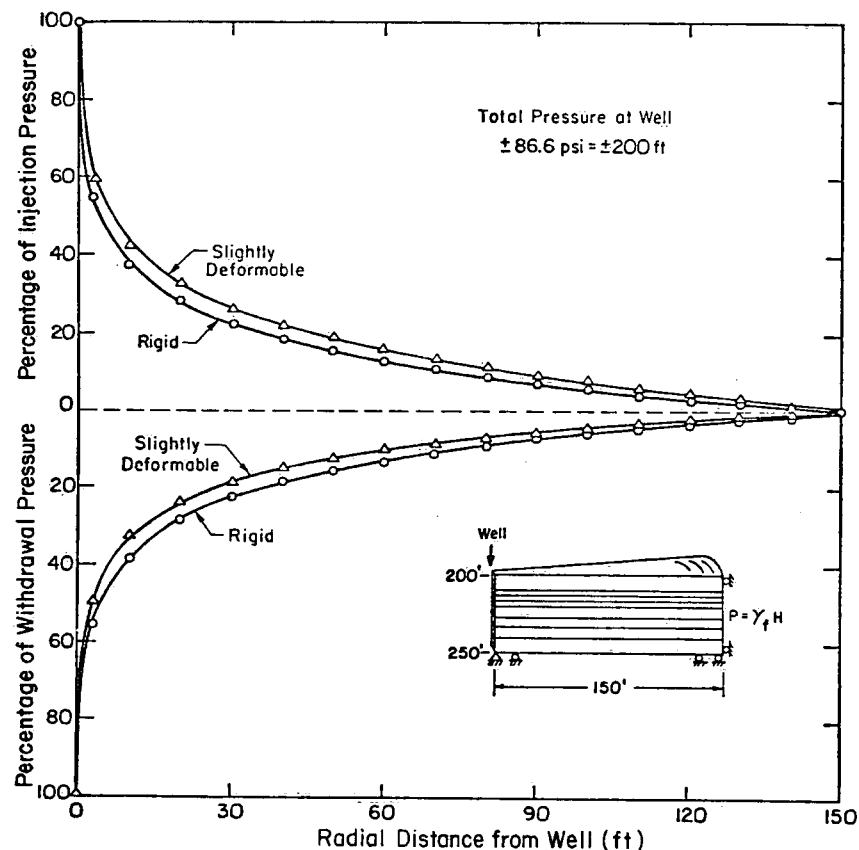


Figure 14. Fluid pressure profiles for fluid injection and withdrawal in rigid and deformable fracture systems.

Fluid Pressure Distributions and Flow Rates in a Vertical Fracture System

To demonstrate further the effects of fracture deformation on pressure distribution and flow rates, a second model was studied. This model consists of two vertical,

orthogonal fracture sets intersecting a horizontal plane. The fractures are assumed to be spaced 200 ft apart and have a uniform fracture aperture of 0.001 ft. The model is 2,000 ft by 2,000 ft and is of unit thickness in the vertical direction (Fig. 15). Fluid was injected and withdrawn from the centre of the fracture model by increasing and decreasing the pressures by 12,480 psf, respectively.

The rock blocks were assigned a Young's modulus of 4.72×10^8 psf and a Poisson's ratio of 0.28. A uniform compressive stress of 28,800 psf was assigned to each rock block and fracture element. It was assumed that the initial fluid pressure within the system was equal to 12,480 psf. Thus the initial effective normal stress within the fracture system was 16,320 psf. The stress field is representative of that found at approximately 500 ft below the ground surface where the stresses are due only to the weight of the overlying rock.

The structural boundary conditions consisted of fixing the four corners of the model in space and elsewhere permitting movement parallel, but not perpendicular, to the boundaries. The flow boundary conditions consisted of assigning a constant pressure equal to the initial pressure at all the flow nodal points on the boundaries.

Three different normal stiffness values were used for the fractures and were assigned the following descriptive terms: stiff, $K_N = 9.72 \times 10^7$ psf/ft; slightly deformable, $K_N = 4.72 \times 10^7$ psf/ft; and very deformable, $K_N = 9.72 \times 10^6$ psf/ft. In all three cases the shear stiffness (K_S) was set equal to the assigned normal stiffness and the angle of friction was 38° .

The finite-element mesh used is depicted in Figure 15 in which the solid continuous lines represent fracture elements. This Figure is a computer plot showing how the initial uniform stress field was altered by the reduction of fluid pressures and the corresponding increase in effective normal stress resulting from fluid withdrawal. The principal stress vectors have been plotted in each rock element and the effective normal stresses have been plotted across each fracture. Note the decrease in effective normal stress as distance from the withdrawal point increases. This indicates that the fractures near the well are closing more than the fractures farther away.

Figure 16 shows the computer plot of the stress field for the same fracture system when fluid is injected at the centre of the model. In this case, the effective normal stresses are smaller near the injection point. Thus the fractures near the well open more. In both the withdrawal and injection cases, note the symmetry of the stress field.

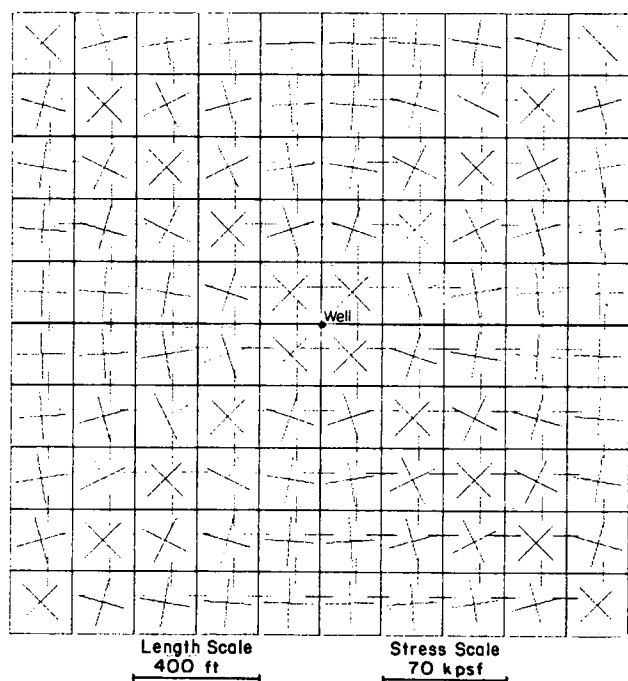
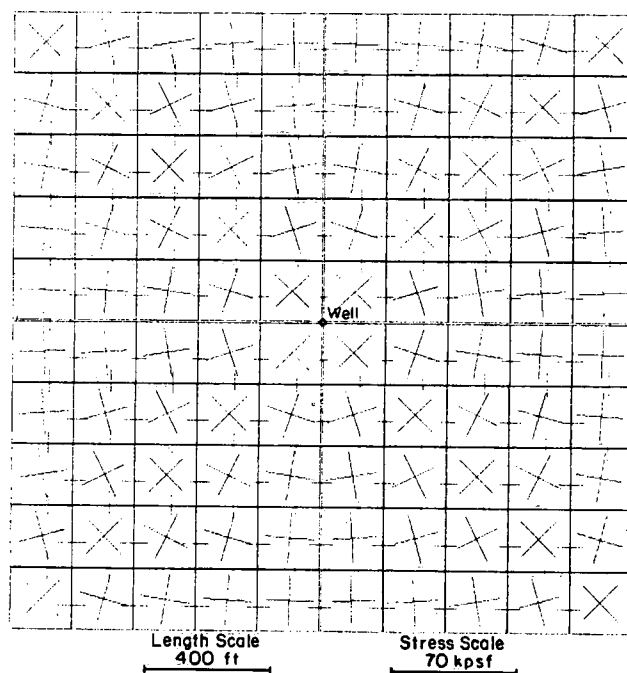


Figure 15. Distribution of stresses in a rock mass containing two vertical orthogonal fracture sets (withdrawal). Maximum and minimum principal stresses are shown by scaled line vectors within each block; effective stresses normal to fractures are indicated by line segments across fractures.

Figure 16. Distribution of stresses in a rock mass containing two vertical orthogonal fracture sets (injection). Maximum and minimum principal stresses are shown by scaled line vectors within each block; effective stresses normal to fractures are indicated by line segments across fractures.



The distribution of fluid pressures in a given fracture system is strongly dependent on the stiffness of the fracture system. This is shown by comparing the pressure profiles along a centre fracture intersecting the well. Pressure profiles for three different fracture stiffnesses for both injection and withdrawal (increase and decrease of fluid pressure at the well of 12,480 psf, respectively) are presented in Figure 17. In the case of fluid injection, as the fracture stiffness decreases the fractures open more and the pressures are propagated increasingly greater distances from the well. In the case of fluid withdrawal, as the fracture stiffness decreases the fractures close and steeper pressure gradients develop near the well. This difference between the effects of injection and withdrawal is more clearly evident in Figure 18 where the isopotentials around the well are plotted as percentages of injection or withdrawal pressure. These plots are for the

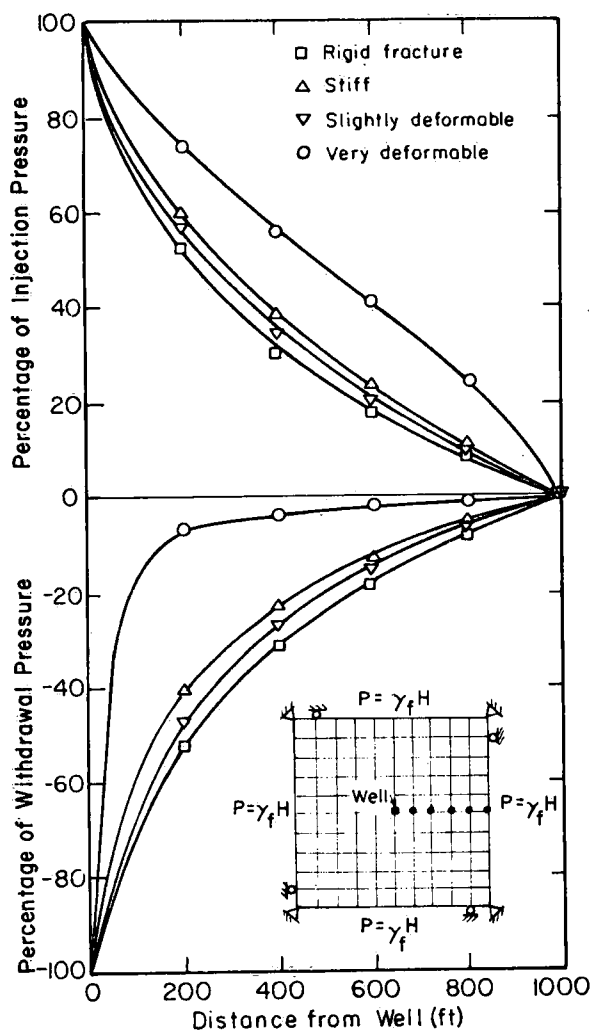


Figure 17. Comparison of fluid pressure distribution along the centre fracture for injection and withdrawal in rigid and deformable orthogonal fracture systems.

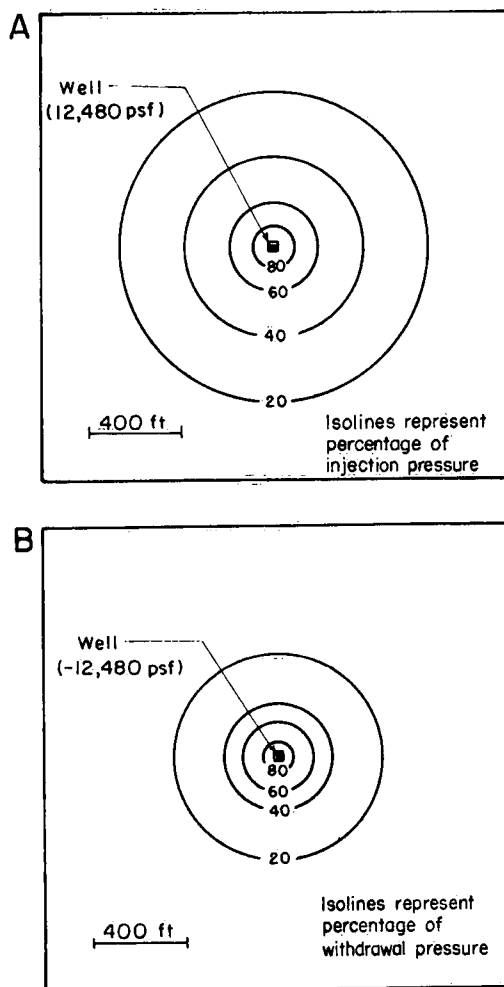


Figure 18. Distribution of fluid pressure for fluid injection and fluid withdrawal in a slightly deformable orthogonal fracture system.

slightly deformable fracture system. They show that the area over which the pressures are affected during withdrawal is 44% less than the area so affected during injection. The 20% isopotential line is arbitrarily used as the basis for this comparison.

The opening or closing of fractures and the increase or decrease in pressure gradients affect the flow rates in the fracture system (Table 2). In Table 2 as the fracture stiffness decreases there are both a significant increase in flow rate during injection and a significant decrease during withdrawal.

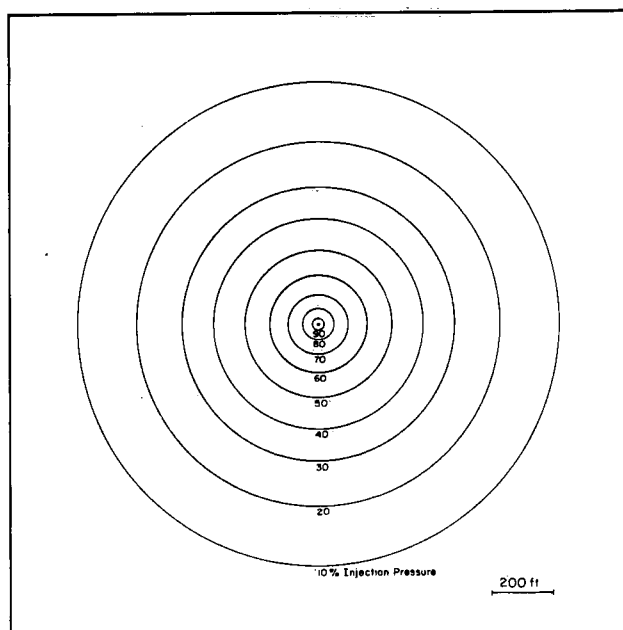
Table 2. Flow Rates for Injection and Withdrawal in an Orthogonal Fracture System with Different Fracture Stiffness Values

Fracture type	Fracture stiffness (psf/ft)		Flow rate (10^{-4} cfs)	
	Normal K_N	Shear K_S	Injection +12,480 psf	Withdrawal -12,480 psf
Rigid	-	-	4.198	-4.198
Stiff	9.72×10^7	9.72×10^7	5.058	-3.466
Slightly deformable	4.72×10^7	4.72×10^7	6.076	-2.835
Very deformable	9.72×10^6	9.72×10^6	16.480	-0.458

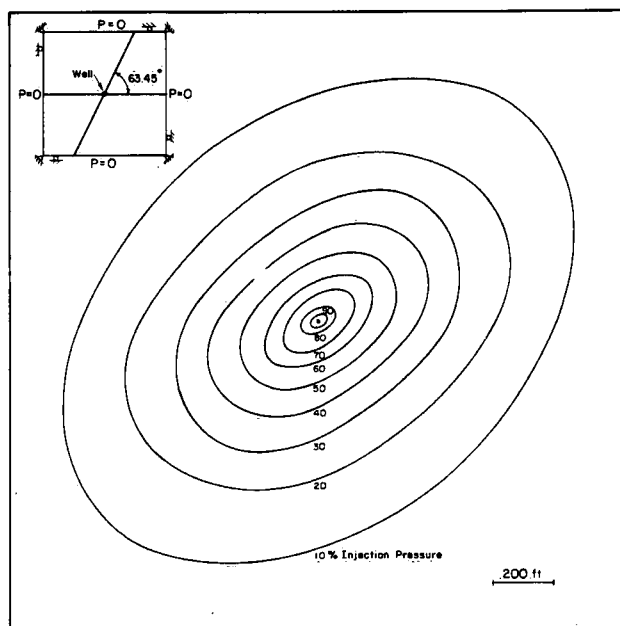
The two examples presented here, which are (1) a horizontal system with no vertical fractures and (2) a vertical system with no horizontal fractures, are probably end members of the actual systems that are found in nature. A combination of both vertical and horizontal fractures is usually encountered, although it has been suggested that vertical fractures are the dominant mode in deep reservoirs (Daniel, 1954; Wilkinson, 1953). In any event, a completely three-dimensional model would be required to simulate flow in both vertical and horizontal fractures under axisymmetric conditions. The main objective here has been to show how the pressures and flow rates are affected by allowing the fractures to deform.

Other factors, such as the angle of fracture intersection and the distribution of apertures, affect the fluid pressure distribution. In a more detailed investigation, Witherspoon *et al.* (1974) studied the effects of varying the angle of intersection between two vertical fracture sets. Their results for fluid injection for four different fracture intersection angles are given in Figure 19. They show that the axes of the fluid pressure ellipses do not necessarily coincide with the mechanical anisotropy indicated by the fracture orientations. These results are for a fracture system where K_N is one fourth and K_S is one tenth of the rock modulus, respectively. An initial uniform stress of 20,000 psf, an injection pressure of 14,400 psf and an initial fluid pressure of zero within the fractures were used in their study.

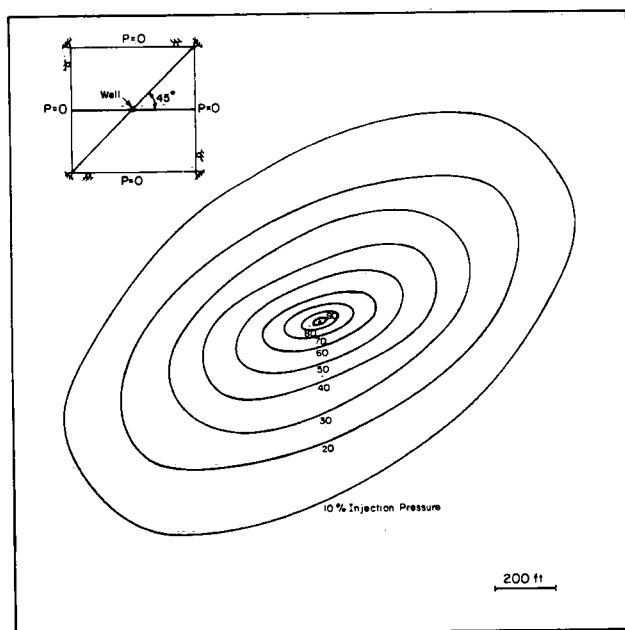
A



B



C



D

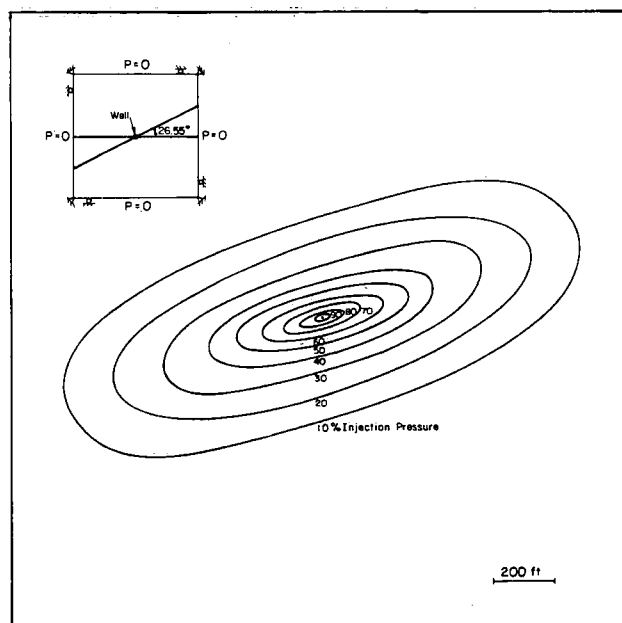


Figure 19. Effect of fracture intersection angle on pressure distribution: A - 90° , B - 63.45° , C - 45° , D - 26.55° (after Witherspoon *et al.*, 1974).

Although these isopotentials (Fig. 19) are for idealized systems, they indicate the difficulty encountered in determining and interpreting the fluid pressure distributions during pump tests in fractured rocks.

Effects of Nonuniform Fracture Apertures

In the previous models it has been assumed that all fractures have the same initial aperture (2b). When fractures in outcrops are examined, a uniform fracture aperture is the exception rather than the rule, even over distances of only a few feet. Fracture apertures determined from an analysis of injection test data are based on averaged flow characteristics and a uniform variation in fluid pressure between the injection point and the observation well or the flow boundary. If pressures at some nearby well are measured and these values are compared with those predicted on the basis of a uniform aperture, a significant difference is sometimes found between the observed and predicted results (Chapter 3).

This pressure difference can be explained using simple fluid mechanics principles. For example, Figure 20 shows two pressure profiles, one for flow in a pipe of uniform diameter and the other for a pipe with a nonuniform diameter. It is apparent that the nonuniform pipe has a much smaller head loss over the large-diameter section than has the corresponding length of pipe with the uniform diameter. Thus a well intersecting a fracture in which the aperture decreases at some distance from the well would show a similar nonuniformity in the pressure profile during injection or withdrawal. This means that significantly higher pressures will occur at some distance from the well than are predicted on the basis of observation of the fracture at the well. Since the pressures multiplied by the area over which they are acting represent the force available to deform the fracture, it can easily be seen that the forces that develop in the case of a nonuniform aperture

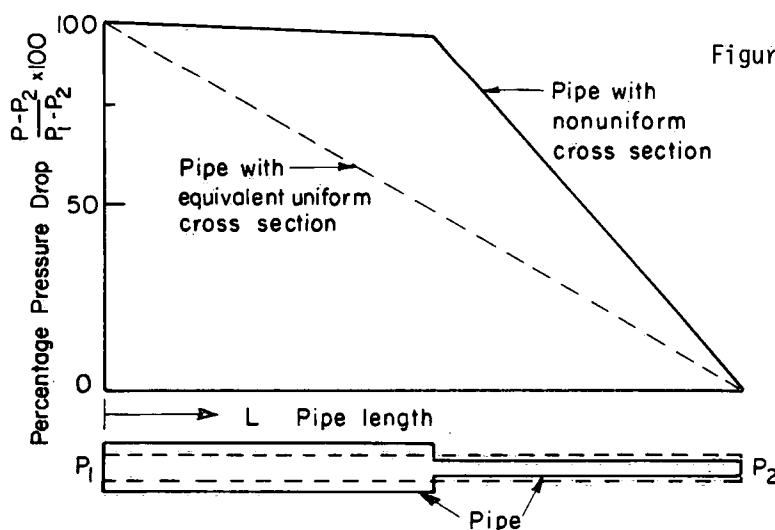


Figure 20. Schematic of pressure profiles for flow in pipes with equivalent uniform and nonuniform cross sections.

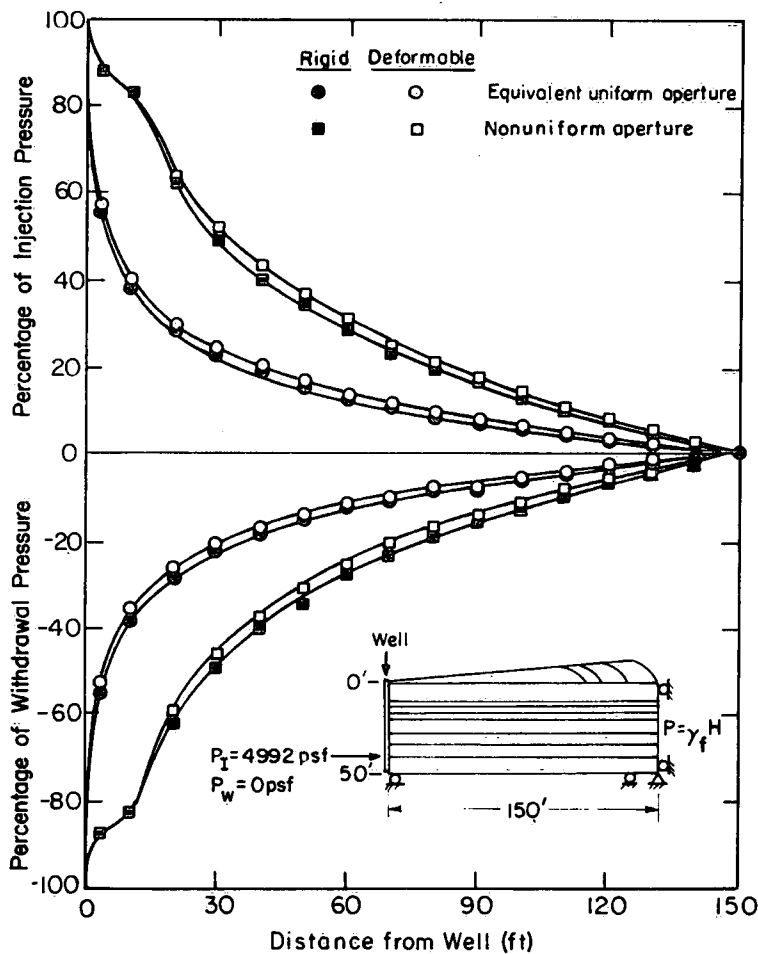
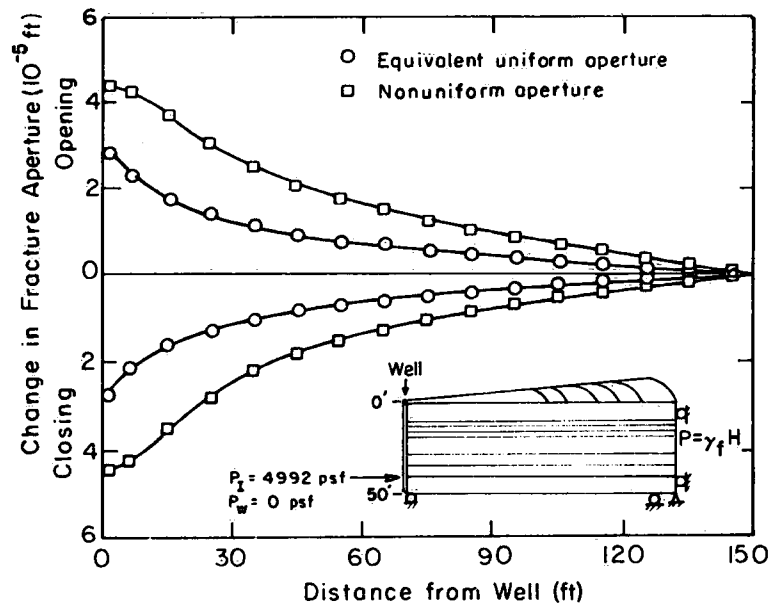


Figure 21. Fluid pressure profiles for injection and withdrawal in fractures with uniform and nonuniform apertures. (Fluid pressure changes in the well were $\pm 2,496$ psf.)

Figure 22. Fracture deformation owing to fluid injection and fluid withdrawal in uniform and nonuniform fracture apertures. (Fluid pressure changes in the well were $\pm 2,496$ psf.)



are much greater than those that occur in the case of an equivalent uniform aperture (equivalent in terms of flow rate for the same injection pressure and flow boundary conditions). For axisymmetric flow, with a theoretical logarithmic decrease in fluid pressure with radial distance, this difference in forces will be even greater.

To compare the effects of injection and withdrawal in a fracture having a non-uniform aperture with those in an equivalent fracture with a uniform aperture, the axisymmetric model described earlier in this section (Fig. 12) was used. It was assumed that the fracture located 40 ft below the surface was isolated for the purposes of this test so that no flow occurred in the other six fractures. The material properties for this model are also the same as those described earlier and a system where the fracture stiffnesses were $K_N = K_S = 4.72 \times 10^7$ psf/ft was investigated.

A nonuniform aperture was adopted by assigning a value of 0.001 ft for $0.125 \leq r_1 \leq 10$ ft and 0.0005 ft for $10 \leq r_2 \leq 150$ ft. For a rigid fracture with a total pressure drop of 2,496 psf, this nonuniform system had a flow rate of 2.126×10^{-3} cfs. Using this flow rate and equation (83) (in Chapter 3), an equivalent uniform aperture of 0.000648 ft was calculated.

Pressure profiles for the nonuniform and equivalent uniform apertures are shown in Figure 21 for both rigid and deformable fractures. The corresponding changes in aperture are plotted in Figure 22. The change in pressure that produced these deformations was only ± 40 ft of water at the well. As indicated in Figure 21, there is a considerable increase in the pressures that develop for injection into the fracture when it is nonuniform as compared with those that result with a uniform fracture. On withdrawal, the fluid pressures are decreased over a greater area within a nonuniform fracture than within a uniform fracture. This is reflected in the changes in aperture plotted in Figure 22. It is apparent that for both injection and withdrawal, the magnitude of the aperture change for the nonuniform case was approximately twice that of the uniform case.

The injection and withdrawal flow rates are tabulated in Table 3. It shows that for the nonuniform aperture, there is an increase of 14% and a decrease of 12% in flow rates for injection and withdrawal, respectively, compared with the flow rates of the rigid system. For the uniform aperture, the corresponding results are 10% and 8%.

The results above are for relatively small changes in pressure. In the past, injection tests have commonly been conducted at very high pressures. To demonstrate the effect a nonuniform aperture would have in such a case, the same model was again used with the same material properties but with injection pressures increased to 1 psi per foot of depth. This means a net pressure of 3,264 psf above the initial fluid pressure of

2,496 psf. The total pressure is slightly less than the overburden pressure because the rock weighs 165 lb/ft³.

Table 3. Flow Rates for Equivalent Uniform and Nonuniform Fracture Apertures ($\pm 2,496$ psf)

Fracture aperture type	Initial fracture aperture (ft)	Q Rigid fracture (10 ⁻³ cfs)		Q Deformable fracture (10 ⁻³ cfs)	
		Injection	Withdrawal	Injection	Withdrawal
Nonuniform aperture	0.001 ft ($0.125 \leq r_1 \leq 10$ ft)	2.126	-2.126	2.416	-1.868
	0.0005 ft ($10 \leq r_2 \leq 150$ ft)				
Equivalent uniform aperture	0.0006481 ft $0.125 \leq r \leq 150$ ft	2.126	-2.126	2.335	-1.949

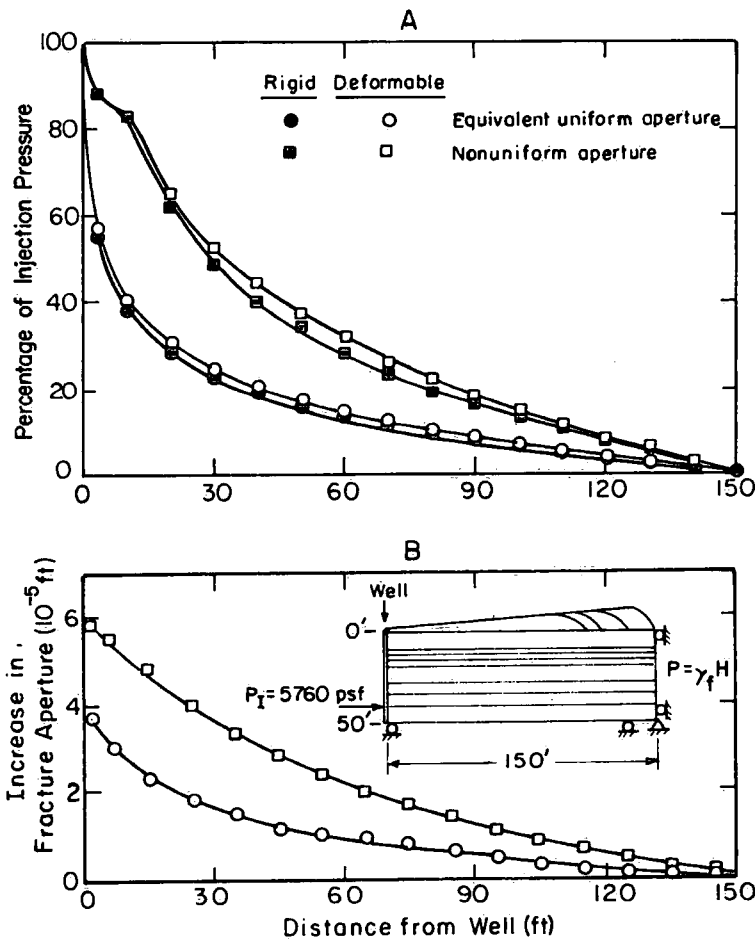


Figure 23. Fluid pressure profiles and changes in fracture apertures owing to fluid injection (+3,264 psf) in uniform and nonuniform fracture apertures.

The pressure profiles and the aperture changes are plotted in Figure 23. It is apparent that the magnitude of the fracture deformation near the well is considerably greater at these higher pressures. This is reflected in the flow rates tabulated in Table 4. These flow rates show an increase of 18% and 13% for the nonuniform and uniform fracture apertures, respectively, compared with those for the rigid case.

Table 4. Flow Rates for Fluid Injection in the Nonuniform and Equivalent Uniform Fracture Apertures (injection pressure, 3,264 psf)

Fracture aperture type	Q Rigid fracture (10^{-3} cfs)	Q Deformable fracture (10^{-3} cfs)
Nonuniform aperture	2.7803	3.2845
Equivalent uniform aperture	2.7803	3.1426

Although the stability of fractured rock masses will not be considered in this study, it can easily be seen that the pressure distribution calculated on the basis of a nonuniform fracture aperture is significantly different from that determined using an equivalent uniform aperture. This difference in pressure distribution, although not affecting flow rates significantly, can have a very important effect on the stability of the fractured rock mass.

Field Measurements of Fracture Deformation Due to Fluid Pressure Changes

INTRODUCTION

From 1970 to 1973, field investigations, sponsored by the Hydrology Research Division, Department of the Environment, were conducted to study fluid flow in the fractured crystalline and metamorphic rocks of Halifax County, Nova Scotia. Part of this effort was directed toward obtaining *in situ* measurements of changes in fracture aperture owing to changes in fluid pressure in the fracture plane. It was hoped that these measurements would assist in determining whether or not fracture deformation and the corresponding change in fracture permeability resulting from fluid pressure changes (produced by drawdown in a pumping well) would have a measurable effect on pump test results.

In the field work, as was in the case of the numerical model studies, investigations were restricted to rocks that had little or no intergranular permeability. Thus the groundwater movement in the rock mass takes place along the fractures or discontinuities. If the fractures close with an increase in effective stress (decrease in fluid pressure as the well drawdown increases), then the fracture permeability may depend on the available drawdown and the depth at which the major water-conducting fractures intersect the well bore. The permeability of rock-fracture systems exhibiting such characteristics is stress-dependent.

In this Chapter, a description is given of the field area selected for the fracture deformation measurements, the design and fabrication of instruments used, and the test procedures and test results.

STUDY AREA AND FRACTURE SYSTEM

Location and Description

The study area is approximately 20 mi southwest of the city of Halifax, Nova Scotia, in the southwestern part of Halifax County near the village of Sambro (Fig. 24).

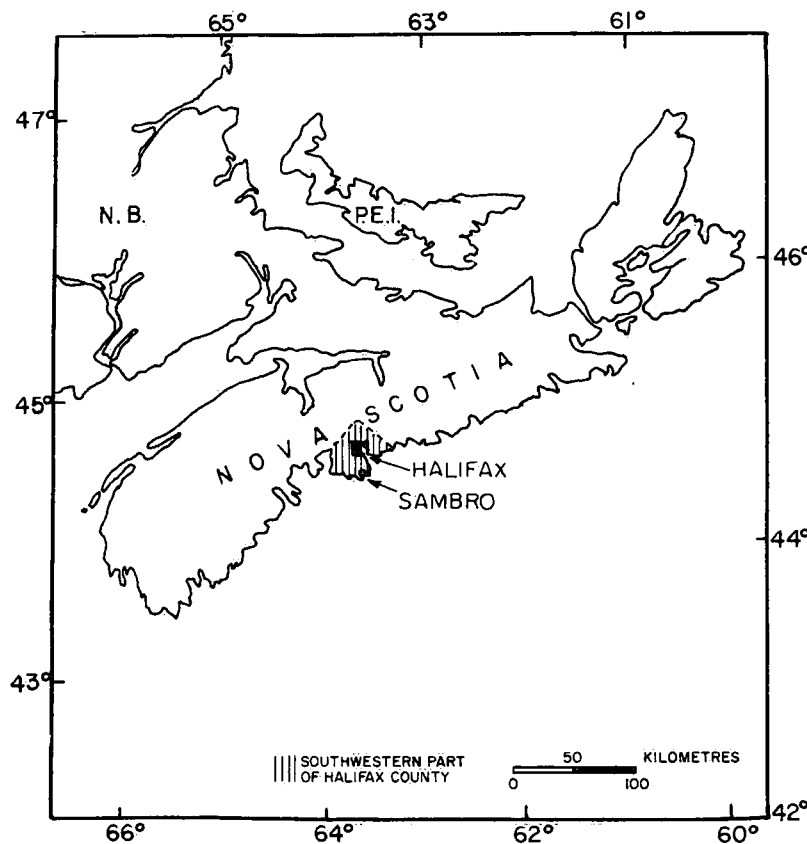


Figure 24. Study area.

This area was selected since it has a good combination of well-exposed bedrock, relatively simple fracture geometry and no interference from pumping of existing domestic wells. Access to the area is by paved road from Halifax to Sambro, and then by a one-half mile long truck trail to the test site.

The climate of Halifax County has been described by MacDougall, Cann and Hilchey (1963). They consider the climate to be humid temperate, with average winter and summer temperatures (based on data collected over the period from 1921 to 1951) of approximately 26°F and 63°F, respectively. For the same period the average yearly rainfall was 54.26 in.

The main topographic feature in southwestern Halifax County is an undulating plane which rises to an altitude of 600 ft in the northern part of the area and slopes gently to the seacoast. The area is dotted with small lakes and marsh-filled depressions.

Geology

Details of the geology of southwestern Halifax County have been given by Faribault (1907). Only a brief description is presented here.

The test area is well within the boundaries of a large granitic batholith of Early Devonian age (Smitheringale, 1960) that underlies a large part of central and southwestern Nova Scotia (Weeks, 1965).

In the Sambro area, the bedrock consists of a medium-grained porphyritic quartz monzonite with well-developed feldspar phenocrysts that frequently have a preferred orientation (Fig. 25). The bedrock is well exposed. The surficial deposits consist of glacial debris of varying thickness. The depressions are filled with peat and muck, indicating poor drainage. Glacial erratics, well-polished outcrops and striations are evidence of Pleistocene glaciation.



Figure 25. Bedrock exposure at Sambro test site showing preferred orientation of feldspar phenocrysts.

In the immediate area of the site, trenching revealed that the surficial material is less than 2 ft thick, with a coarse, sandy, residual layer at the base.

Surface Measurements

Figure 26 shows the general topography of the Sambro area and the fracture orientations at selected locations. Two sets of major structural lineaments (shear zones) were mapped from aerial photographs. These shear zones have a general strike of $N20^{\circ}W$ and $N45^{\circ}E$ and appear to be vertical.

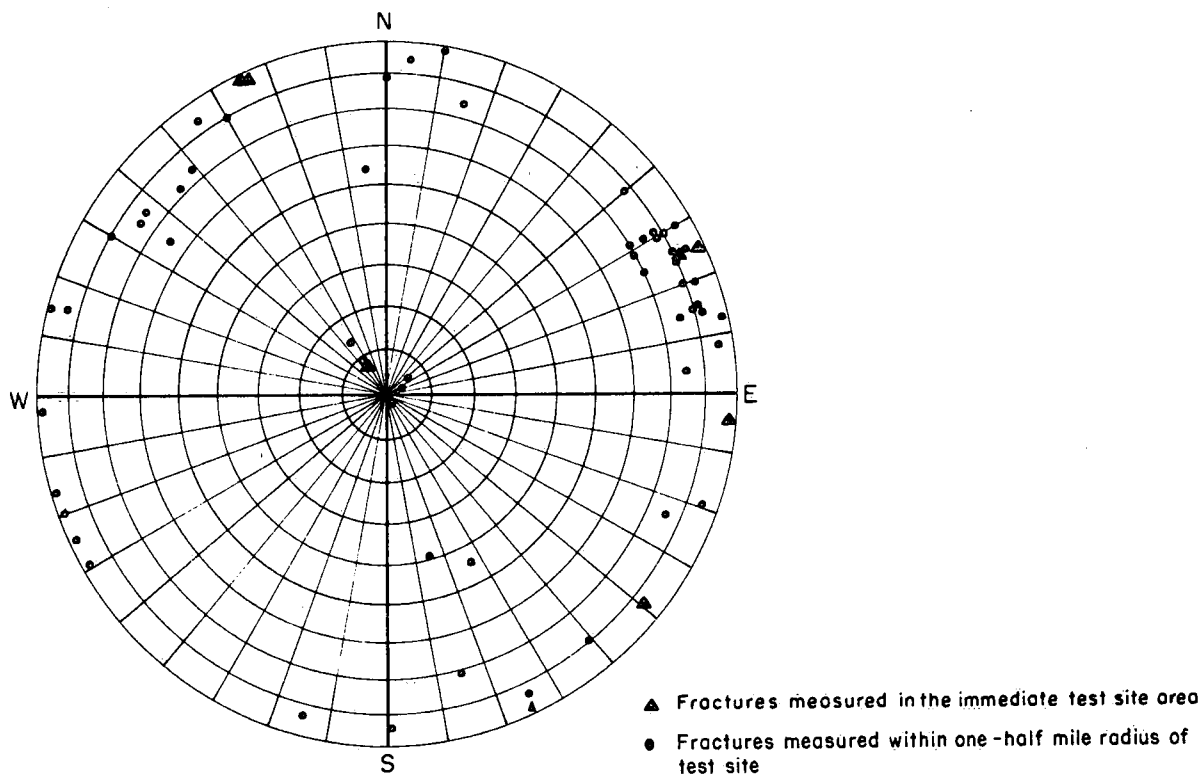


Figure 27. Upper hemisphere equal-area polar projection of poles to fracture planes measured in Sambro area.

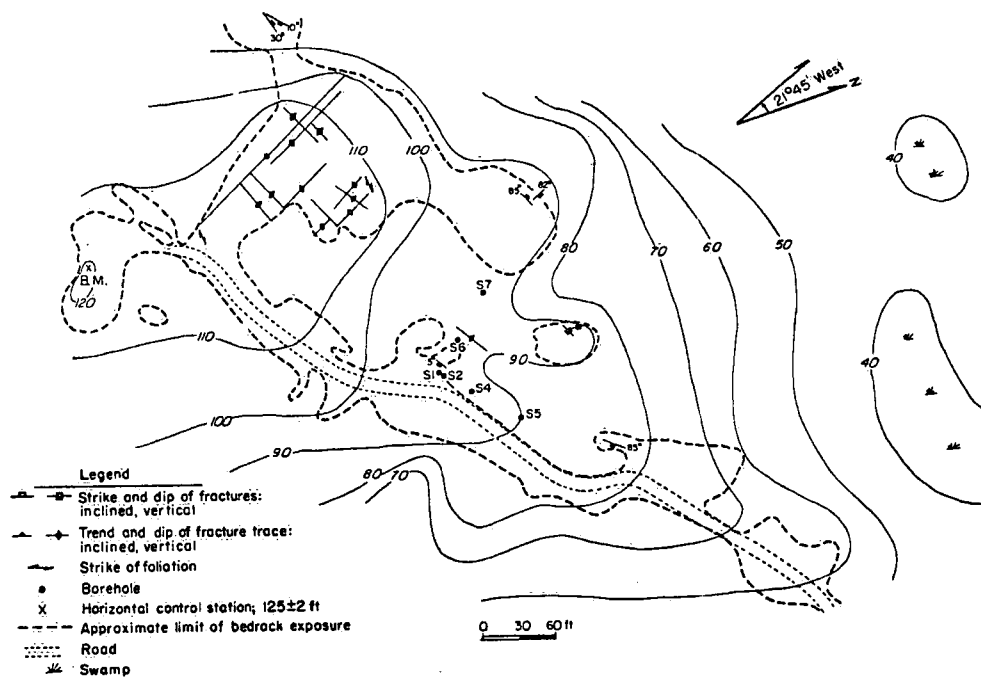


Figure 28. Plane-table map of Sambro test site.

site area could be measured and mapped. In the western part of the area, on a small hill, which corresponds to the highest elevations of the test site, vertical fracture traces were mapped (Fig. 28). As will be shown later, the horizontal fractures in this area and the evidence of glacial erosion suggest that this hill is a small exfoliated dome. In the central part of the area very few vertical fractures could be found, although this may be partly due to a decrease in the amount of bedrock exposure in this area. Trenching with a tractor failed to uncover any vertical fractures between the proposed drilling sites S1 and S6 (Fig. 28). Considered in conjunction with the natural bedrock exposure, this trenching gave an area of approximately 30 ft to 40 ft in radius on which no surface expression of vertical fractures could be detected. Since practically all of the fractures mapped at the test site have a near-vertical dip, fractures existing outside the 30-ft radius would be unlikely to intersect test wells at shallow depths located within this radius.

Thus the test wells are located in this central area. Two lines of wells were drilled. The first includes four wells: S1, S2, S4 and S5. The latter three are spaced at 3 ft, 35 ft and 70 ft, respectively, from S1 along the road in the direction $N45^{\circ}E$. A second line ($N45^{\circ}W$), at right angles to the first line and consisting of wells S6 and S7, was drilled at 35 ft and 70 ft, respectively, from S1 (Fig. 28).

Downhole Measurements

A total of six wells were drilled during the 1972 field season. Wells S1 and S2 are NX diamond drill holes (approximately 3 in. in diameter) 50 ft and 60 ft deep, respectively. Wells S4, S5, S6 and S7 were drilled using a percussion drill and are approximately 4 in. in diameter. These four wells are about 60 ft deep.

The objective of the drilling program was to determine the presence of horizontal to near-horizontal fractures and their lateral continuity between wells. Horizontal fractures were preferred for this experiment as they provide the simplest situation for placing instruments in the borehole. In addition, a horizontal fracture system was more amenable to numerical analysis, since a two-dimensional axisymmetric model could be used to simulate the field situation rather than a more complicated three-dimensional model.

Fracture occurrences in all six wells were determined from both analysis of the drill core (wells S1 and S2) and observation of the borehole walls using a borehole periscope (Trainer and Eddy, 1964). The fracture logs for wells S1 and S2 are given in Figures 29 and 30. Both the borehole periscope logs and the drill core analysis gave the same general fracture pattern in these two wells. In the percussion drilled wells, the drilling method left a relatively rough borehole wall, so that only the major fractures

could be detected with the borehole periscope. The smooth walls of a diamond drill borehole are an excellent background on which to detect even the faintest fracture trace. The fracture logs for wells S4, S5, S6 and S7 are given in Figure 31.

The fracture apertures in the periscope logs were estimated by comparing a marker of known width (0.005 ft) attached to the outside of the borehole periscope viewing area with the size of the observed fracture. Because of the nature of the fracture roughness and its irregular expression at the intersection with the borehole wall, the estimated apertures are a rough average of several estimates at different points on the borehole wall. An example of the detail obtained is shown in Figure 32 for the fracture at the 13-ft level in wells S1 and S2. The fine fractures may have resulted from the drilling. In the

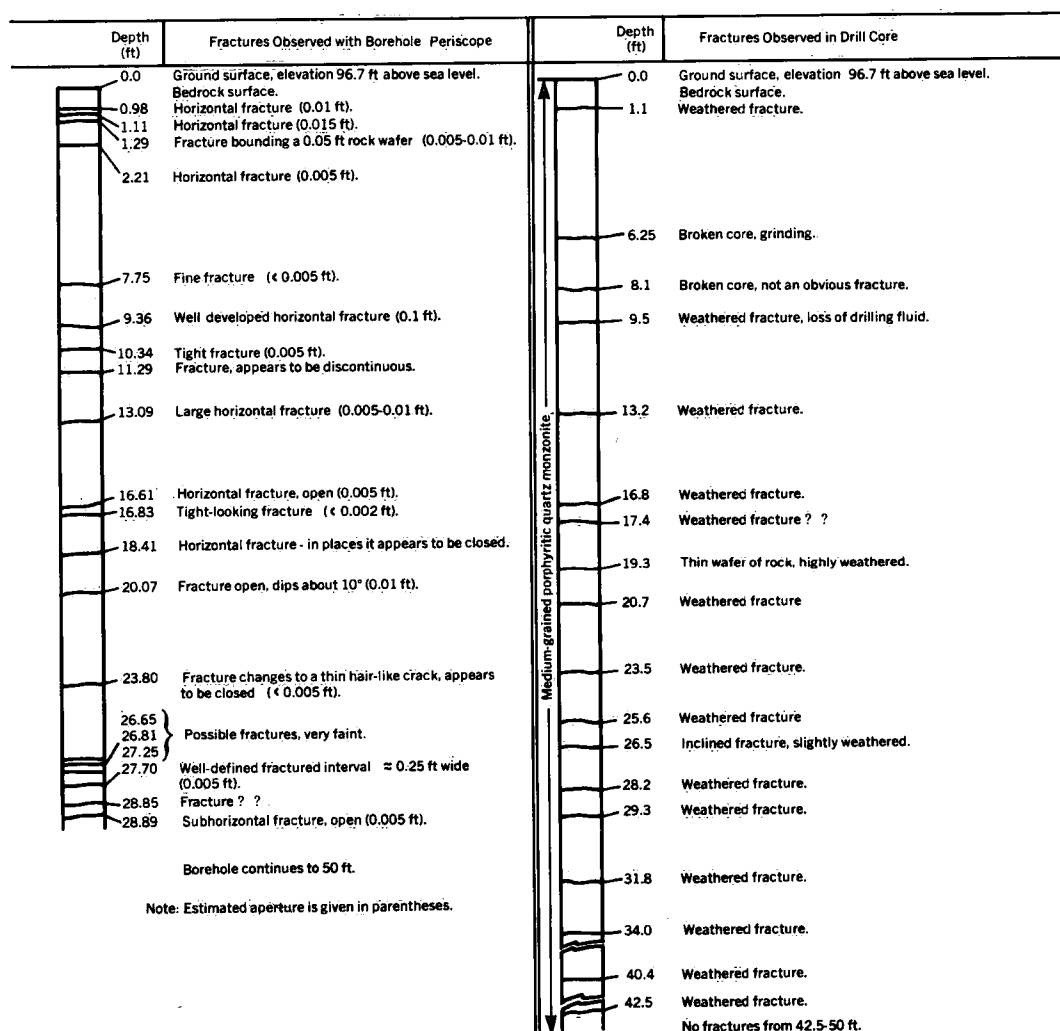


Figure 29. Fracture log for well S1.

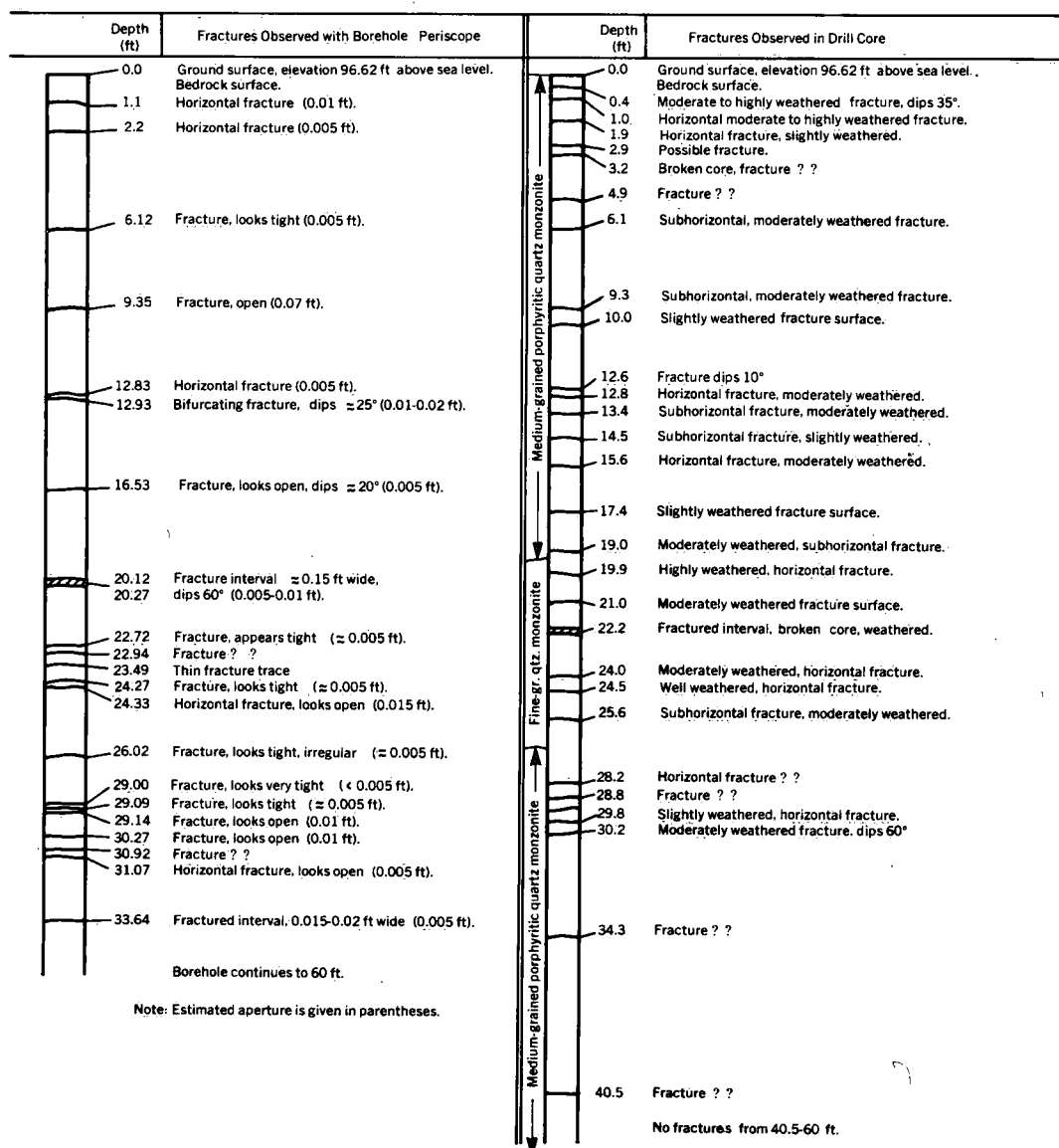


Figure 30. Fracture log for well S2.

following sections of this Chapter the estimated fracture apertures are compared with the equivalent uniform fracture apertures calculated from injection test results.

From the fracture logs it is apparent that most of the fractures are in the horizontal or near-horizontal plane. Most of the fractures are continuous between wells S1 and S2. The periscope logs (Figs. 29, 30 and 31) also indicate that nearly all of the major fractures are found in all of the wells except S7. Injection tests were performed to determine the relative hydraulic importance of the fractures observed.

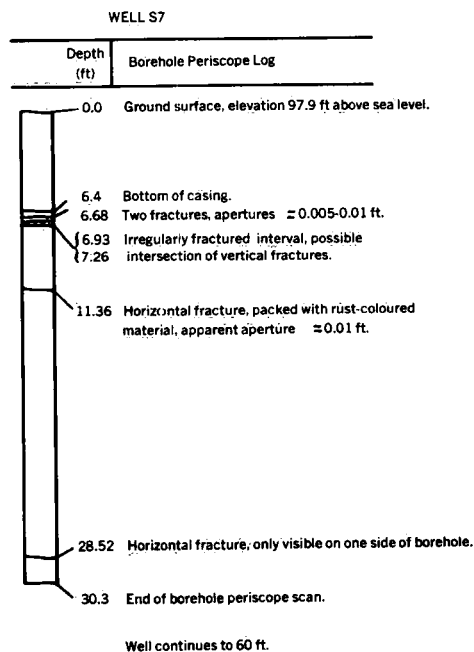
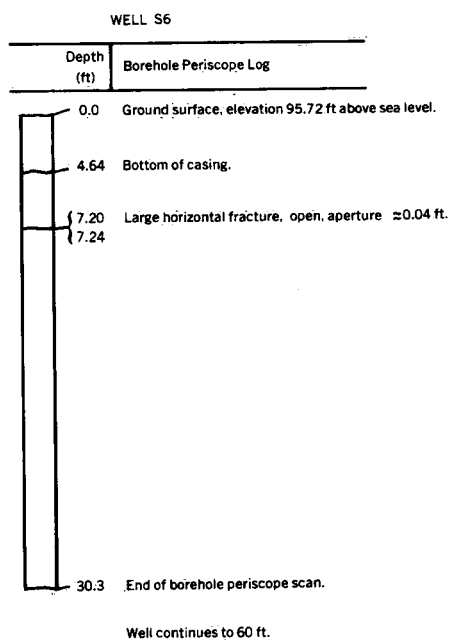
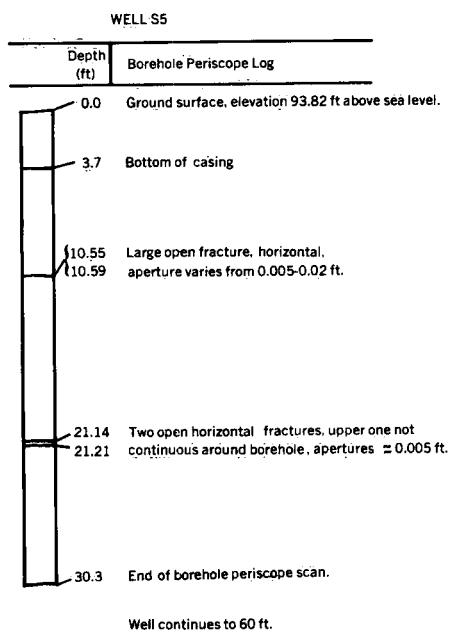
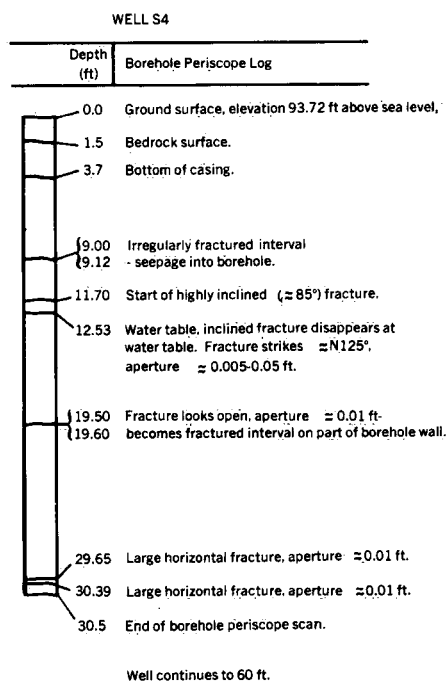


Figure 31. Fracture logs for wells S4, S5, S6 and S7.

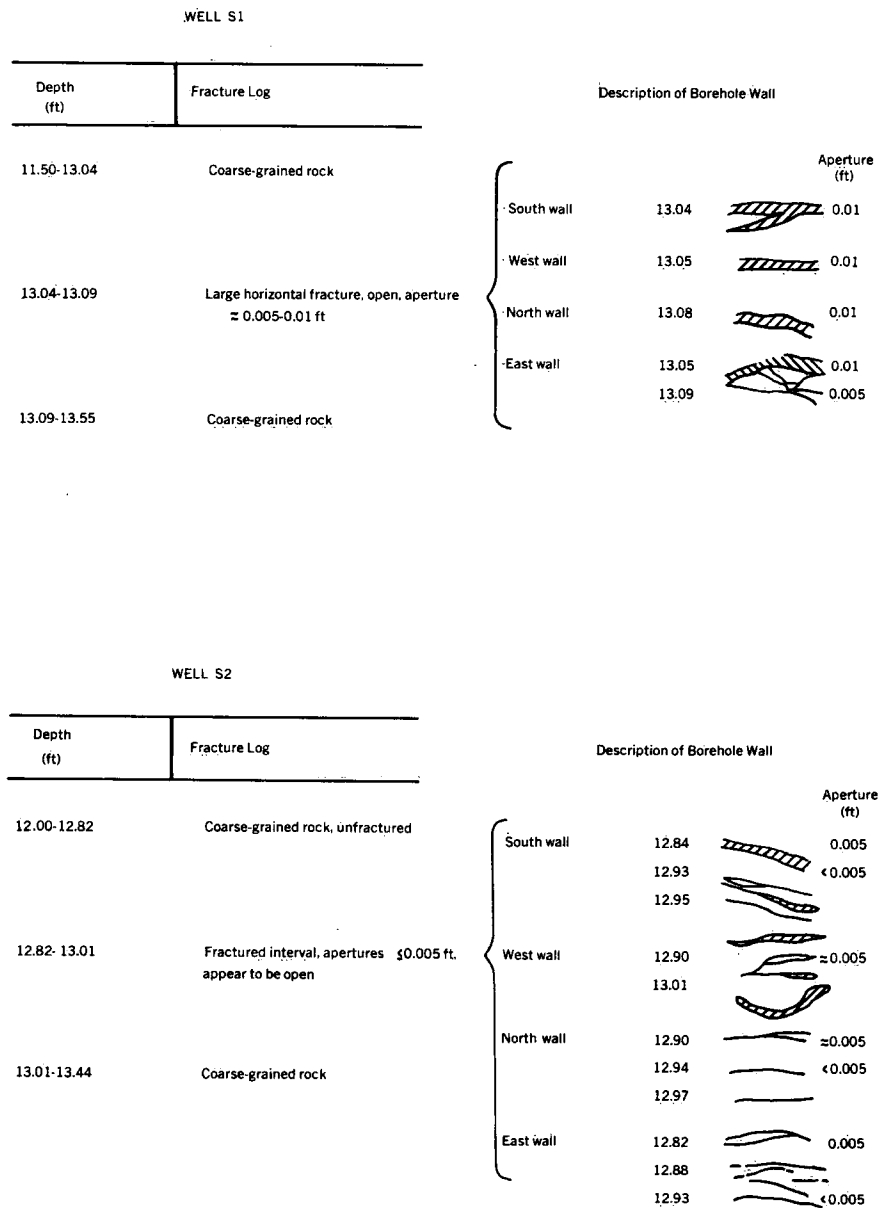


Figure 32. Detailed borehole periscope observations of fractures at 13-ft level in wells S1 and S2.

Material Properties

Uniaxial compression tests were performed on several specimens of NX diamond drill core obtained from wells S1 and S2. The test specimens were representative of the medium-grained porphyritic quartz monzonite bedrock at the test site. The test specimens consisted of a medium-grained (hypidiomorphic-granular) holocrystalline groundmass of biotite (12%), quartz (15%) monzonite containing several large (0.75 in. in length) feldspar phenocrysts. Other minerals present were potassium feldspar (25%), plagioclase (An_{50}) feldspar (45%), muscovite (2%) and approximately 1% accessory minerals. The potassium feldspar is altered in places to sericite.

A section of the fine-grained granitic vein material mapped in the core from well S2 (Fig. 30) was also tested. This vein material contains approximately 40% altered potassium feldspar, 25% plagioclase, 25% quartz, 7% muscovite and 3% secondary and accessory minerals. The rock is holocrystalline with a granular texture and can be classified as a fine-grained quartz monzonite.

The uniaxial tests were performed according to the ASTM (C170-50) "Standard Method of Test for Compressive Strength of Natural Building Stone." A load-displacement curve for the medium-grained quartz monzonite porphyry is shown in Figure 33 with pertinent test data. From the stress-strain data, a Young's modulus of 4.72×10^8 psf was calculated for this medium-grained rock. In addition, simultaneous measurements of lateral and longitudinal deformation at approximately 50% of the final load gave a Poisson's ratio of 0.28.

The load-displacement curve for the fine-grained quartz monzonite in Figure 34 gives approximately the same value of Young's modulus as that obtained from the medium-grained quartz monzonite porphyry cores, but the compressive strength of the fine-grained rock is much higher. Since the fine-grained rock was seen only as a few widely scattered veins in the outcrops at the test site and was otherwise found only in the core from well S2, no attempt is made to distinguish between the medium-grained and fine-grained rocks when constructing numerical models for this test site. In any event, the changes in stress during this experiment are only a small percentage of the compressive strength of the rock.

Examination of the drill core showed that some of the fracture surfaces exhibited chemical alteration to a depth of about 1 mm (0.003 ft) (Fig. 35). Undisturbed samples of the fractures were unobtainable for laboratory determination of the force-displacement relationships. For numerical modelling purposes, it is possible to attain an approximate measure of the fracture behaviour by using the laboratory data collected by other workers

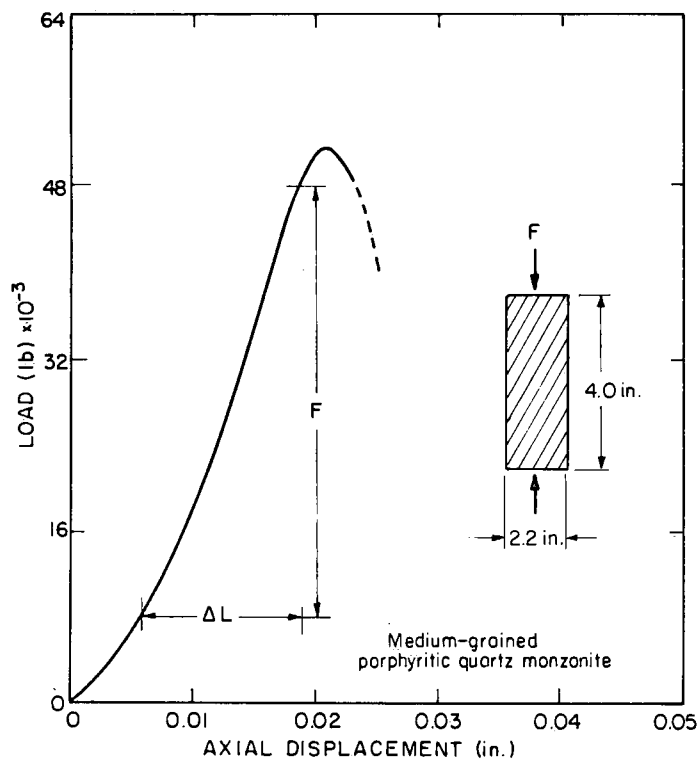
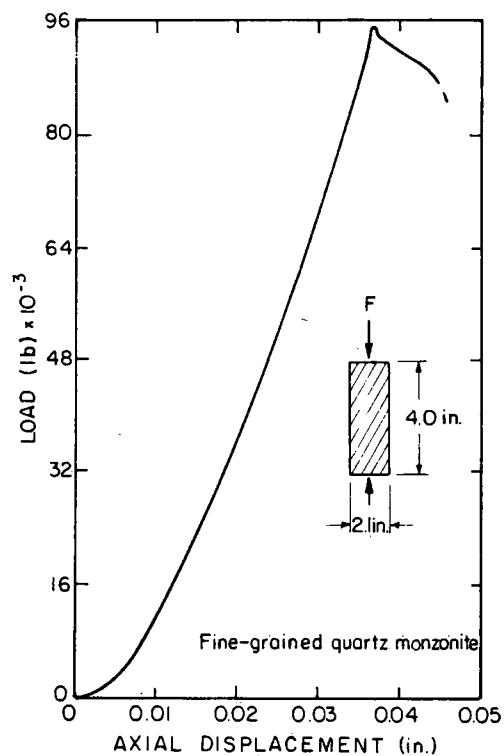


Figure 33. Load-displacement curve for a sample of the quartz monzonite porphyry.

Figure 34. Load-displacement curve for a sample of the fine-grained quartz monzonite.



for similar rock types. For example, Goodman and Dubois (1972) reported normal stiffness values for (1) an open clean joint in fresh quartz monzonite of 9.75×10^7 psf/ft and (2) an open calcified joint in slightly altered rhyolite porphyry of 1.04×10^8 psf/ft. Shehata, using artificially created tension fractures in quartz monzonite, measured a normal stiffness value of 1.35×10^7 psf/ft. All of the stiffness calculations above are based on the secant of the load displacement curve.



Figure 35. Close-up view of core from 9.36 ft below ground surface in well S1, showing the highly weathered nature of the fracture surface.

The highly deformable nature of the fractures at the test site was demonstrated by accidentally loading a water-filled fracture using a truck. The fracture was located approximately 2 ft below the surface and was connected to the surface by a 1-in. diameter drill hole. As the truck wheel approached the drill hole water was forced up the hole to the ground surface indicating that the fracture had closed.

Hydraulic Characteristics

Injection Tests

To evaluate the hydrologic characteristics of the fractures observed both in the boreholes and in the rock cores, constant-pressure injection tests were carried out using a standard injection test arrangement (Fig. 36) and the inflatable packer arrangements shown in Figure 37. Both single and double packer assemblies were constructed in the field and their construction closely followed that of Maini. The method of packer construction has been described by Gale and Welhan (1975b).

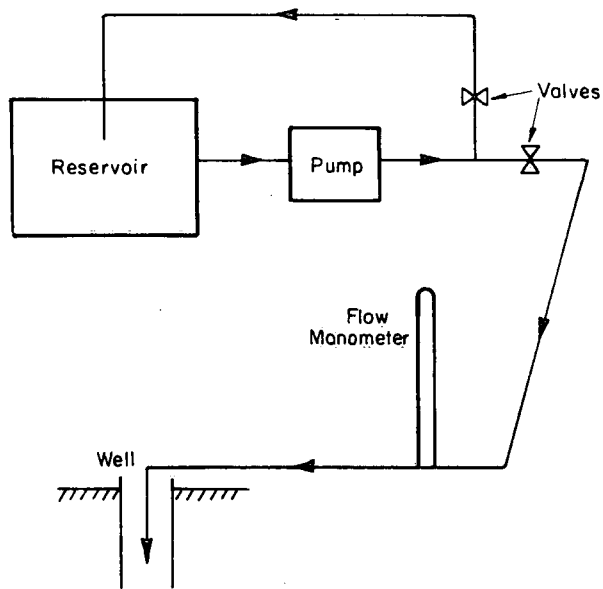
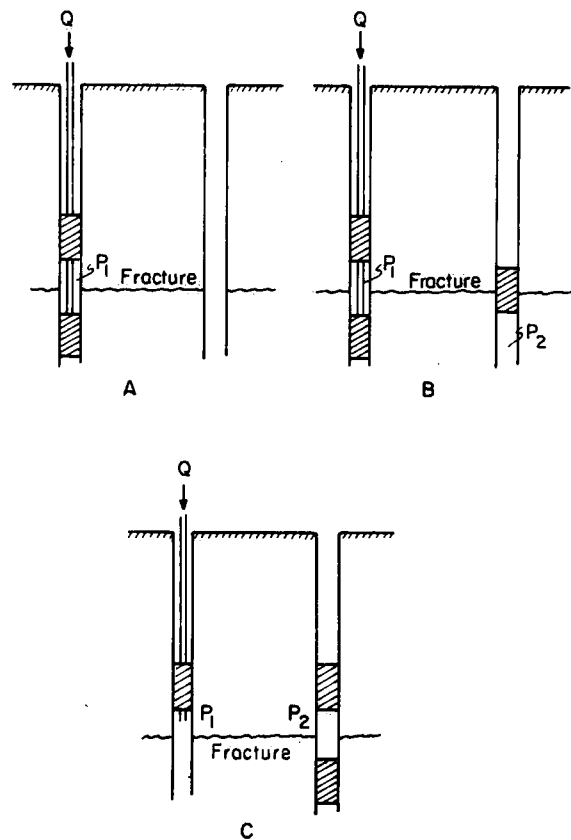


Figure 36. Schematic of injection test.

Figure 37. Packer arrangements for injection tests. P_1 is injection pressure; P_2 is pressure in the observation well.



The injection rates were measured using a series of three parallel flow manometers. The orifice plate openings in the manometer pipes were 1/8 in., 1/4 in. and 3/8 in., respectively. The calibration curves for the three flow manometers are given in Figure 38.

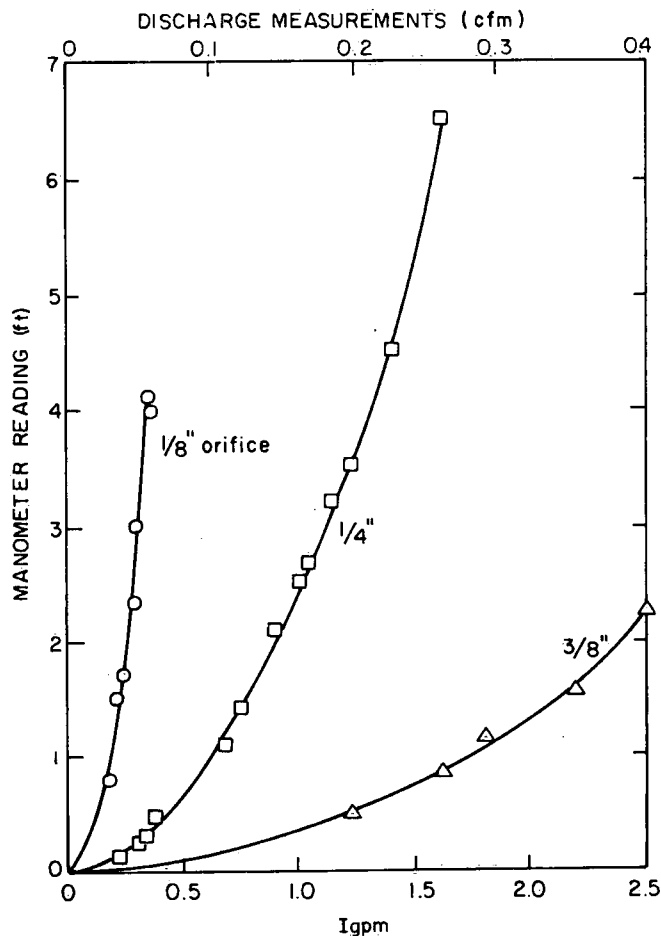


Figure 38. Calibration curves for flow manometers.

The injection rate was obtained by making spot measurements of manometer heights and then determining the corresponding flow rate from the manometer calibration curve. In many of the injection tests only the 1/4-in. orifice plate was used. From the calibration curves (Fig. 38) it can be seen that it was impossible to measure flow rates of less than 0.01 cu. ft/min with this manometer system. To determine very low flow rates, the volume removed from the temporary reservoir (45 Imperial gallon capacity) was measured over a 20- to 30-min period.

During each injection test, the flow rate was increased until the desired water pressure in the injection cavity was reached, and then the water pressure was held constant by adjusting the flow rate. A continuous record of the fluid pressure in the injection

cavity was made using Hewlett-Packard single-pen strip-chart recorders and the fluid pressure transducer equipment shown in Figure 39. In each injection test, the packer separation was approximately 2 ft and the fluid pressures were increased successively until the pressure in the packer interval was slightly less than overburden pressure. Pressures were held approximately constant after each pressure change until the flow rate had stabilized.

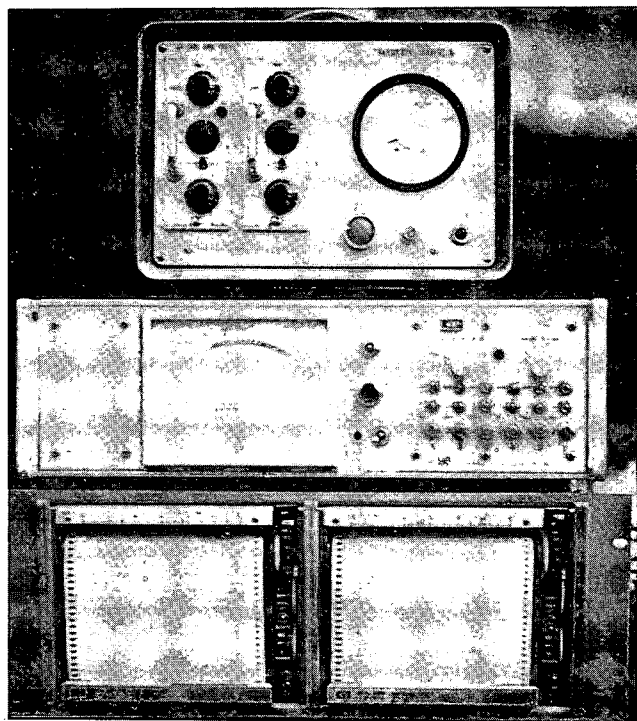


Figure 39. Pressure transducer equipment.

Most of the experimental work was performed in wells S1 and S2. Since these two wells are only 3 ft apart, the injection tests were (a) carried out with the second well open (Fig. 37, section A) and (b) repeated with the fracture being tested blocked with an inflatable packer where it intersected the second well (Fig. 37, section B).

Table 5 summarizes the results of the injection tests in well S1 with (a) well S2 open and (b) the fracture being tested in S1 blocked in well S2. By comparing these pressure and flow rate data with the fracture logs in Figures 29 and 30, it can be seen that the most important water conduits in S1 are located at 9.36 ft, 13.19 ft, 20.04 ft, 27.7 ft, 28.89 ft and ~40 ft below the ground surface. Thus there is very good agreement between the location of the fractures detected by the injection tests and the location of the fractures described as being open in the periscope logs or as being weathered in the core logs (Fig. 29).

Table 5 also shows that the open well (S2) has a greater effect on the flow rate in the larger fractures (at 13.19 ft and 20.04 ft) than on the flow rate in the smaller fractures (at 27.7 ft and 28.89 ft). Thus for the larger fractures, the appropriate flow

rates must be determined while the fracture being tested is blocked in well S2. The difference in the flow rates above can be partly explained if the fractures at 13.19 ft and 20.04 ft have large apertures in the vicinity of wells S1 and S2 and these apertures decrease farther from the wells. It should be noted that the injection test results show that the fracture at approximately 40 ft below the ground surface is essentially a discontinuous fracture that is penetrated by both wells S1 and S2. This fracture accepts a fairly large flow rate when S2 is open, but the flow rate is essentially zero when the fracture is blocked where it intersects well S2.

Table 5. Pressure and Flow Rate Data and Calculated Equivalent Uniform Apertures for Injection Tests in Well S1

Depth interval open in S1 (ft)	Pressure increment (psi)	Flow rate (cfm)	Equivalent fracture aperture (ft)	
			S2 Open	S2 Blocked
8.55-10.5	(2*) 0.2	0.2675	0.0037	
	(5) 0.7	1.0755	0.0039	
10.15-12.10	10.1	≤0.0268†	≤0.00046	
11.85-13.8	(4) 3.0	0.2135	0.00138	
	(6) 4.1	0.2530	0.00132	
	(10) 5.5	0.2640	0.00121	
12.55-14.5	(7) 3.0	0.2198	0.0014	
	(9) 4.8	0.3000	0.00132	
12.45-14.4	(3) 5.4	0.0589		0.00074
	(11) 7.5	0.0689		0.00069
14.10-16.05	30.0	≈ 0.0+		
15.60-17.55	22.3	0.0016†	0.000139	
	32.5	0.0268	0.000313	
17.35-19.30	19.2	≈ 0.0+		
19.25-21.2	(5) 6.5	0.2279	0.00109	
	(12) 8.6	0.2658	0.00104	
	(18) 10.8	0.2615	0.00096	
19.2-21.15	(6) 2.5	0.0401		0.00084
	(12) 5.7	0.0776		0.0008
	(28) 10.8	0.0936		0.0007

*Time in minutes since test started.

†No detectable flow rate.

‡Flow rate averaged over 20- to 30-min period.

Table 5. Continued

Depth interval open in S1 (ft)	Pressure increment (psi)	Flow rate (cfm)	Equivalent fracture aperture (ft)	
			S2 Open	S2 Blocked
20.65-22.60	22.0	≈ 0.0+		
22.55-24.5	22.4	≈ 0.0+		
23.45-25.4	15.0	≈ 0.0+		
25.15-27.1	12.6	≈ 0.001†	0.000143	
25.75-27.7	8.7	0.001	0.000162	
26.75-23.7	(2) 6.3	0.0385	0.00061	
	(5) 9.9	0.0593	0.00061	
	(8) 16.2	0.0931	0.00060	
27.55-29.5	(5) 8.5	0.0722	0.00068	
	(10) 16.3	0.1124	0.00064	
	(18) 18.6	0.0995	0.00058	
	(20) 19.0	0.0979	0.00058	
27.4-29.35	(11) 8.6	0.0776		0.00069
	(25) 18.1	0.1124		0.00061
	(4) 25.8	0.1338		0.00058
29.3-50.0	(2) 1.1	0.0669	0.0013	
	(8) 7.4	0.1043	0.00081	
	(15) 10.9	0.1124	0.00073	
	(19) 14.9	0.1525	0.00072	
30.65-32.60	26.7	0.0+		
32.60-34.55	4.4	0.00018†	0.00011	
	10.3	0.0003†	0.0001	
33.85-35.8	21.2	0.0+		
39.25-41.20	(1) 1.6	0.0401	0.00098	
	(6) 3.9	0.0722	0.00088	
	(10) 6.0	0.0963	0.00084	
	(17) 11.5	0.1378	0.00076	
	(22) 16.5	0.1578	0.00071	
39.2-41.15	10.0	0.001†		0.00015
40.55-42.50	19.3	≈ 0.0+		
41.55-43.50	12.3	≈ 0.0+		
41.5-50.0	17.4	≈ 0.0		

By observing the fluid pressure below a single packer blocking the fracture in S2 while fluid is being injected between two packers straddling the fracture in S1, it is evident whether the fracture being tested is hydraulically connected to any of the fractures below it. The fluid pressures for three different tests of this type on fractures located at 13.19 ft, 20.04 ft and 28.89 ft below ground surface in well S1 are shown in Figure 40. The fluid pressures below the inflatable packer in well S2 did not change as the individual fractures in S1 were being tested. Thus it can be assumed that at least in the immediate vicinity of wells S1 and S2, vertical fractures, if present, are not significant fluid conductors. Note that this set of figures presents total pressures in the well, not the increase in fluid pressure.

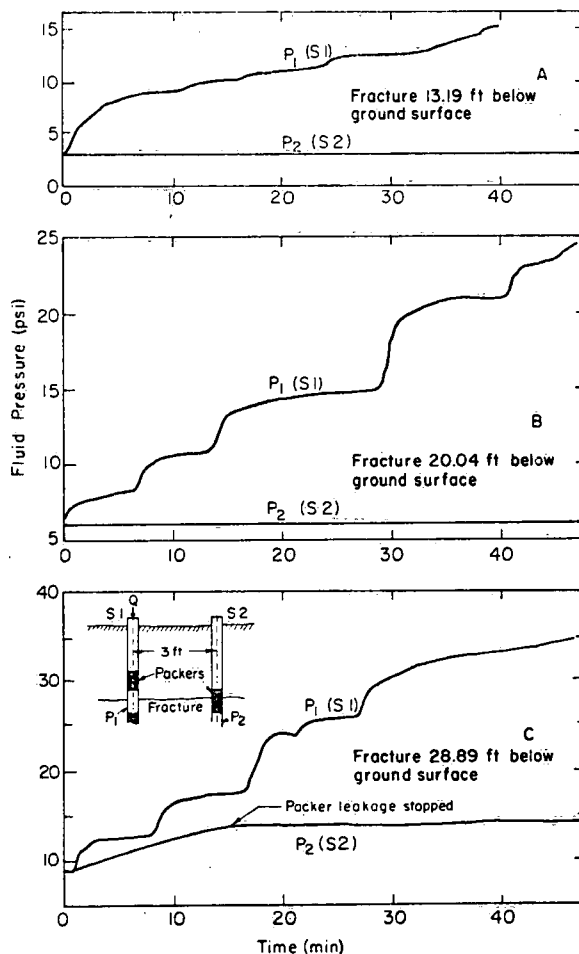


Figure 40. Fluid pressures in various fracture planes. P_1 is pressure at injection well; P_2 is pressure below fracture plane at a radial distance of 3 ft.

The borehole periscope logs for wells S4, S5, S6 and S7 (Fig. 31) show that most of the significant fractures detected in wells S1 and S2 have similar counterparts in wells S4 and S5. In wells S6 and S7, only a few fractures were detected with the borehole periscope, partly because of the rough nature of the borehole walls. The flow rate data

from wells S4 and S6 do not indicate an increase in fracturing below the 30-ft level over that observed in wells S1 and S2. This is shown by the injection rates in Table 6. Well S7 would not accept any water even when lithostatic pressures were approached, suggesting that this well does not intersect the fracture system detected in the other wells. It is also possible that the intersecting fractures were plugged by the drilling operations (air-driven percussion drill).

The different hydraulic character of well S7 is further demonstrated by the fluid temperature profiles measured in wells S1, S5 and S7 (Fig. 41). From the shape of the temperature profiles the conclusion can be drawn that wells S1 and S5 are part of the same fracture flow system but that well S7 is not. This, in part, substantiates the injection test results and the borehole periscope logs. These temperature measurements were made with a thermistor and Wheatstone bridge.

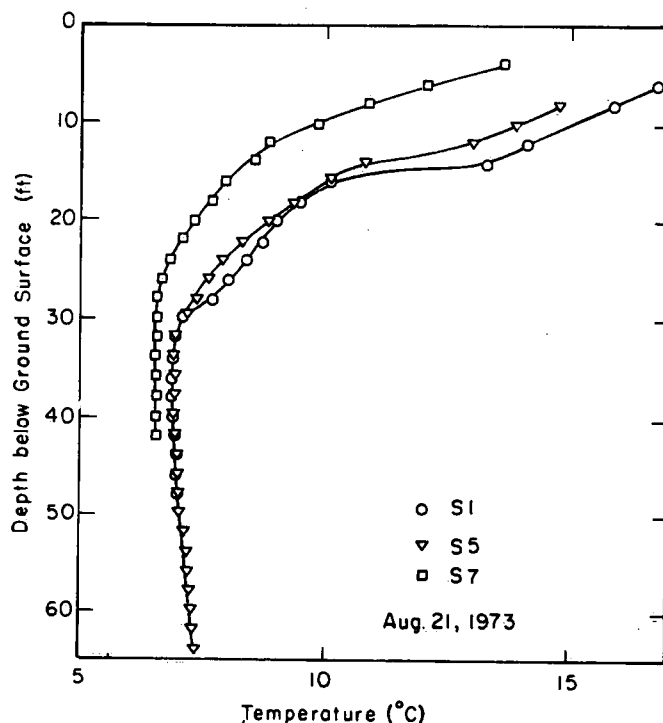


Figure 41. Fluid temperature profiles measured at beginning of field season before the wells had been disturbed.

Calculated Equivalent Fracture Apertures

The fracture system described above can be idealized as a system of horizontal fractures, and these fractures can be modelled using the parallel plate analogy. Individual equivalent uniform fracture apertures can be calculated using a radial flow, parallel plate model with the radius of influence determined from field observations.

Table 6. Pressure and Flow Rate Data from Wells S4, S6 and S7

Well S4			Well S6			Well S7		
Injection interval (ft)	Increase in pressure (psi)	Flow rate (cfm)	Injection interval (ft)	Increase in pressure (psi)	Flow rate (cfm)	Injection interval (ft)	Increase in pressure (psi)	Flow rate (cfm)
31.0-46.0	(8*) 9.3	0.0918	31.0-46.0	(8) 8.5	0.1307	15.5-60.0	13.5	0.0
	(12) 9.9	0.0704		(12) 9.2	0.6088			
	(2) 10.2			(16) 9.2	0.0959			
				(20) 9.4	0.0787			
46.0-60.0	(8) 6.3	0.0508	46.0-60.0	(10) 8.7	0.2194			
	(12) 7.0	0.0428		(12) 8.8	0.1979			
	(20) 8.5	0.0347		(16) 8.7	0.1926			
	(23) 8.7	0.0334		(19) 8.5	0.1950			
	(30) 8.8	0.0321						

*Time in minutes since test started.

Applying Darcy's law to a horizontal parallel plate model for radial flow

$$V = -k \frac{dH}{dr} \quad (79)$$

where H is the hydraulic head,

V is the velocity,

r is the radial distance from the well, and

k is the hydraulic conductivity of the fracture $\left(\frac{\rho_f g (2b)^2}{12\mu} \right)$.

The flow from a cavity into a fracture (Fig. 42) is

$$Q = 2\pi r (2b) V \quad (80)$$

where Q is the flow rate.

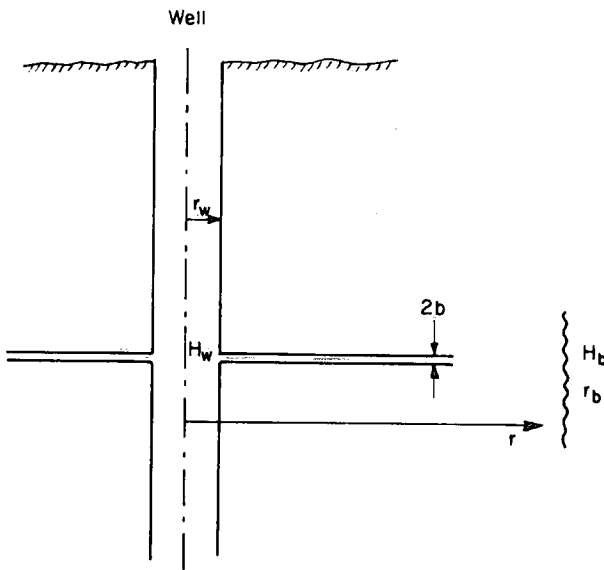


Figure 42. Flow from cavity to fracture.

Combining equations (79) and (80)

$$Q = -2\pi r (2b) k \frac{dH}{dr} \quad (81)$$

After rearranging, equation (81) becomes

$$\int_{r_w}^{r_b} \frac{dr}{r} = - \int_{H_w}^{H_b} \frac{k}{Q} 2\pi (2b) dH \quad (82)$$

where H_w is the hydraulic head in the borehole (L),

H_b is the hydraulic head on the boundary (L),

r_w is the borehole radius (L), and

r_b is the radial distance to flow boundary (L).

Integrating equation (82) leads to an expression for an equivalent uniform fracture aperture, based on measured flow rates and hydraulic heads at the borehole and assumed boundary conditions

$$2b = \sqrt[3]{\left[- \left(\frac{12 Q \mu}{2 \rho_f g \pi} \right) (\ln r_b - \ln r_w) \right] / (H_b - H_w)} \quad (83)$$

Application of equation (83) is generally based either on the assumption of an aquifer of infinite radius or on the measurement of hydraulic head values in the plane of the fracture in a second borehole. Muskat (1946) has shown that the assumption of an infinite aquifer for porous media leads to a maximum possible error in the permeability calculation of not more than an order of magnitude. For the fracture system at the test site, it can be assumed that $50 \text{ ft} \leq r_b \leq 500 \text{ ft}$.

To demonstrate the relative unimportance of the radius of influence in determining the size of the calculated fracture apertures, consider the case of a constant flow rate and a constant pressure in a 3-in. diameter borehole intersecting a single horizontal fracture. The effect of different values of r_b (the distance to a constant-head boundary) on the magnitude of the equivalent uniform fracture aperture calculated using equation (83) can now be determined. For example, a constant flow rate of 0.003 cfs and a constant injection head of 50 ft, for r_b equal to 50 ft, 250 ft and 500 ft, will give equivalent uniform fracture apertures (2b) of 0.000638 ft, 0.00069 ft and 0.00071 ft, respectively. Thus for the purpose of calculating equivalent uniform fracture apertures, one can safely assume a radius of influence of 150 ft based on the local topography and hydrogeology of the site.

The equivalent uniform apertures calculated from the injection test results are given in Table 5. These fracture aperture calculations are based on the assumption of laminar flow, a constant water temperature of 20°C and a radius of influence of 150 ft. Also, it has been assumed that only one fracture is present in each injection interval and that the presence of the open well at a radius of 3 ft can be disregarded. The error involved in making this last assumption can be assessed by considering the data for the case where the second well is blocked.

From the injection test results in Table 5 it is evident that the fracture system at Sambro can be represented, with some degree of idealization, by a system of seven discrete fractures as shown in Table 7. This idealized system will be used in constructing a numerical model of the Sambro test site discussed in Chapter 4. Table 7 includes the fracture apertures determined from the borehole periscope observations and the equivalent uniform fracture apertures determined from the injection tests. It will be noted that the calculated fracture apertures are much smaller than the estimated fracture apertures. These differences are covered in the following section.

Distribution of Fluid Pressures in the Fracture Plane

As discussed in Chapter 2, the magnitude of the fracture deformation depends on the distribution of fluid pressures in the fracture plane. Therefore a variation of the standard injection test (Fig. 37, section C) was used to determine the fluid pressure distribution in the plane of the fracture. Water was injected in well S1 using a single packer. A double packer was used to isolate a fracture in well S2 which also intersected the injection cavity in well S1. The fluid pressure was recorded in both wells simultaneously.

To be able to compare the fluid pressure distribution measured in the different fractures tested, the fluid pressure profile owing to flow in a single horizontal fracture, as depicted in Figure 43, was calculated. The pressure profile shows the change in fluid pressure expressed as a percentage of the change in fluid pressure at the injection or withdrawal well plotted against a dimensionless distance which includes the radius of the well and the radial distance to the constant head boundary. This calculated pressure profile is based on the radial flow formula (Verruijt, 1970, p.36), a rigid uniform fracture aperture, a constant head boundary at r_b and known flow rate and fluid pressure boundary conditions. This curve is independent of the flow rate, injection and fluid boundary pressures, magnitude of the fracture aperture, well radius and distance to the constant head boundary. Therefore it can be used to compare field, laboratory or numerical results. Note that the flow rates and fluid pressures at the boundaries determine the size of the calculated fracture aperture. Having obtained a compatible uniform fracture aperture, the radial flow formula can then be used to calculate the fluid pressure profile.

Table 7. Fracture Data and Equivalent Fracture Apertures for Selected Fractures at Sambro

Fracture depth		Aperture estimated from borehole periscope log (ft)	Excess hydraulic head (ft)	Flow rate (10 ⁻³ cfs)	Calculated equivalent apertures (ft)
Model (ft)	Borehole (ft)				
10.0	9.36	0.1-0.08	0.46	4.46	0.0037
13.0	13.19	0.01-0.02	12.47	0.98	0.0007
			17.32	1.12	0.00069
16.5	16.61	0.005	51.5	0.027	0.00014
			75.1	0.45	0.00031
20.0	20.07	0.005-0.01	5.8	0.67	0.00084
			13.2	1.29	0.0008
			24.9	1.56	0.00068
28.0	28.89	0.005-0.01	19.86	1.29	0.00069
			41.8	1.87	0.00061
33.5	34.0	0.005	10.16	0.003	0.00011
			23.79	0.005	0.0001
40.0	41.0		23.3	≤0.001	0.00015

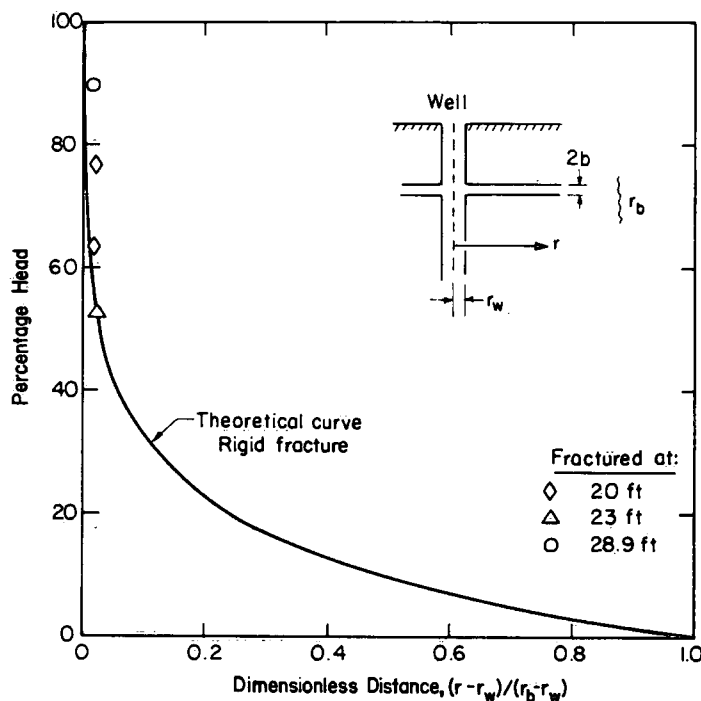


Figure 43. Percentage change in hydraulic head for laminar axisymmetric flow from borehole.

Verruijt (1970, pp. 37-38) has discussed the degenerative nature of the radial flow formula for both the case of a well of infinitely small radius and the case where the outer radius of the well becomes infinitely large. He concluded that these limitations have no practical significance, since neither of the cases above exist in nature. Thus, as expressed, the radial flow formula implies a finite radius well in a finite aquifer.

Deviation from the theoretical curve plotted in Figure 43 can result from (a) nonuniform fracture apertures, (b) fracture deformation, (c) turbulent flow, (d) anisotropy in the fracture plane plus other contributing factors which might include head loss where the fracture intersects the well.

The numerical results presented in Chapter 2 show that flow in fractures with nonuniform apertures produces a fluid pressure profile considerably different from flow in fractures with equivalent uniform apertures. During fluid injection the fluid pressures at some point away from the injection well will be a greater percentage of the injection pressure if the apertures are not uniform than if the apertures are uniform. Thus the point representing the fluid pressure in a nearby observation well will plot above the curve shown in Figure 43. This observation is based on the assumption that the injection well intersects the fracture at the point where the fracture aperture is largest. If the injection well should intersect the fracture where the aperture is smallest and the observation well intersect the fracture at a point where the fracture aperture is larger, then the fluid pressure at the observation well would plot below the curve shown in Figure 43.

The numerical results presented in Chapter 2 also indicate that if the fracture deforms (opens) owing to an increase in fluid pressure, then the fluid pressures are propagated a greater distance from the injection well. In fact, it is the same effect as in a fracture with a nonuniform aperture except that the nonuniformity of the fracture aperture in this case is due to the magnitude of the fracture deformation decreasing with a decrease in fluid pressure away from the injection well. In a fracture with a fairly uniform aperture the percentage of the fluid pressure, with respect to the injection pressure, measured at a given point would increase with increasing pressure and the corresponding increase in fracture deformation. Thus for each increase in pressure, a given point on the fluid pressure profile would plot farther and farther above the curve in Figure 43.

Turbulent flow would produce a greater pressure drop per unit radial distance than laminar flow and thus the fluid pressure profile would decrease more rapidly than shown in Figure 43. On the basis of injection pressures and flow rates given in Table 5, it can safely be assumed that turbulent flow was not an important factor in the tests performed during this field experiment.

To determine the effects of anisotropy within the fracture plane on the fluid pressure profiles, simultaneous measurements from different observation wells would be needed. Because of the lack of such wells, the importance of anisotropy could not be determined in this particular field situation. On account of the enlargement of the fracture aperture at the well bore by the drilling operations, head losses in the well bore are not considered to be significant.

Section A of Figure 44 shows the pressure-time history for a fracture located 28.9 ft below the ground surface. Note that fluid pressures are expressed as total water pressure measured at the injection cavity and the observation well and not as the pressure increase. If the increase in pressure P_2 measured in S2 is expressed as a percentage of the increase in pressure P_1 measured in S1, for each pressure level, the field measurements can be compared with the fluid pressures that are predicted from the calculated pressure profile. For this fracture under approximately steady-state conditions, the field measurements show that the fluid pressure in the observation well (P_2) 3 ft from the injection well is approximately 90% of the pressure measured in the injection well (P_1) for all the pressure steps shown.

The measured fluid pressure in the observation well determines one point on the fluid pressure profile of this fracture. If this point is plotted on Figure 43, it is located a considerable distance above the theoretical curve.

One possible explanation of this discrepancy is that natural fractures do not usually have uniform fracture apertures. From field observations of fracture systems, it

is concluded that nonuniform fracture apertures are the rule rather than the exception. Thus, as shown in Chapter 2 (Fig. 20), if a well intersects a fracture at some point where the fracture aperture is large and if at some distance from the well the aperture decreases, a fluid pressure distribution similar to that indicated in Figure 44, section A, would be observed during injection tests.

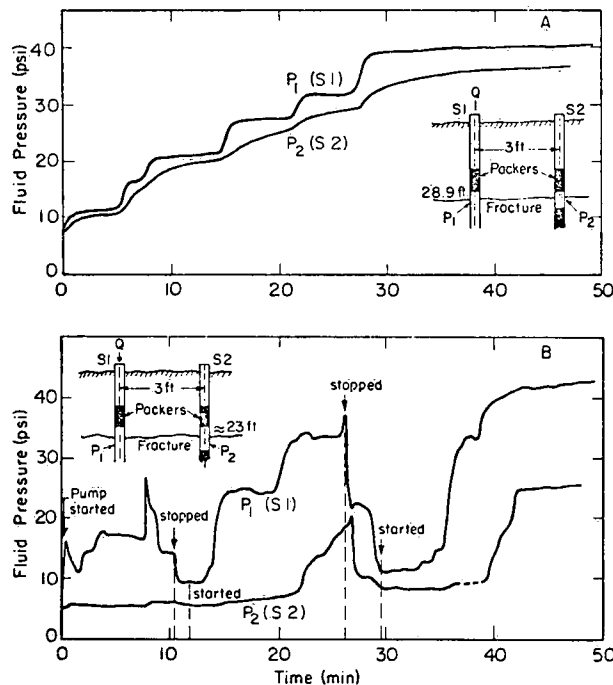


Figure 44. Distribution of fluid pressures in the fracture plane:
A - fracture at the 29-ft level
and
B - fracture at the 23-ft level.

Also, it should be noted that the calculated fluid pressure profile assumes radial symmetry. This may not be a valid assumption for the field situation, although deviations from this assumption would not be expected to have a significant effect on the fluid pressures within the first several feet of the well bore.

The effect that a nonuniform fracture aperture has on fluid pressure distribution and fracture deformation, and hence on flow rate, has been discussed for an idealized fracture system in Chapter 2.

The results of an injection test in a very fine fracture located 23 ft below the ground surface are presented in section B of Figure 44. The ratios of pressures measured at P_1 and P_2 for this test are significantly different from those shown in section A. The flow rate in this fracture was so small that it could not be accurately measured. Because of equipment problems, only the last 20 min of this test is usable. If the stabilized changes in fluid pressures at the end of the test are compared, taking into account initial fluid pressures of 8 psi and 6 psi for wells S1 and S2, respectively, P_2 is approximately

53% of P_1 . This point plots directly on the curve in Figure 43. Since the fluid pressures in the injection well exceed the lithostatic pressure, it must be assumed that fracture deformation does play some role in determining the fluid pressure distribution observed. Because of the poor quality of this particular test result, no speculation on that role or on the variability of the fracture aperture itself is possible.

In another injection test, on the open fracture at 20 ft below the ground surface, two steady-state pressure levels were used. The increases in fluid pressures were 12.5 psi and 8 psi for P_1 and P_2 , respectively, for the first pressure level, and 22 psi and 17 psi for P_1 and P_2 , respectively, for the second pressure level. Thus the fluid pressure at the observation well corresponds to 64% and 77% of the fluid pressure at the injection well for the first and second pressure levels, respectively. These two points plot one above the other in Figure 43 and may represent changing fluid pressure distributions owing to fracture deformation. This particular test is discussed later in connection with the presentation of the field measurements of fracture deformation.

From the field measurements above of fluid pressure distributions in the fracture planes it is concluded that the results presented in Table 7 and based on equivalent uniform fracture apertures are not a good representation of the actual field situation. The information about the fluid pressures observed 3 ft from the injection well can now be used to refine the fracture aperture calculations. This is accomplished by applying equation (83) to each fracture in two successive steps, using two different sets of boundary conditions.

In the first step, the fracture aperture between the injection well and the observation well ($r_b = 3$ ft) is calculated. The increases in pressure measured at the injection well (P_1) and at the observation well (P_2) are used as the pressure boundary conditions. This enables the calculation of an equivalent uniform fracture aperture for that part of the fracture between the injection well and the observation well.

In the second step, it is assumed that the radius of the well (r_w) is equal to the distance to the observation well and that r_b equals 150 ft. The fluid pressure at r_w is set equal to the increase in fluid pressure measured at the observation well. Thus, by applying equation (83) a second time, the calculation of an equivalent uniform fracture aperture for that part of the fracture plane between 3 ft and 150 ft is possible.

The results of the calculations above are presented in Table 8 for the five fractures described in Table 7 for which there are simultaneous measurements in both the injection well and the observation well. For the two fractures on which the necessary pressure distribution data are not available, Table 8 uses the calculated equivalent uniform fracture results given in Table 7.

In Table 8 it is evident that some of the fractures seem to be highly nonuniform. Additional observation wells would permit a much better description of the actual variation in fracture aperture. The results presented in Table 8 are used in most of the numerical simulations of the Sambro test site that are presented in Chapter 4.

Table 8. Nonuniform Fracture Apertures Calculated from Injection Test Results

Fracture depth (ft)	$\frac{P_2}{P_1} \times 100$ (%)	Nonuniform apertures (ft)		Equivalent uniform apertures (ft)
		($0.125 \leq r \leq 3$ ft)	($3.0 \leq r \leq 150.0$ ft)	
9.5	98	0.01008	0.003037	0.0037
13.0	95	0.001537	0.000616	0.0007
16.5		(0.005*)		0.00014
20.0	64	0.00085	0.0008	0.00084
28.89	90	0.00114	0.000549	0.00069
33.5		(0.0005*)		0.00011
≈ 40	98	0.000170	0.00005	0.00015

*Estimated with borehole periscope; no data on pressure distribution.

There is still a considerable difference between the fracture apertures reported in Table 8 and those presented in the borehole periscope logs (Figs. 29 and 30). Attempts to determine the size of fracture apertures using a borehole periscope are complicated by the enlargement or chipping of the fracture at the borehole walls as a result of the vibrations of the drilling bit. In addition, there is no way of estimating the effect of roughness within the fracture plane. An increase in roughness decreases the effective fracture aperture. If roughness was taken into account in calculating equivalent fracture apertures, the cubic relationship in equation (83) would have to be modified, resulting in larger apertures being calculated than those now reported.

Thus, because of roughness, chipping of the fracture edges during drilling and nonuniform flow within the fracture plane, the effective fracture opening is considerably less than direct observations would suggest. Direct visual observation of fractures gives, at best, a rough qualitative estimate of the relative hydraulic importance of the different fractures.

Constant Flow Rate Injection Test

Although no vertical fractures could be detected by the hydraulic tests or observed in the outcrops near the test wells, the fracture system at the test site must be connected to vertical fractures at some point. The vertical and near-surface horizontal

fractures may or may not be completely saturated. Because of the small size of the fracture apertures the capillary effect would be expected to ensure that the fractures were, in fact, saturated.

The injection tests discussed previously in this Chapter were based on maintaining a constant pressure in the injection cavity. Figure 45 shows the pressure versus time record for a constant flow rate into the injection cavity. The injection cavity consisted of all the fractures located below the 19-ft level in well S1. Well S2 was blocked with an inflatable packer at the 19-ft level.

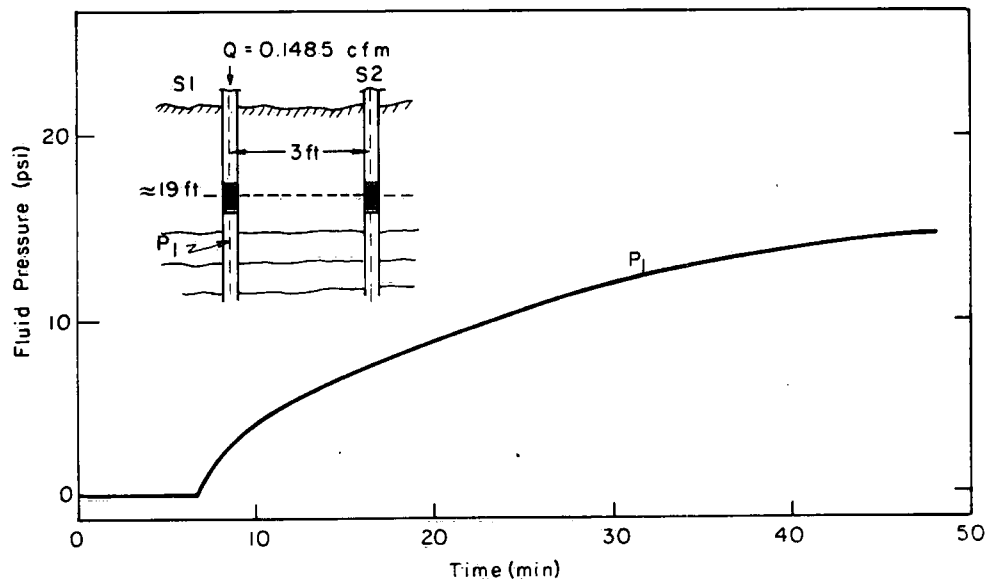


Figure 45. Pressure-time data for constant flow rate injection test.

The results of the pressure variation during a constant injection rate test should give some indication of the nature of the boundary conditions, such as the presence or absence of a no-flow boundary. In the presence of a no-flow boundary, the fluid pressures would be expected to increase continually and after some period of time to increase more rapidly. Also, Maini (personal communication, 1972) has suggested that a constant flow rate test could be used to detect the presence of unsaturated fractures. If part of the fracture system was unsaturated, the field pressures would be expected to increase continually in the injection cavity.

The results of the constant flow rate test at the test site (Fig. 45) show that the rate of fluid pressure increase slowly decreases with time. The test had to be stopped after approximately 45 min. Although it cannot be concluded that the fracture system is completely saturated, the rate of change of fluid pressure in the injection cavity does

not suggest that a significant percentage of the fractures are unsaturated. Also, the pattern of change in fluid pressures in the injection cavity does not suggest the presence of no-flow boundary conditions at this test site. Finally, the effect fracture deformation had on the observed fluid pressure changes during this test is unknown. Undoubtedly, fracture deformation contributed to some of the transient effects observed.

Withdrawal Tests

Several attempts were made to determine the hydrologic response of the entire fracture system by a withdrawal test. The decrease in water levels was measured both in the pumped well and in the nearby observation well. When the pumping rate was about 1 gpm very rapid drawdowns were measured after only 30 min or 40 min of pumping. By slowly decreasing the pumping rate it was determined that the wells would only sustain a very small pumping rate. Thus, after the fluid pressures in the fracture system had stabilized, the pumping rate was set at $1.43 \times 10^{-3} \text{ ft}^3/\text{s}$ and held constant during the pumping test by using a discharge control tank (Gale and Welhan, 1975a).

Section A of Figure 46 is a log-log plot of time in minutes versus drawdown in feet for a pumping test in well S2. The pump jet was set at approximately 55 ft below the ground surface. The fluid pressures were measured using a pressure transducer located approximately 4 ft below the pump jet. Water levels in well S1 were measured with a tape. The pump test was continued for approximately 400 min and was terminated when the water level in well S2 reached the pump jet.

The data presented in Section A of Figure 46 are not amenable to standard pump test analysis. During the first 250 min of the test the maximum drawdown is approximately 1 ft, and then the drawdown begins to increase rapidly (Fig. 46, section A). There are two obvious factors that contribute to this sort of well response. Recalling the descriptions of the fractures observed in wells S1 and S2 (Figs. 29 and 30), it can be seen that a large fracture (fracture aperture $\approx 0.1 \text{ ft}$) intersects both wells at approximately 9 ft below the ground surface. This large fracture must act as a reservoir, resulting in the very small drawdowns during the earlier part of the pump tests. When it had been dewatered, the rate of drawdown increased rapidly.

It should be noted that when the water level falls below the large fracture at the 9-ft level, the discharge from this fracture is independent of the drawdown in the pumping well. Thus it is extremely important to know the points along the well bore at which the main water-conducting fractures intersect the borehole.

The recovery of the well was very rapid (Fig. 46, section B), with almost complete recovery being reached in approximately 120 min. The effect fracture deformations had on the response of this well could not be determined from these data.

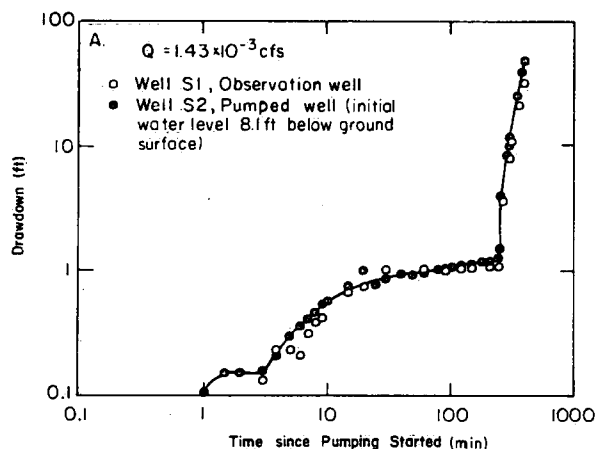
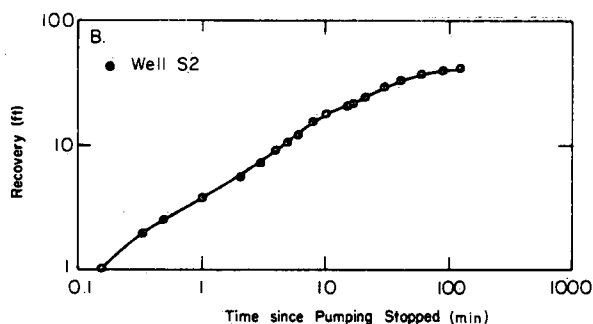


Figure 46. Pump test data.



APERTURE DEFORMATION RESULTING FROM FLUID PRESSURE CHANGES

As stated earlier, in the field study emphasis was placed on measuring the opening and closing of fractures in response to changes of fluid pressure within the fracture plane. It was anticipated that these measurements of fracture deformation would provide an indication of the extent to which stress-dependent permeability affected well behaviour in fractured rock aquifers.

At the start of the field program, the rock and soil mechanics literature on instrumentation was reviewed. This revealed that the *in situ* measurements of changes in fracture apertures could not be made with existing instruments. Thus it was necessary to design and develop a special instrument that could be placed in a borehole and used to measure changes in fracture openings of as little as 10^{-6} ft. The author, in conjunction with the Instrumentation Section of the Inland Waters Branch, Department of Fisheries and the Environment, designed and developed an instrument which is referred to as a "fracture deformation gauge." Details on the development and use of this instrument have been

presented by Gale and Welhan (1975a). In the following text, changes in fracture aperture that were measured during withdrawal and injection tests using the fracture deformation gauge are discussed.

Withdrawal Test

A pumping-out test lasting approximately 10 min was carried out at the test site. The fracture deformation gauge was locked in place across a fracture at the 29-ft level in well S1. A pump jet was installed in well S2 at the 50-ft level. The well was pumped at a constant rate of 2.4 gpm and fluid pressures were measured at the deformation gauge in S1 and slightly above the pump jet in well S2. The high pumping rate was to ensure a rapid drawdown, since the field equipment did not permit testing for a long period of time.

A constant discharge tank previously described by Gale and Welhan (1975a) was used to control the flow rate during the test. A leak in the pump jet during the initial so-called "cycling" period (Gale and Welhan, 1975a) caused the fluid pressures to decline in both wells during this part of the pumping test. During this period, all water removed from the well should be returned to it, but during the actual field experiment some of the water being removed from the well replaced air in the water pipes connecting the pump and control tank.

The inset in Figure 47 shows the test configuration. The fluid pressures in both the observation well (P_2) and the pumping well (P_1) were recorded as well as the output from the measuring device [a linear variable differential transducer (LVDT)] inside the fracture deformation gauge. The output was converted to displacement in feet and is indicated on the same time scale as the fluid pressures (Fig. 47).

When the pump was started, the fluid pressures in both wells declined very rapidly and there was an abrupt closing of the fracture. It continued to close until the fluid pressure in well S1 fell below the level of the fracture deformation gauge, i.e., until P_2 reached a constant value. After the water level in S1 had dropped below the deformation gauge, there was an abrupt change in the rate of fracture closure. The continued closure of the fracture reflects that the fluid pressures were still changing in the surrounding rock mass. After the pump was stopped the water level in S2 started to recover. There was no change in the rate of fracture closure until the fluid pressure started to increase in the plane of the fracture, at which time the fracture started to reopen.

The water levels in both wells were allowed to recover for approximately 43 min. At that time neither the fluid pressures nor the fracture apertures had returned to their original values and the ratios of fracture deformation to fluid pressures were different from those observed at the beginning of the test. Part of this residual fracture closure

was due to the incompletely recovered water levels in the wells, but part may also have been due to the changing fluid pressures in the rock mass, i.e., may have been a transient effect such as that observed on the strain records at Bergen Park, Colorado, reported by Snow (1968a). In addition, some of the fracture closure may be irreversible, representing nonelastic deformation of the asperities and filling materials in the fracture owing to increased effective normal stress.

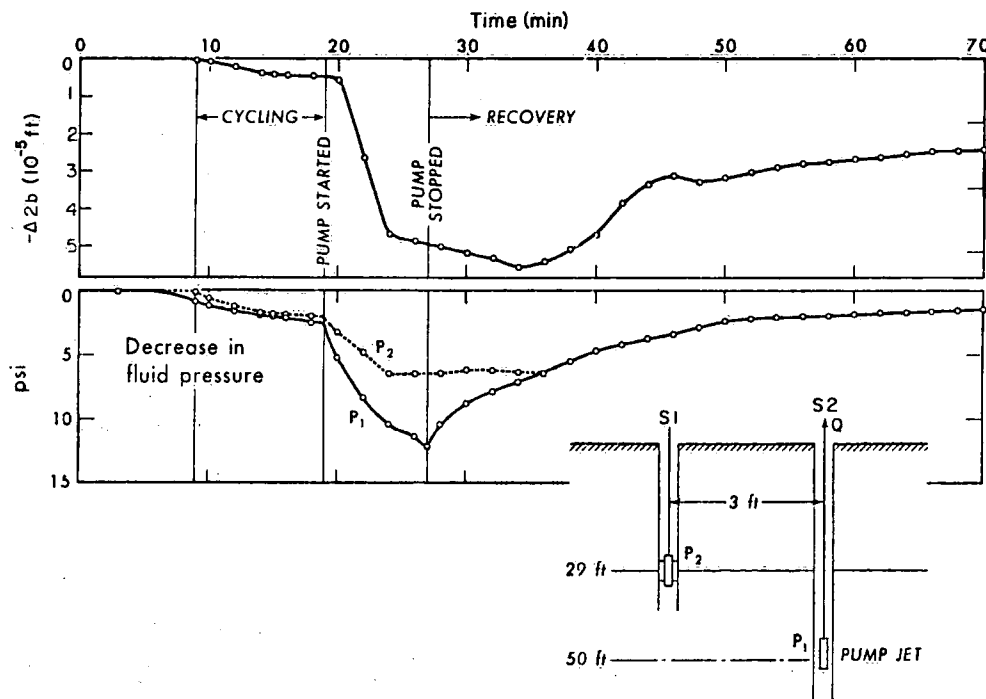


Figure 47. Results of fracture deformation measurements during withdrawal test. Fracture deformation gauge locked across fracture at 29-ft level. Water level at start of test was ≈ 9 ft below ground surface.

The fracture surfaces, as observed in the drill cores, were weathered by the effects of groundwater movement over a long period of time. Thus on the drill core the character of the rock varies from very weak, weathered material on the fracture surface to dense unweathered rock at a depth of about a millimetre. By reducing the fluid pressures in the fracture plane the effective normal stress increased and thus the weaker asperities may have been crushed. In a well with a depth of 200 ft to 300 ft with a possible change in fluid pressure of approximately one-half the well depth, the resulting nonrecoverable deformation would be represented by a significant permanent change in the fracture permeability.

The total fracture deformation measured during this test was approximately 5×10^{-5} ft. The fracture deformation can be compared with the equivalent fracture aperture

of 6×10^{-4} ft calculated from injection test results. The measured deformation is approximately one-twelfth the computed aperture.

In view of the very small pressure changes observed in the fracture plane (-7.5 psi), this is a significant change in fracture aperture. One would assume that with an increase in aperture there would be a decrease in the contact area of the opposing fracture surfaces. With a decrease in contact area, a small change in fluid pressure in the fracture plane would result in an increase in deformation, since the stresses at the points of contact would be higher.

As mentioned earlier, calculated equivalent apertures are not a very good measure of local fracture openings. In Table 8, it has been shown that for the fracture at the 29-ft level, the aperture is of the order of 10^{-3} ft within a 3-ft radius around the well. Therefore the measured changes in aperture are a smaller proportion of the original fracture opening. Thus the changes in aperture for this larger fracture opening are more consistent with the magnitude of the changes in fluid pressures observed.

Injection Tests

Several tests were conducted where the well containing the fracture deformation gauge was used either as the injection or the observation well. When water was being injected into the well containing the fracture deformation gauge, the pressures changed in all fractures that intersected the well bore below the packer seal. In this case, a double packer was used in the observation well to isolate the fracture across which the deformation gauge had been placed in the injection well. Thus the change in pressure 3 ft from the injection well in the plane of the fracture being tested was known.

When the well containing the deformation gauge was used as the observation well the procedure above was reversed. Using a double packer assembly a single fracture in the injection well was isolated. The deformation gauge was placed across this same fracture in the observation well. This well was sealed with a single packer above the deformation gauge. It should be noted that water being injected into the fracture in the injection well could flow into the observation well. This would raise the fluid pressure in other fractures intersecting the observation well below the packer seal.

Figure 48 shows the results of injecting water into the well containing the deformation gauge. The gauge was locked in place across the fracture at the 29-ft level (28.89 ft below ground level). This is the same fracture across which measurements were made during the pumping-out test (Fig. 47). In Figure 48, the flow rate is plotted in cubic feet per second, the fluid pressure in both wells (see inset) in pounds per square inch and the change in fracture aperture in feet against time in minutes since the test

started. The basic data used to compile this Figure are given in Tables 9 and 10. The fluid pressures (P_2) in the observation well (S2) are almost equal to the fluid pressures (P_1) measured in the injection cavity (S1). It should be noted that the pressure measurements were only accurate to ± 1 psi, at best. The sudden jump in injection cavity fluid pressure (P_1) after approximately 20 min may be partly due to fluctuations in electronic signals, since P_1 does not return to its original value at the end of the test. The sudden increase in P_1 may also have been caused by flushing of drilling material from the fracture plane during the injection test. In any event, the fluid pressure distribution in Figure 48 is very similar to that observed during an earlier injection test in the same fracture (Fig. 44, section A), i.e., P_2 is greater than 90% of the pressure (P_1) at the injection point.

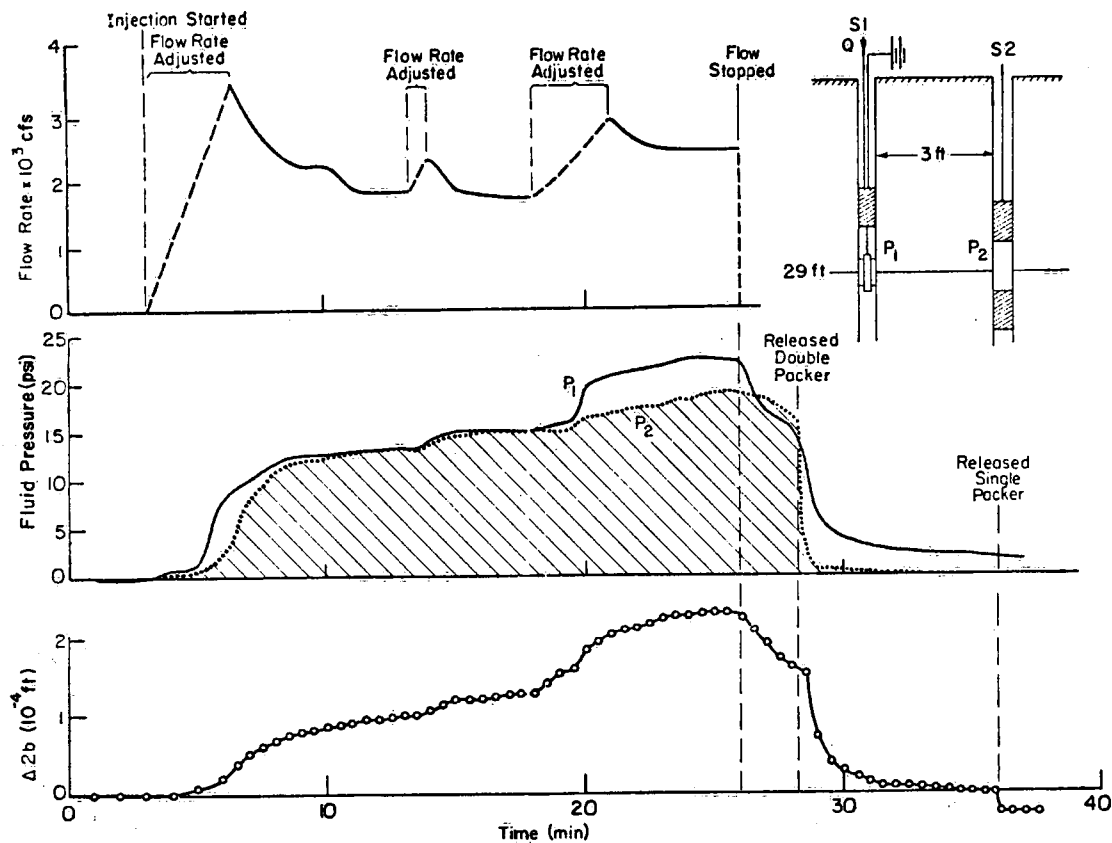


Figure 48. Results from an injection test in well S1 with the fracture deformation gauge locked across the fracture at the 29-ft level in S1. Water level at start of test was ≈ 11 ft below ground surface.

It should be noted that the injection cavity consists of all the fractures below the 27-ft level in well S1. Thus it is impossible to correlate the changes in flow rates with corresponding changes in fracture aperture. In any future study a packer placed below the deformation gauge would effectively isolate a single fracture in both wells.

Table 9. *In Situ* Fracture Deformation Test Data, September 14, 1973

Time (min)	Fracture deformation gauge (VDC)	Pressure in well S1 (psi)	Pressure in well S2 (psi)
0.00	1.4918	6.9	2.7
1.00	1.4915	6.8	2.7
2.00	1.4914	6.8	2.6
3.00	1.4906	6.8	2.6
4.00	1.4906	7.5	3.0
4.50	1.4905	7.3	3.1
5.00	1.4985	8.0	3.2
5.50	1.4904	12.0	3.9
6.00	1.5100	15.2	5.0
6.50	1.5350	16.5	7.5
7.00	1.5478	16.8	10.7
7.50	1.5570	17.5	12.3
8.00	1.5668	18.6	13.5
8.50	1.5753	19.2	14.7
9.00	1.5786	19.2	14.6
9.50	1.5822	19.4	14.6
10.00	1.5864	19.5	15.0
10.50	1.5898	19.7	15.2
11.00	1.5938	19.8	15.4
11.50	1.5959	20.0	15.6
12.00	1.5979	20.0	15.7
12.50	1.6010	20.2	16.0
13.00	1.6024	20.2	16.0
13.50	1.6023	20.0	15.7
14.00	1.6086	21.0	16.3
14.50	1.6172	21.5	17.0
15.00	1.6226	22.0	17.3
15.50	1.6235	22.0	17.4
16.00	1.6252	22.0	17.5
16.50	1.6263	22.0	17.7
17.00	1.6266	22.0	17.7
17.50	1.6285	22.0	17.7
18.00	1.6286	22.0	17.7
19.00	1.6570	22.5	17.7
19.50	1.6606	22.6	18.0
20.00	1.6820	26.5	19.0
20.50	1.6926	27.2	19.2
21.00	1.7016	27.6	19.5
21.50	1.7095	28.0	19.7
22.00	1.7122	28.4	20.0
22.50	1.7158	28.6	20.3
23.00	1.7424	28.7	20.6
23.50	1.7441	29.0	20.8
24.00	1.7453	29.2	20.9
24.50	1.7480	29.2	21.3
25.00	1.7483	29.2	21.5
25.50	1.7492	29.3	21.7
26.50	1.7270	26.0	21.6
27.00	1.7035	24.0	21.0
27.50	1.6870	23.0	20.0
28.00	1.6725	22.0	19.0
28.50	1.6650	19.0	6.0
29.00	1.5800	13.0	3.0

Table 9. Continued

Time (min)	Fracture deformation gauge (VDC)	Pressure in well S1 (psi)	Pressure in well S2 (psi)
29.50	1.5420	11.0	3.0
30.00	1.5262	10.5	3.0
30.50	1.5181	10.0	2.8
31.00	1.5120	9.5	2.8
31.50	1.5078	9.3	2.8
32.00	1.5040	9.2	-0.0
32.50	1.5024	9.0	-0.0
33.00	1.4995	9.0	-0.0
33.50	1.4983	8.9	-0.0
34.00	1.4967	8.8	-0.0
34.50	1.4951	8.8	-0.0
35.00	1.4940	8.8	-0.0
35.50	1.4930	8.7	-0.0
36.00	1.4608	8.4	-0.0
36.50	1.4612	8.4	-0.0
37.00	1.4616	8.2	-0.0

Note: Injection test and fracture deformation gauge are in well S1; S2 is the observation well. The fracture is located approximately 29 ft below ground surface.

Table 10. Pressure History Test Data for Fracture Deformation Test, September 14, 1973

Time (min)	Fracture deformation gauge (VDC)	Pressure in tank (psi)
0.00	1.4321	6.8
1.00	1.4322	6.8
2.00	1.4324	6.7
3.00	1.4323	6.8
4.00	1.4320	7.4
4.50	1.4319	7.4
5.00	1.4317	8.0
5.50	1.4310	12.0
6.00	1.4300	15.2
6.50	1.4308	16.5
7.00	1.4318	16.8
7.50	1.4317	17.4
8.00	1.4313	18.6
8.50	1.4312	19.2
9.00	1.4311	19.2
9.50	1.4308	19.4
10.00	1.4306	19.5

Table 10. Continued

Time (min)	Fracture deformation gauge (VDC)	Pressure in tank (psi)
10.50	1.4302	19.6
11.00	1.4302	19.8
11.50	1.4298	20.0
12.00	1.4296	20.0
12.50	1.4292	20.0
13.00	1.4290	20.0
13.50	1.4288	20.2
14.00	1.4276	21.0
14.50	1.4271	21.4
15.00	1.4263	22.0
15.50	1.4262	22.0
16.00	1.4260	22.0
16.50	1.4258	22.0
17.00	1.4254	22.0
17.50	1.4251	22.0
18.00	1.4248	22.0
18.50	1.4246	22.0
19.00	1.4231	22.6
19.50	1.4228	22.6
20.00	1.4129	26.5
20.50	1.4138	26.5
21.00	1.4120	27.5
21.50	1.4125	28.0
22.00	1.4121	28.4
22.50	1.4117	28.6
23.00	1.4267	28.7
23.50	1.4259	29.0
24.00	1.4258	29.1
24.50	1.4258	29.1
25.00	1.4257	29.2
25.50	1.4257	29.2
26.00	1.4278	26.4
26.50	1.4305	24.0
27.00	1.4303	23.1
27.50	1.4300	23.0
28.00	1.4306	22.1
28.50	1.4365	19.0
29.00	1.4374	13.0
29.50	1.4362	11.0
30.00	1.4359	10.1
30.50	1.4358	10.1
31.00	1.4358	9.4
31.50	1.4358	9.3
32.00	1.4358	9.0
32.50	1.4358	9.0
33.00	1.4358	9.0
33.50	1.4358	8.9
34.00	1.4358	8.8
34.50	1.4357	8.8
35.00	1.4357	8.8
35.50	1.4357	8.8
36.00	1.4357	8.5
36.50	1.4357	8.4
37.00	1.4357	8.2

In this test, the measured changes in aperture are in the order of 10^{-4} ft. After 18 min of testing the fluid pressures in both the injection and the observation well were approximately 15 psi (± 1 psi). The injection rate at this time was approximately stable at 0.0017 cfs. The increase in aperture, as measured at the injection well, was +0.000125 ft.

The pressures were then increased such that after 25 min, they were 22 psi and 19 psi, respectively. The steady-state injection rate increased to 0.00246 cfs and the change in aperture increased to 0.00023 ft. Thus there were increases of 45% in the injection rate and 84% in the opening of the fracture over those measured at 18 min.

Since the pressures are reported in terms of change from the initial condition, the total fluid pressure after 25 min is equal to approximately 1 psi per foot of depth. This may partly account for the relatively large increase in aperture. Also, the possibility of turbulent flow plus the nonuniform nature of the fracture aperture may have contributed to the smaller change in flow rate.

In a second injection test, the deformation gauge was locked in place across a fracture at the 20-ft level in well S1 (Fig. 49). Packers were placed above and below this fracture where it intersected well S2, isolating the fracture being tested from the rest of the fractures intersecting well S2. An inflatable packer was placed in well S1 several feet above the deformation gauge. Thus the fractures below the 19-ft level were hydraulically connected through well S1 with the injection cavity in S2. Water was injected into the fracture located between the two packers in well S2.

In Figure 49, the following are plotted: the flow rate of water being injected into the isolated fracture in well S2; the changes in fluid pressures (P_1) in the injection cavity (S2); the change in fluid pressures (P_2) at the deformation gauge (S1); and the changes in fracture aperture measured in S1 3 ft away from the injection point. Two distinct levels of pressure and flow rate were measured during the test. For a change in fluid pressure of 12.5 psi at the injection point, an increase of 8 psi was observed in the well containing the deformation gauge. Thus there was a drop of 36% in the fluid pressure over a radial distance of 3 ft. This is significantly different from the ratio of P_2 to P_1 shown in Figure 48 for the fracture at the 29-ft level. For the results given in Figure 49 it should be remembered that well S1 was open below the deformation gauge and water was being injected into fractures below the 20-ft level and intersecting this well. Since the fractures below the 20-ft level all have smaller equivalent fracture apertures than the fracture being tested (Table 5), it can safely be assumed that the fluid pressure P_2 in Figure 49 is only slightly lower than would have been recorded if the fracture had been completely isolated in both wells. The flow rate corresponding to the injection

pressure above was 0.0022 cfs. The change in fracture aperture measured in well S1 was 0.000117 ft.

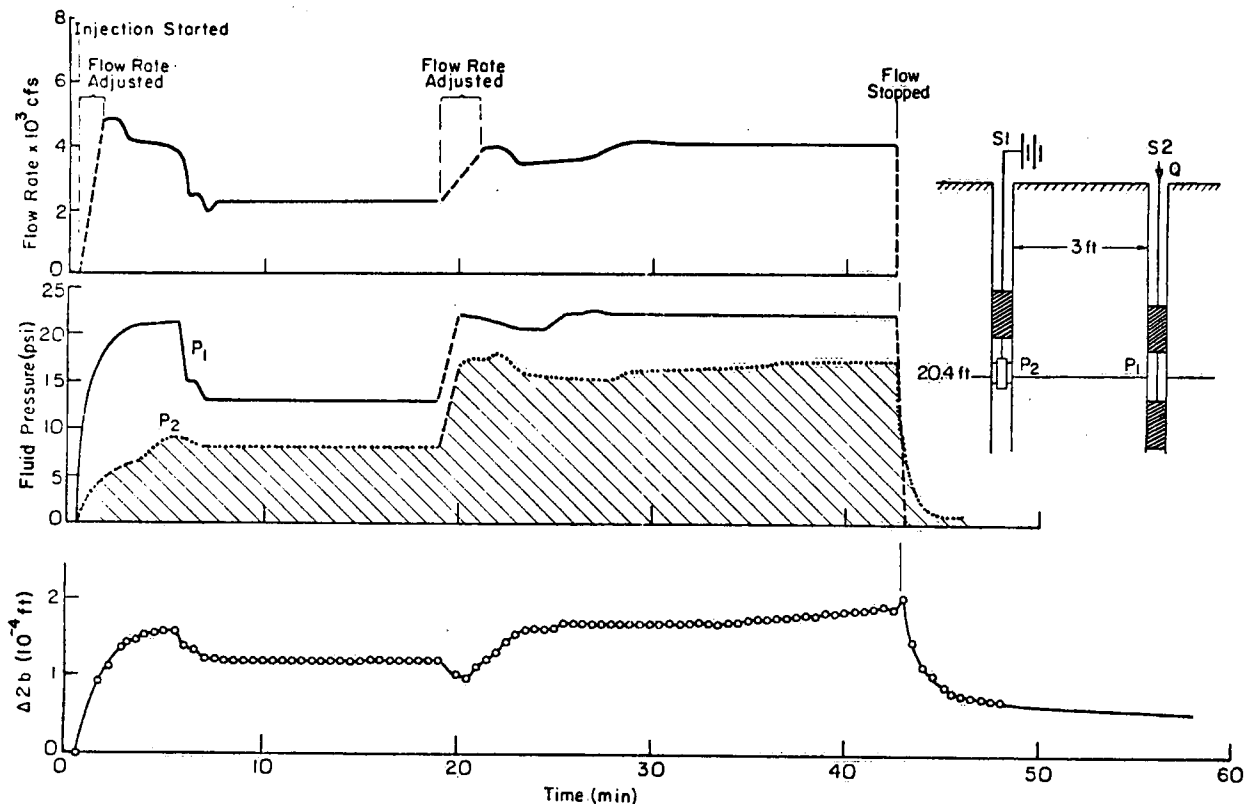


Figure 49. Results from an injection test in well S2 with the fracture deformation gauge locked across the fracture at the 20-ft level in S1. Water level at start of test was ~8 ft below ground surface.

After approximately 20 min, the injection pressure was suddenly increased by adjusting the flow rate. This increase in pressure caused the fracture deformation gauge to slip in the borehole. The steady-state pressures after 40 min were 22 psi (P_1) and 17 psi (P_2). The measured flow rate was 0.0041 cfs. The change in fracture aperture was 0.00018 ft. It should be noted that the indicated change in aperture is much smaller than the actual fracture deformation because of the instrument slippage. Thus if the amount of slippage was added to the indicated deformation, the change in aperture would be approximately 0.00025 ft.

After the injection test had been stopped, the fracture aperture did not return to its original value. This is partly related to transient effects, since fluid pressures within the fracture plane had not yet returned to their original values. These effects are more easily appreciated if a fracture of nonuniform aperture is visualized as consisting of

a series of segments having alternating large and small apertures. After fluid pressures have been increased, some period of time is required for the system to reach equilibrium in all of these segments again. Reestablishment of fluid pressure equilibrium, however, may not provide the complete explanation for the observed residual fracture opening. Part of the residual may represent instrument slippage or propping of the fracture through movement of broken rock chips during fluid injection.

Using the same test arrangement, the fracture at the 20-ft level was again tested. In this second test, water was injected into well S1 which contained the fracture deformation gauge. The double packer straddling the fracture in well S2 was now used as a fluid pressure measuring point. It should be noted that in this test the water was being injected into the entire fracture system below the 19-ft level.

The results from this test are presented in Figure 50. The fluid pressures measured in well S2 (P_2) are unreliable due to packer leakage and problems with the pressure transducer. The measured changes in aperture show an initial opening of the fracture corresponding to the initial increase in fluid pressure. Then, with the pressure remaining constant, the fracture gradually closed again and did not reopen until the fluid pressure

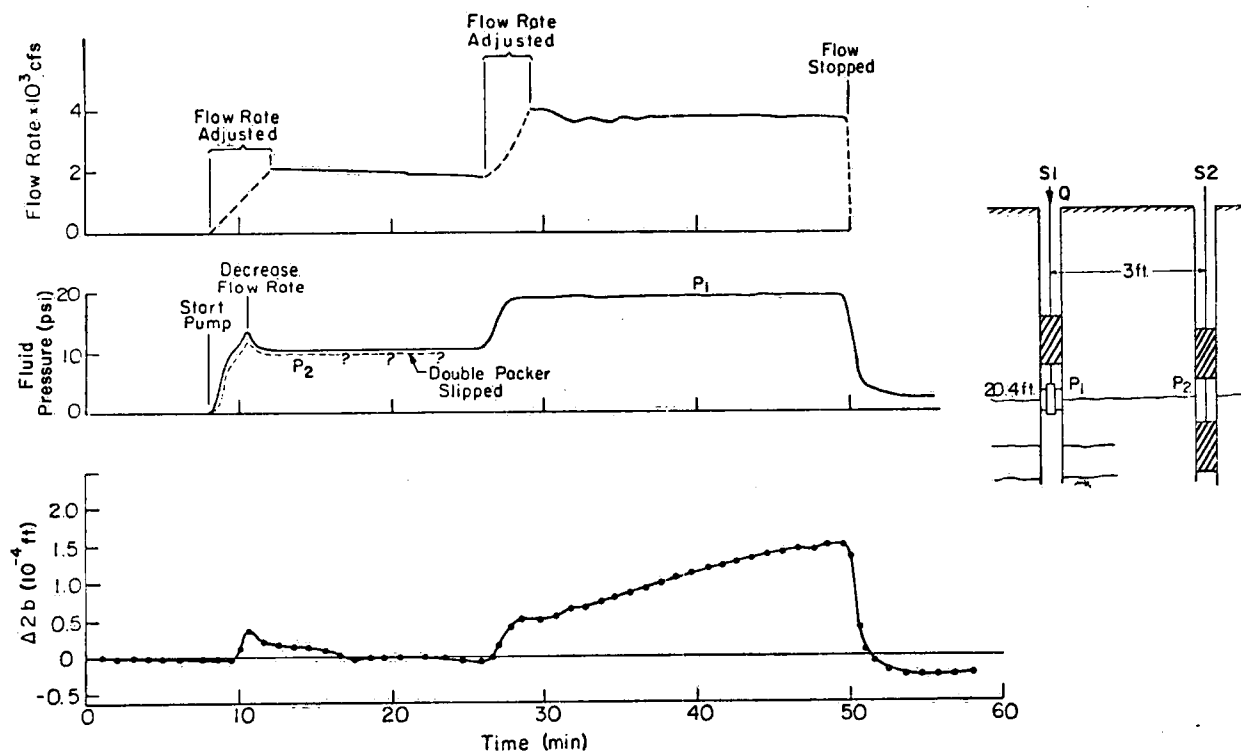


Figure 50. Results from an injection test in well S1 with the fracture deformation gauge locked across the fracture at the 20-ft level in S1. Water level at start of test was ≈ 13 ft below ground surface.

was again increased. Then the aperture steadily increased and reached a constant value near the end of the test.

The changes in aperture in Figure 50 are significantly different from those in Figure 49. The only difference in procedure for the two tests was the injection into an isolated fracture in one instance and the injection into the major part of the fracture system in the second.

In an attempt to explain the differences in behaviour evident in Figures 49 and 50, it may be recalled that Benko (1966) has reported grouting operations followed by excavation of the grouted region that have shown a preferential opening and closing of fractures, i.e., some fractures are extensively filled with grout, whereas others are not. This suggests that preferential opening and closing of fractures is a possible explanation for the phenomena observed in the two field experiments described above.

In fluid injection, the total stress acting on the rock mass is not being changed. Thus the distribution of fluid pressures within the fracture plane determines the changes in effective normal stress acting across the fracture and hence the magnitude of the change in aperture. In Figure 49 the injection was only in one fracture, and thus any change of pressure in other fractures can only result from the short-circuiting effect of the observation well (S1). As in Figure 49, the pressure in S1 is much less than the injection pressure in S2. Thus the forces owing to fluid pressure in the fracture at the 20-ft level are always greater than the forces developing in the other fractures intersecting well S1. This is no longer true when well S1 is used as the injection well (Fig. 50). In this case, water is being injected into the fracture at the 29-ft level as well as into the other fractures below the 19-ft level. The data in Figures 48 and 49 indicate that the fluid pressures are propagated a greater distance from the injection point in the fracture at the 29-ft level than in the fracture at the 20-ft level. Therefore, for any given injection pressure, a greater force will be developed in the fracture at the 29-ft level and this fracture will open at the expense of other fractures along the same borehole in which smaller fluid pressure forces have developed.

Thus, it is suggested that Figure 50 shows the initial closing of the fracture at the 20-ft level owing to the development of greater fluid pressure forces in adjacent fractures. As the pressures are propagated within the fracture plane at the 20-ft level, the fluid forces become sufficient to balance the forces in the other fractures and hence the fracture opens to some equilibrium state. The small residual closure of the fracture at the end of the test is most likely due to instrument slippage or transient effects.

Also, it should be recalled that Shehata observed that a withdrawal test in a well in a shear zone resulted in an increase in the water level in a nearby well in the country rock. The initial fracture opening shown in Figure 50 may have resulted from a similar set of factors, i.e., the greater fluid pressure forces in the lower fractures may have resulted in an increase in the pressure in the plane of the fracture being tested, and hence, the fracture would open. When a steady state was reached, these fluid forces were balanced and the fracture closed. It should be noted that the fracture did not start to reopen until the fluid pressures were almost equal to 1 psi per foot of depth.

Numerical Simulation of the Fracture System at Sambro, Nova Scotia

COMPARISON OF MEASURED CHANGES IN FRACTURE APERTURES WITH NUMERICAL MODEL RESULTS

Using the field and laboratory data presented in Chapter 3, a finite-element model of the fracture system at the Sambro test site was constructed. This finite-element mesh was employed in Chapter 2 with idealized apertures and material properties to demonstrate the effect of deformable fractures on flow rates and fluid pressure distributions. In this section, the changes in apertures measured in the field are compared with those calculated using the numerical model.

Figure 51 depicts the numerical model representation of the test site. This model incorporates nearly all the available field and laboratory data from the site. The principal compressive stresses shown as line vectors within each rock block and the effective normal stresses plotted across each fracture element are due to the interaction of the gravity forces and the initial fluid pressures only. The magnitude of the stresses is related to depth below the ground surface.

The fracture system at the site is represented by seven discrete horizontal fractures with the same spacing and aperture distribution as described in Chapter 3 (Table 8). This, of course, entails some degree of idealization in representing the geometry and continuity of the fractures over a radial distance of 150 ft.

The description of the fracture system given in Chapter 3 justifies the idealization of the fracture system as completely horizontal, at least in the immediate vicinity of wells S1 and S2. Because of the rapid radial drop in pressure, the geometry of the fractures beyond 30 ft from the point of fluid injection or withdrawal does not significantly affect the overall site simulation.

The fracture apertures used in this model are listed in Table 8. The well, 0.25 ft in diameter, is assumed to be 50 ft deep having a radius of influence of 150 ft (Chapter 3). A Young's modulus of 4.72×10^8 psf and a Poisson's ratio of 0.28 were determined from uniaxial compression tests on drill core samples. It was not possible to obtain undisturbed samples of the natural fractures from the site for laboratory stiffness testing.

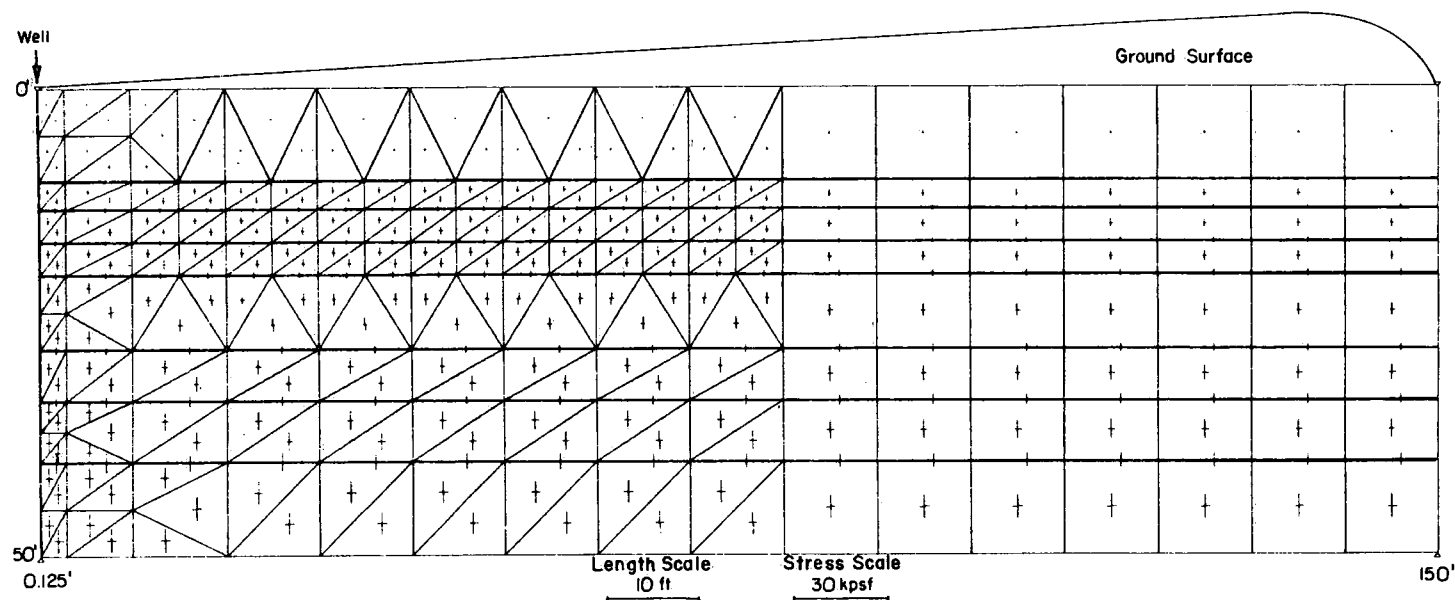


Figure 51. Finite-element model of fracture system at Sambro showing principal compressive stresses within the rock elements and the effective normal stresses across the fractures owing to gravity forces. Maximum and minimum principal stresses are shown by scaled line vectors within each block; effective normal stress is indicated by vertical line segment across each fracture.

One possible approach in determining the material characteristics of the fractures for modelling purposes is to use normal stiffness (K_N) and shear stiffness (K_S) values determined from laboratory tests on similar rock types by other workers, e.g., Goodman and Dubois (1972). Much of this laboratory work, however, has involved artificial fractures subjected to normal stresses that are very high in comparison with the small changes in effective stress occurring during this field investigation.

Natural fractures, when tested in the laboratory, must undergo some disturbance during the extraction process which affects their displacement behaviour at low stresses. The size of the rock sample that can be tested in the laboratory is generally restricted, with the maximum size of the actual fracture plane being in the order of tens of square inches. The small size of the sample results in the imposition of somewhat artificial boundary conditions during the laboratory test. It is possible to conduct large-scale field tests on natural fractures (Pratt, Swolfs and Black, 1974), but these are generally very expensive and time consuming.

In measuring the changes in fracture apertures during the field investigation, an *in situ* measure of the normal stiffness of the fractures is actually obtained, i.e., both the change in fluid pressure (change in effective stress) and the change in aperture (fracture deformation) are measured in the borehole. If the distribution of fluid pressures in the fracture plane can be determined, then a close approximation can be made to the force being applied to produce the measured fracture deformation. During the tests at Sambro, the fluid pressures were measured at two points within the fracture plane: (a) at the injection or withdrawal well and (b) in a second well located at a radial distance of 3 ft. Thus the force being applied over an area of the fracture plane that is measured in tens of square feet can be estimated. In the case of a nonuniform aperture, where there is very little head loss within the first few feet from the well, measuring the pressures at several points gives a very close approximation to the change in effective stress within the fracture plane. Also, small-diameter holes can easily be drilled in a pattern around the test well to obtain more complete information on the pressure changes within the fracture plane. *In situ* measures of the force-displacement relationships of fractures are more representative of the behaviour of fractures within a rock mass because of the natural boundary conditions and larger area being sampled.

Figure 52 presents field results from the Sambro site for the aperture changes resulting from changes in fluid pressure. This Figure is a force-displacement curve and may be used for the estimation of K_N , the normal stiffness (Fig. 5). The original data used to compile sections A and B of Figure 52 are presented in Figures 47, 48 and 49. The pressure values were averaged from the measurements made at S1 and S2. The results plotted in section A of Figure 52 show the effects of both injection and withdrawal for the fracture at the 29-ft level, whereas in section B of Figure 52, only the effects of injection are

given for the fracture at the 20-ft level. In addition, to obtain a second data point in section B it was necessary to correct the measured aperture change of 0.00018 ft for an estimated instrument slippage of 0.00007 ft. This gave a total deformation of 0.00025 ft.

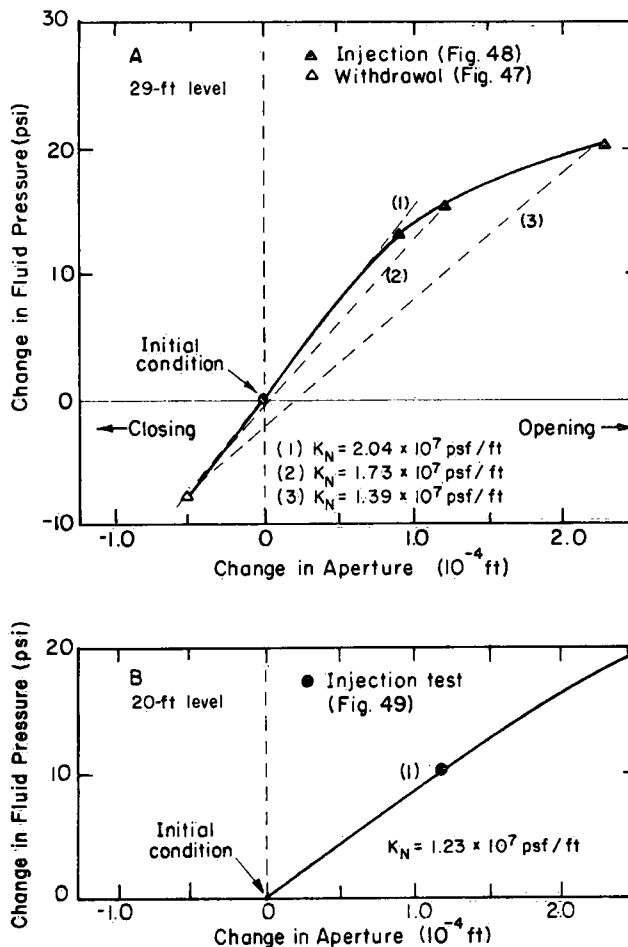


Figure 52. Force (fluid pressure) - normal displacement relationships determined from field data for fractures at 29-ft and 20-ft levels.

The slopes of the three line segments shown in section A represent different normal stiffness values calculated from the field data for the fracture at the 29-ft level:

- (1) $K_N = 2.04 \times 10^7$ psf/ft,
- (2) $K_N = 1.73 \times 10^7$ psf/ft, and
- (3) $K_N = 1.39 \times 10^7$ psf/ft.

Section B gives a rather uniform slope of $K_N = 1.23 \times 10^7$ psf/ft passing through the mid-point of the curve. Because of the greater head loss in this fracture at the 20-ft level as compared with that in the fracture at the 29-ft level, averaging the fluid pressures at the injection well and the observation well may not give a good approximation of the change in effective stress. Assuming a possible error of -20% in the calculated value of the

averaged fluid pressure, from the measured displacements a K_N value of 9.87×10^6 psf/ft would be calculated; similarly, assuming a possible error of +25%, a K_N value of 1.54×10^7 psf/ft would be obtained.

With these values for the normal stiffness, the numerical model was used to determine displacement values for the same pressure changes as those observed in the field. Table 11 presents a comparison of displacements as measured in the field and those calculated from the numerical model for the fracture at the 29-ft level. Table 12 lists the results of the same calculations for the fracture at the 20-ft level.

In both cases the lowest K_N values give the best overall agreement with the field measurements. These results, especially those presented for the fracture at the 29-ft level, indicate the shortcomings of the straight-line approximation to determination of the K_N values that is the basis of the stiffness perturbation method used to model the force-displacement characteristics of fractures. The nonlinear nature of the fracture deformation cannot be modelled accurately using the straight-line approach, especially when the change in effective stress is a significant percentage of the initial effective stress. A constitutive relationship that follows the real force-displacement curve would give better results when comparing field or laboratory data with numerical model results.

Because of equipment limitations, the change in flow rates associated with a given change in fracture aperture could not be determined during the field tests. Thus the flow rates ascertained from the model calculations cannot be compared with those measured in the field. Flow rates for the individual fractures have been calculated using the numerical model and are listed in Tables 11 and 12 for the lowest K_N values. The results are expressed as a percentage of the flow rate in the corresponding rigid fracture with the same fluid pressure changes. These results show that the fracture deformations produce a significant (up to 60%) increase or decrease in flow rates in individual fractures as compared with rates for flow in a rigid system.

EFFECT OF FRACTURE DEFORMATION AND FRACTURE LOCATION ON SIMULATED PUMP TEST RESULTS

In this section, the effects of fracture deformation on flow rate during pumping-out tests are investigated using both (1) nonuniform and (2) equivalent uniform apertures. In addition, the importance of depth below the water table at which the larger fractures intersect the borehole is considered.

The model presented in Figure 51 and the fracture data given in Table 13 were used in this study. All other material properties were the same as those mentioned earlier

Table 11. Comparison of Field Measurements and Numerical Model Results of Fracture Deformation for the Fracture at the 29-ft Level

Measuring point (well)	Field measurements		Numerical results $\Delta 2b \times 10^3$ ft			$\frac{Q_D - Q_R}{Q_R} \times 100$ ($K_N = 1.39 \times 10^7$ psf/ft) (%)
	Fluid pressure (psi)	$\Delta 2b \times 10^3$ (ft)	$K_N = 2.04 \times 10^7$ psf/ft	$K_N = 1.73 \times 10^7$ psf/ft	$K_N = 1.39 \times 10^7$ psf/ft	
Injection well (P_1)	13.0	+0.092	+0.069	+0.082	+0.101	33.1
Observation well (P_2)	12.5	-	+0.0687	+0.081	+0.100	
Injection well (P_1)	22	+0.233	+0.116	+0.137	+0.169	+60.8
Observation well (P_2)	19	-	+0.115	+0.136	+0.167	
Withdrawal well (P_1)	0.0(-7.5)	-	-0.0360	-0.0437	-0.0543	-16.2
Observation well (P_2)	0.0(-7.5)	-0.05	-0.0356	-0.0430	-0.0535	

* Q_D = Flow rate in deformable fracture.

Q_R = Flow rate in rigid fracture.

Note: The percentage change in flow rate is also given for the lowest K_N value.

Table 12. Comparison of Field Measurements and Numerical Model Results of Fracture Deformation for the Fracture at the 20-ft Level.

Measuring point (well)	Field measurements		Numerical results $\Delta 2b \times 10^3$ ft			$\frac{Q_D - Q_R}{Q_R} \times 100$ ($K_N = 9.87 \times 10^6$ psf/ft) (%)
	Fluid pressure (psi)	$\Delta 2b \times 10^3$ (ft)	$K_N = 1.54 \times 10^7$ psf/ft	$K_N = 1.23 \times 10^7$ psf/ft	$K_N = 9.87 \times 10^6$ psf/ft	
Injection well (P_1)	13	-	0.063	0.077	0.0935	25.7
Observation well (P_2)	8	0.125	0.057	0.070	0.0860	
Injection well (P_1)	22		0.114	0.139	0.170	50.0
Observation well (P_2)	17	0.175	0.102	0.127	0.158	

* Q_D = Flow rate in deformable fracture.

Q_R = Flow rate in rigid fracture.

Note: The percentage change in flow rate is also given for the lowest K_N value.

in this Chapter. The pumping well was assumed to be 50 ft deep with the static water level at 9 ft. A constant-head boundary was assigned at a radius of 150 ft. During the pump test the water level in the well was dropped to the 40-ft level, i.e., the level at which the lowest fracture intersects the well. Thus the initial fluid pressures were set equal to zero at the points where the fractures intersected the pumping well.

Table 13. Properties of the Fracture System Used in Simulated Pump Tests

Depth to fracture (ft)	Nonuniform apertures		Equivalent uniform apertures (ft)	Stiffness values $K_N = K_S$ (10^7 psf/ft)	Initial fluid pressure (psf)
	$r < 3'$ (ft)	$r < 3'$ (ft)			
10	0.01008	0.003037	0.0037	1.2	62
13	0.00154	0.00062	0.0007	1.2	250
16.5	0.00014	0.00014	0.00014	1.2	468
20	0.00085	0.0008	0.00084	0.987	686
28	0.00114	0.00055	0.00069	1.39	1,186
33.5	0.00011	0.00011	0.00011	1.2	1,435
40	0.00017	0.00005	0.00015	1.2	1,934

Table 14 lists the results of a simulated pump test where the fractures intersecting the well have nonuniform apertures. The flow rates in the individual fractures were calculated for both the rigid fracture case and the case in which the fractures were allowed to deform. For each fracture the change in flow rate is expressed as a percentage of the flow rate in the corresponding rigid fracture. The total discharge for all fractures is also included.

Table 14. Results of Simulated Pump Test with Nonuniform Apertures

Depth to fracture (ft)	Q_R	Q_D	$\frac{Q_R - Q_D}{Q_R} \times 100$
	Rigid fracture system (10^{-4} cfs)	Deformable fractures (10^{-4} cfs)	(%)
10	-137.13	-136.9	-0.2
13	-4.329	-4.16	-4.0
16.5	-0.0402	-0.0401	-0.3
20	-12.26	-11.41	-7.0
28	-13.61	-11.3	-17.0
33.5	-0.0598	-0.0507	-15.0
40	-0.0194	-0.0190	-2.1
All fractures	-167.45	-163.88	-2.1

Table 15 presents similar results for the nonuniform fracture system for which the large fracture at the 10-ft level has been interchanged with the smaller fracture at the 40-ft level.

Table 15. Results of Simulated Pump Test with Nonuniform Apertures with Fractures at 10-ft and 40-ft Levels Interchanged

Depth to fracture (ft)	Q_R Rigid fracture system (10^{-4} cfs)	Q_D Deformable fractures (10^{-4} cfs)	$\frac{Q_R - Q_D}{Q_R} \times 100$ (%)
10	-0.00061	-0.00060	-1.6
13	-4.329	-4.18	-3.4
16.5	-0.0402	-0.0398	-1.0
20	-12.26	-11.56	-5.7
28	-13.61	-11.47	-15.7
33.5	-0.0598	-0.0597	-0.2
40	4,251.0	3,971.0	-6.6
All fractures	-4,281.30	-3,998.31	-6.61

In Tables 16 and 17, the results from the same series of calculations are given for a simulated pump test where the fractures intersecting the well have equivalent uniform apertures.

Table 16. Results of Simulated Pump Test with Equivalent Uniform Apertures

Depth to fracture (ft)	Q_R Rigid fracture system (10^{-4} cfs)	Q_D Deformable fractures (10^{-4} cfs)	$\frac{Q_R - Q_D}{Q_R} \times 100$ (%)
10	-98.96	-98.90	-0.06
13	-2.68	-2.62	-2.2
16.5	-0.0402	-0.0401	-0.25
20	-12.73	-11.84	-7.0
28	-12.19	-10.85	-11.0
33.5	-0.0598	-0.0567	-5.2
40	-0.2043	-0.2040	-0.2
All fractures	-126.86	-126.41	-0.4

A comparison of the results presented in Tables 14 through 17 shows that the greatest change in flow rates between the rigid and the deformable systems occurs for fractures with nonuniform apertures. This is a direct effect of the initial fluid pressures

being changed over a greater area during the withdrawal test resulting in a greater change in aperture. A comparison of the results in Tables 14 and 15 and Tables 16 and 17 shows the dominant effect of the larger fractures and the importance of the depth at which the larger fractures intersect the well bore.

Table 17. Results of Simulated Pump Test with Equivalent Uniform Apertures with Fractures at 10-ft and 40-ft Levels Interchanged

Depth to fracture (ft)	Q_R Rigid fracture system (10^{-4} cfs)	Q_D Deformable fractures (10^{-4} cfs)	$\frac{Q_R - Q_D}{Q_R} \times 100$ (%)
10	-0.0066	-0.0065	-1.5
13	-2.68	-2.63	-1.9
16.5	-0.0402	-0.0401	-0.3
20	-12.73	-11.92	-6.4
28	-12.19	-11.02	-9.6
33.5	-0.0598	-0.0577	-3.5
40	-3,066.0	-2,952.0	-3.7
All fractures	-3,093.7	-2,977.7	-3.8

The discrepancies between the flow rates for rigid fractures with nonuniform apertures (column 2, Tables 14 and 15) and equivalent uniform apertures (column 2, Tables 16 and 17) are due to round-off errors in calculating the equivalent fracture apertures. These are magnified because of the cubic dependence of flow rate on aperture size. The corresponding discrepancies for the nonuniform and equivalent uniform deformable fractures (column 3, Tables 14 to 17) are due to the iterative method of solution used in this numerical approach and the relative degree of convergence obtained.

Although the maximum change in total flow rate for the simulated pump tests is 6.6%, it should be noted that a change in the pumping rate of as little as 4% introduces a significant error into the interpretation of the pump test data (Mr. T. Hurr, USGS, Denver, Colorado, personal communication, 1972). Using Gale and Welhan's (1975a) discharge control tank, the well discharge can easily be controlled during a pumping test. Thus if the fracture deformation changed the permeability of the fracture system during a pump test, it should be reflected in the rate of drawdown being measured in the pumping well.

Figure 53 shows the drawdown versus time data for two separate pump tests in closely spaced wells drilled in the same rock unit as that found at the Sambro test site. The well discharge during each pump test was kept at a fixed rate by using the discharge control tank. The drawdowns were measured in the pumping well and water levels in the observation well were not affected.

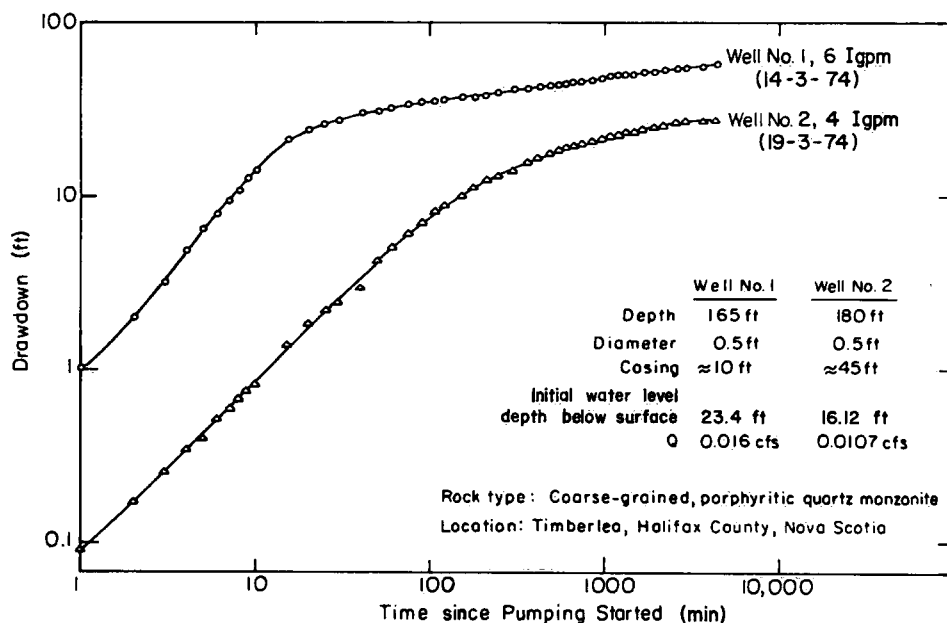


Figure 53. Drawdown data measured in the pumping well during two separate pumping tests on two separate wells.

To date, there is no method of determining what effect fracture deformation has on the rate of drawdown during such pump tests. To estimate such effects the points at which the major water producing fractures intersect the pumping well (the permeability profile) must be known. A simple and inexpensive method for determining the permeability profile of wells with low specific capacities, such as wells drilled in fractured crystalline and metamorphic rocks, is presented in the Appendix. Thus pump test data obtained in wells where the discharge is constant and the permeability profile known would enable one to determine whether permeability changes owing to fracture deformation could be identified and assessed from drawdown data.

SUMMARY

There is very good agreement between the changes in apertures measured in the field and those calculated using the numerical model. The normal stiffness values determined using the field measures of fracture displacement and changes in fluid pressure are slightly lower than those determined for similar rock types from laboratory tests. This is consistent with the highly weathered nature of the fractures observed in the field as compared with the fresh (and hence stiffer) surfaces of the fractures tested in the laboratory. The approach used in this study may be valuable in determining the *in situ* material characteristics of fractures at shallow to moderate depths below the ground surface.

The simulated pump tests for the fracture system at Sambro show the importance of controlling well discharge during a pump test and the need to determine permeability profiles of wells completed in fractured rock aquifers. In addition, representing nonuniform apertures as equivalent uniform apertures gives an incorrect indication of changes in fluid pressures and, hence, of both the magnitude of fracture deformation and the resulting change in flow rates for deformable fracture systems.

Laboratory Study of Injection and Withdrawal Tests Using Large-Diameter Rock Cores

INTRODUCTION

The third part of this research program is a laboratory study of fluid injection and withdrawal in artificial fractures using a large-diameter rock core. The core selected is 38 in. in diameter and 6 ft long. Both a fracture cut with a wire saw and a tension fracture were studied. In addition, a nonuniform fracture was created by sandblasting the saw-cut fracture surface over a given radius.

The main objective of this laboratory study was to determine whether the pattern of fracture deformation observed in the field could be reproduced qualitatively. Thus during the study the changes in fracture aperture associated with known changes of fluid pressure and the corresponding changes in flow rate were measured under controlled laboratory conditions. Also, fluid pressures were measured at several points within the fracture plane. It should be noted that the artificial fractures investigated in the laboratory were much stiffer than the highly weathered fractures at the Sambro test site. All of the displacements measured during these tests were normal to the fracture surfaces.

DESCRIPTION OF EXPERIMENT

Sample Preparation

A 38-in. diameter granite rock core (Fig. 54) was obtained from the Cold Springs Granite Company near Raymond, California. The core was trimmed on both ends to a length of 6 ft using wire saws, with an effort being made to achieve as good a degree of parallelism as possible. The total weight of the core was 8,000 lb.

The quarry operators were asked to drill an NX hole along the axis of the core. Since they did not have a rotary drill, a 2-in. diameter percussion drill hole was made to within 6 in. of the bottom of the core. This hole had to be enlarged after the core had been delivered to the test facility.



Figure 54. Granite core (38-in. diameter) at Cold Springs Co. quarry near Raymond, California.

After the centre hole had been drilled at the quarry, the core was cut at the midpoint with a wire saw to simulate a horizontal fracture perpendicular to the axis of the core. Before the core was cut, reference marks were made across the proposed cut to enable the halves of the core to be fitted back together as closely as possible to the original position. In each 3-ft section, 0.75-in. diameter holes, 3 in. deep, were drilled at 8-in. intervals around the circumference midway between the top and bottom of the section (Fig. 55). These holes made it possible to split the core to create a rough tension fracture. Finally, a total of 12 holes, 4 in. deep and approximately 2 in. in diameter, were drilled at 120° intervals along a circumference in each of what were to become the four sections of rock. Eyebolts cemented into these holes with a strong epoxy provided a means of shifting the core sections using an overhead crane. The core, as prepared and delivered by the quarry operators, is shown in Figure 55.

Figure 56 shows the core halves, indicating the locations of the centre hole and the positions of the LVDTs used to measure changes in fracture aperture. Note that these changes were measured at three points on the surface of the core and also at the centre of the core where the fracture intersects the centre hole. A metal sleeve (Fig. 56) was glued into the centre hole at the top of the upper block. An O-ring was machined into the outside of this sleeve such that it would fit to the sample cap.

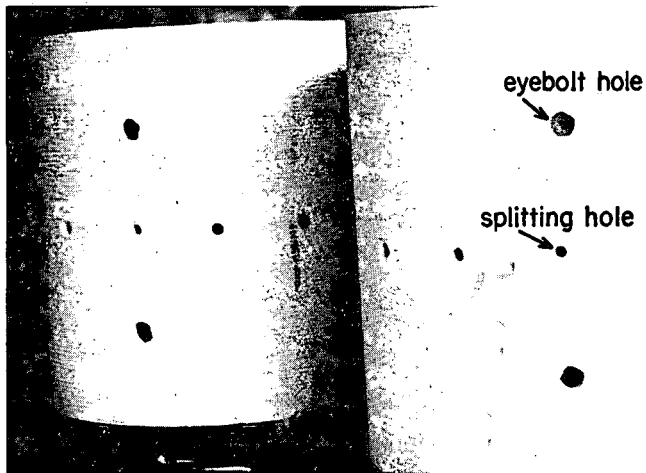
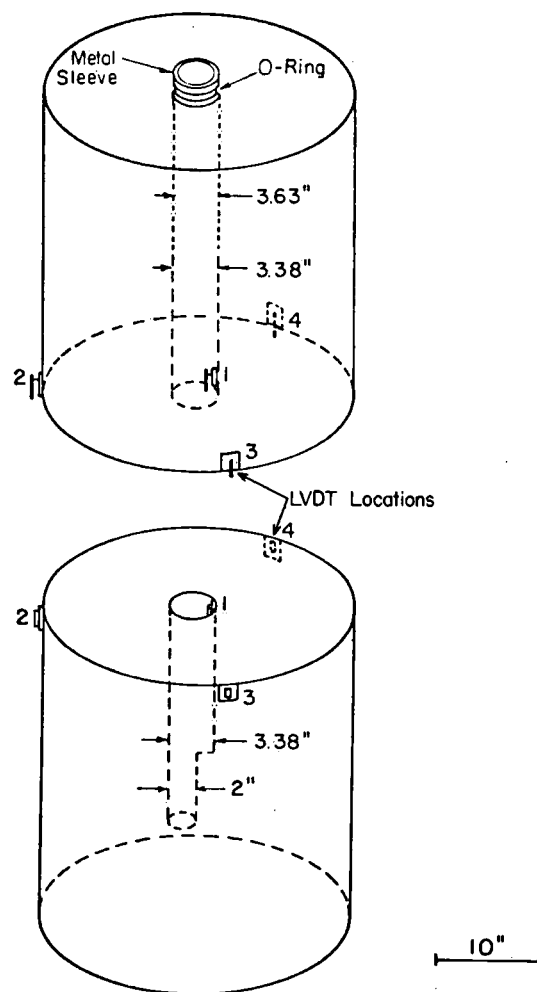


Figure 55. Both halves of 38-in. diameter core showing anchor and splitting holes.

Figure 56. Schematic diagram of core showing location of centre hole and four LVDTs.



In the case of the tension fracture, metal guides were placed across the anticipated location of the fracture plane. This ensured that the rough surfaces would be properly rematched. Figure 57 indicates the guides with the connecting rods and the location of the splitting holes.

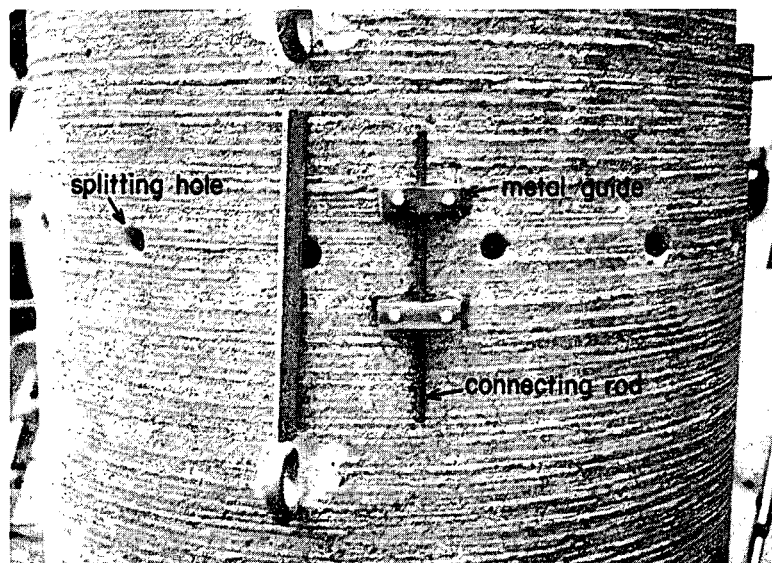


Figure 57. Location of splitting holes and reference guides for rematching tension fracture.

Material Properties

The rock core used in this experiment is identified by the Cold Springs Granite Company as Sierra White Granite. The approximate mineral composition has been estimated from thin section analysis as follows:

Mineral	Approximate composition (%)
Quartz	20
Plagioclase (An ₂₀ , partially altered to sericite)	30
Feldspar (partially altered to sericite)	25
Biotite (some alteration to chlorite)	10
Muscovite	10
Chlorite	2
Alteration minerals	2
Minor accessories	1

The rock specimen is grayish white and fine-grained to medium-grained with a uniform texture. On the basis of the description above and thin section analysis, the rock can be classified as a grayish-white muscovite-biotite quartz monzonite.

During this experiment the large rock core was subjected to repeated stress cycles up to 2,500 psi - approximately 15% of the compressive strength of the rock. To determine whether this repeated loading would have any effect on the material characteristics of the rock, cycle uniaxial compression tests were performed on 2-in. diameter cores, 4 in. long. The cores were drilled from samples of the same rock collected at the Raymond Quarry. The tests followed the ASTM C170-50 test specifications; the results for two test cores are given in Table 18.

Table 18. Results of Cyclic Compression Tests on Sierra White Granite

Sample number	Cycle number	Maximum compression σ_{\max} (psi)	Young's modulus E (psi)
1	1	5,000	5.77×10^6
	2	5,000	5.88×10^6
2	1	5,000	5.88×10^6
	2	5,000	5.77×10^6
	3	5,000	5.88×10^6

These results show that for the range of stresses applied during testing of the large rock core, no significant change was to be expected in the stress-strain relationship of the rock itself. A partial stress-strain curve for sample No. 1 is given in Figure 58 and a complete set of stress-strain curves, in Figure 59.

Test Procedure - Sample Instrumentation

The large-scale triaxial testing facility at the Richmond Field Station of the University of California, Berkeley, is the largest piece of equipment used in this study. It consists of an 80-in. inside diameter chamber on a heavy, movable steel base and a loading frame that can apply an axial load of 4 million pounds. The test chamber has been routinely tested to 750-psi water pressure during testing of rockfill materials (Becker, Chan and Seed, 1972). The test chamber can accommodate specimens up to 80 in. in height.

The core was prepared for testing in the large triaxial cell as shown in Figure 60. The preparation consisted of mounting LVDTs across the saw-cut fracture and attaching strain gauges to the surface of the rock core to measure both horizontal and vertical strains. A 2-in. thick aluminum plate was placed on top of the core. Two holes were drilled from the edge to the centre of this plate. Also, a hole, 1 in. deep and 3 in. in diameter, was cut out at the centre of the plate. This recess is directly over and fitted to the

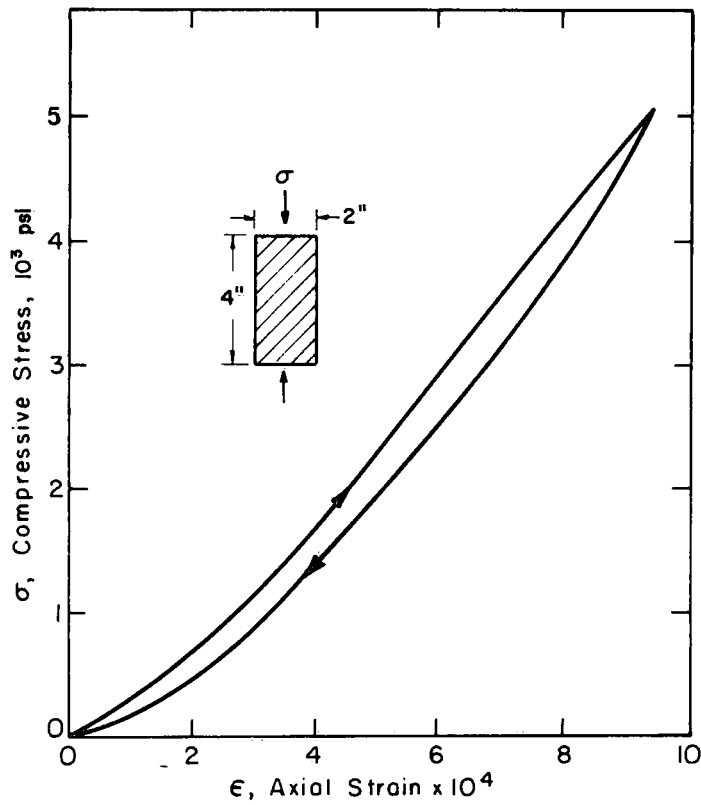
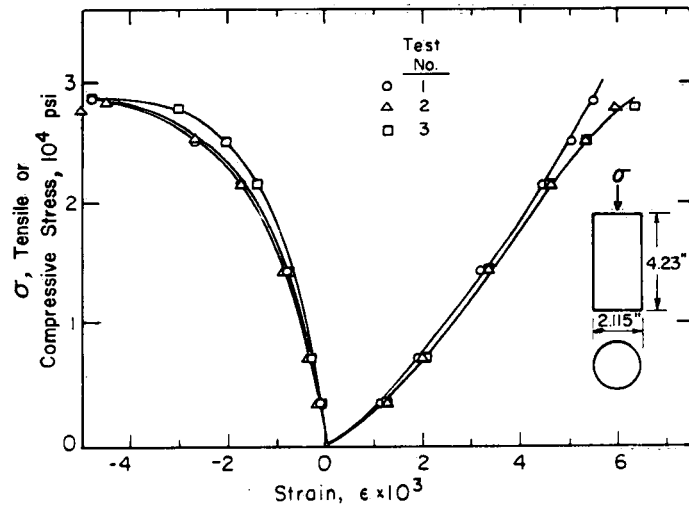


Figure 58. Partial stress-strain curve for sample No. 1.

Figure 59. Complete stress-strain curve for three samples of Sierra White Granite from Raymond, California. (Courtesy of H. Pratt, Terratek, Salt Lake City, Utah.)



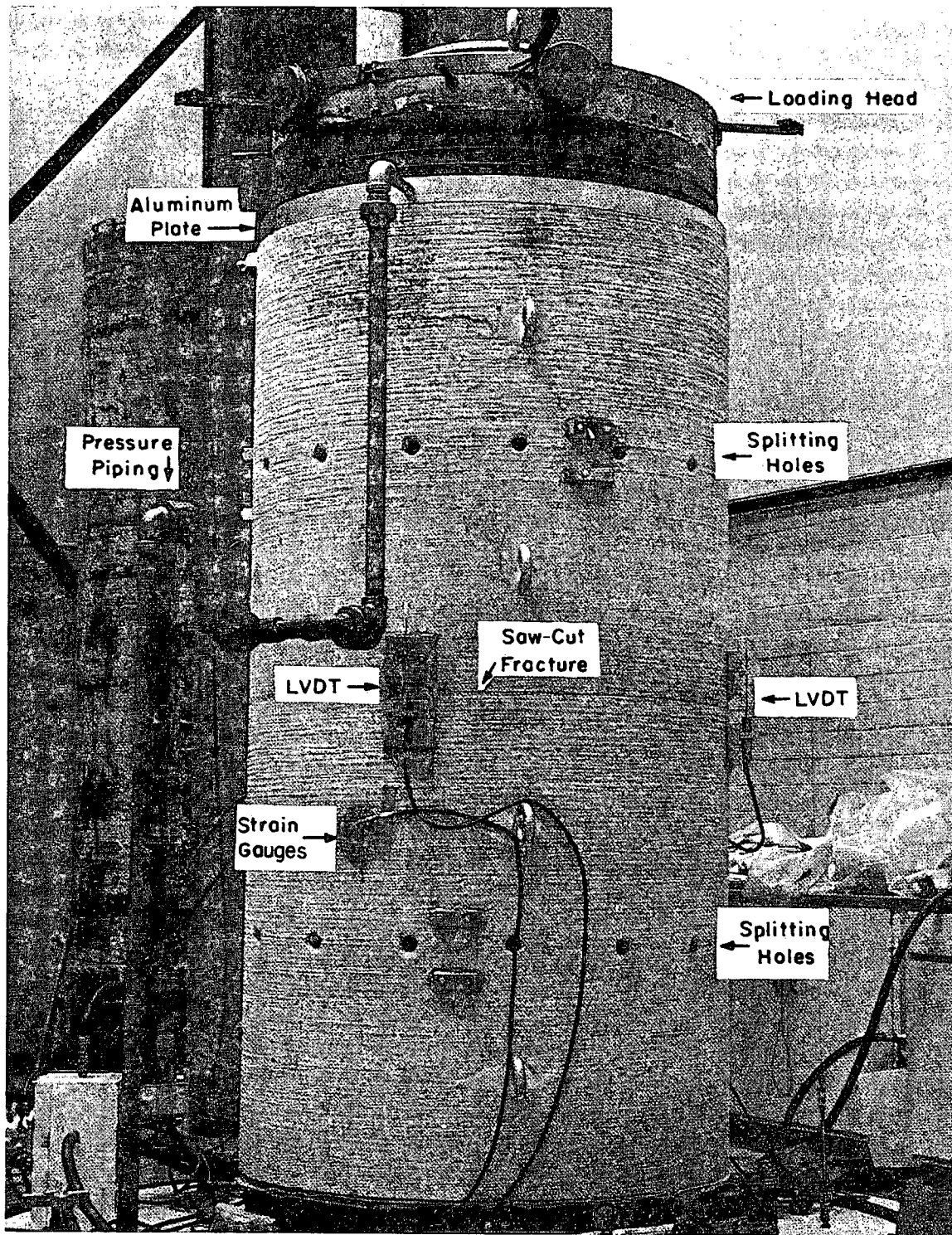


Figure 60. Large-diameter core prepared for testing.

metal sleeve in the centre hole in the rock core and allows water to flow into and out of the core. One hole in the plate serves as an injection path and the second permits the wires connecting the LVDTs in the centre of the rock core to be brought to the outside of the core through watertight fittings. Additional LVDTs were attached across the tension fracture after splitting the core. A 3-in. spacer was placed on top of the aluminum cap and the loading head of the testing machine was fitted to the spacer.

The loading head has a curved surface on which a thin aluminum crush plate has been placed. This assists in obtaining a uniform load transfer between the loading piston and the loading head. All of the signal wires pass through a watertight box within the pressure chamber and then through the cell base to the instrument room.

Figure 61 is a close-up of an LVDT mounted across the saw-cut fracture plane. These LVDTs are designed to operate in water under a pressure environment and can measure displacements as small as 10^{-6} ft.

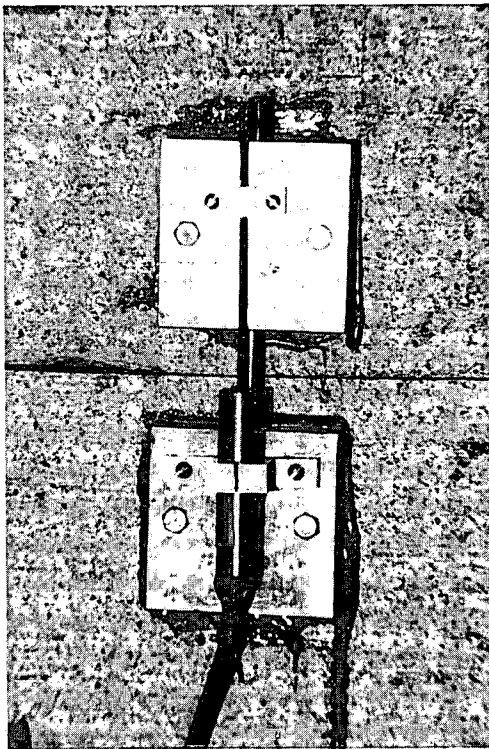


Figure 61. Close-up view of LVDT mounted across saw-cut fracture.

Figure 62 shows the core sample in place just before the pressure chamber is about to be lowered and bolted to the cell base. In the photograph, the 4-million pound loading frame is in the left background.

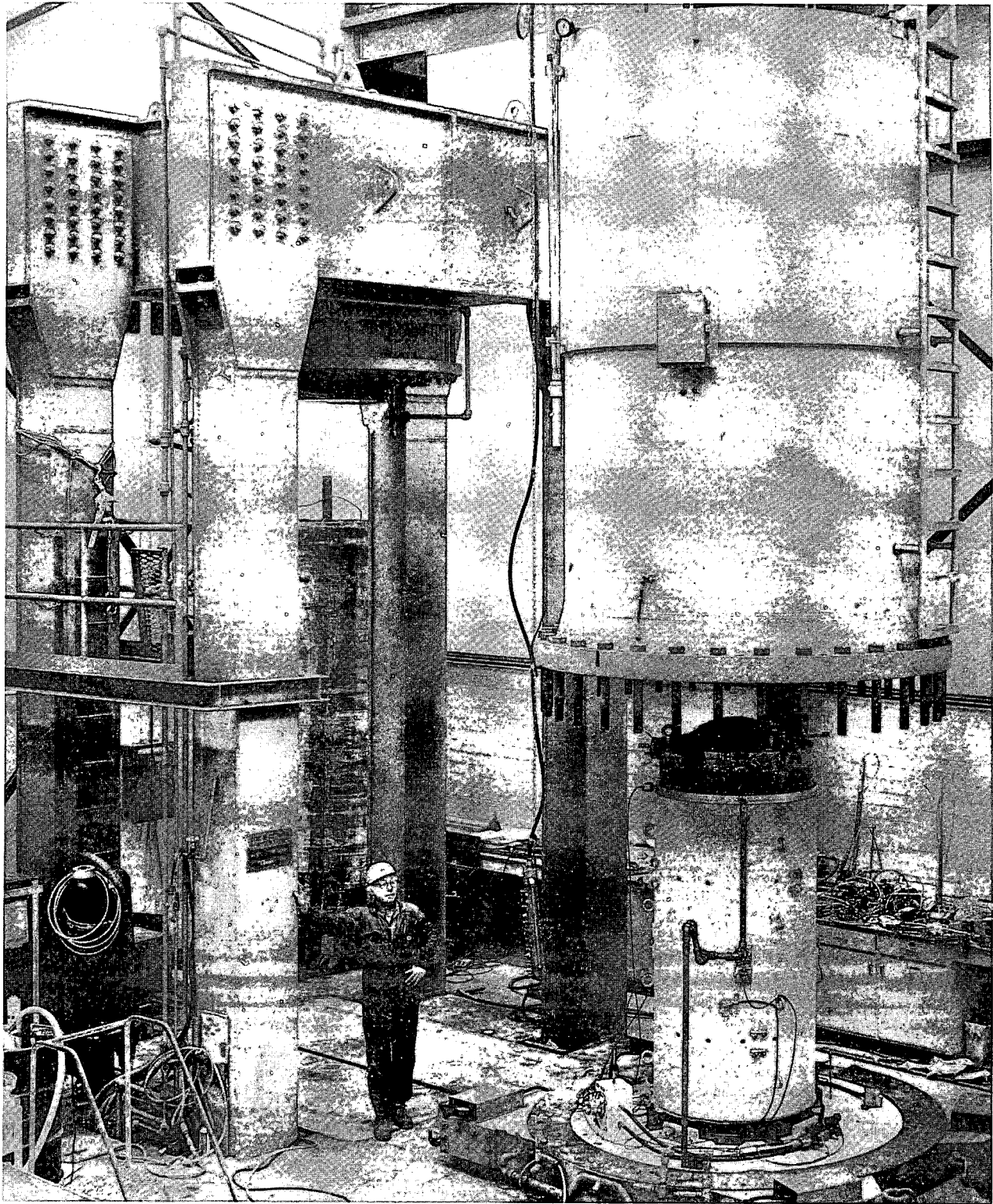


Figure 62. Large-diameter core ready for assembly in triaxial cell.

RESULTS OF FLUID INJECTION AND WITHDRAWAL TESTS

Three different kinds of fractures were investigated:

- (1) a "uniform" aperture represented by the saw-cut surface;
- (2) a "nonuniform" aperture produced by sandblasting a 14-in. circular area of the saw-cut surface (Fig. 63); and
- (3) a rough "tension" fracture surface produced by splitting the core.

The tension fracture was created by driving metal "feather" wedges into the 3/4-in. holes drilled around the perimeter of the core (Fig. 60). The saw-cut fracture was tested first, and then the sandblasted saw-cut surface was tested. The core was split, and the sandblasted saw-cut surface and the tension fracture were tested. Finally a rubber gasket was placed around the centre hole of the sandblasted surface enabling the tension fracture to be tested separately.

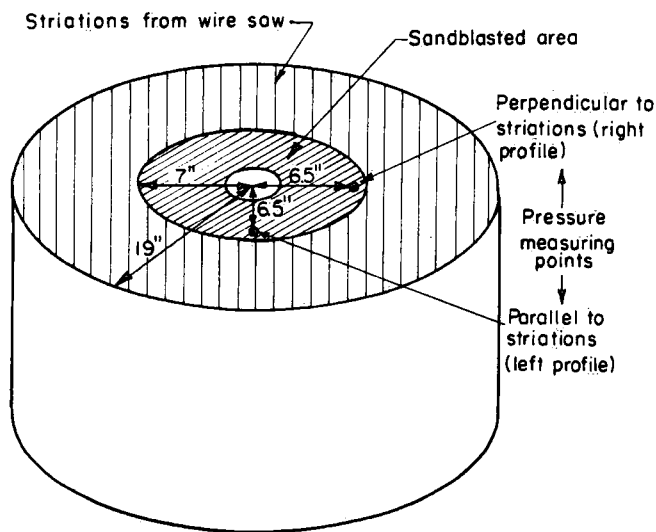


Figure 63. Schematic of sandblasted saw-cut fracture surface in nonuniform aperture.

With the instrumentation described above it was possible to measure the response of the fractures to different axial loads and changes in fluid pressures by measuring changes in aperture at the centre and at three points around the outside perimeter. For each fracture surface the change in flow rate and the change in fracture aperture were measured for different axial loads. In addition, for an axial stress of 200 psi and an external fluid pressure of 100 psi, the changes in flow rates and aperture were measured for different values of injection and withdrawal pressure in the centre borehole.

Cutting the core at the quarry produced fine striations on the saw-cut fracture surface. To determine whether these striations would produce anisotropy, in terms of flow

or pressure distribution, two small holes were drilled into the fracture plane at a distance of 6.5 in. from the centre of the injection hole (Fig. 63). These holes are oriented perpendicular and parallel to the striations. The fluid pressures were measured at these two points. Two similar holes were drilled into the plane of the tension fracture, in line with the two holes in the saw-cut fracture plane. Note that the centre borehole has a diameter of approximately 3.2 in.

Saw-cut Fracture Surface - "Uniform Aperture"

Figure 64 is a plot of axial stress versus average total displacement parallel to the axis measured with the four LVDTs placed across the saw-cut fracture surface. This displacement ($\delta_R + \Delta 2b$) is the sum of the change in fracture aperture ($\Delta 2b$) and the rock deformation (δ_R) parallel to the axis averaged over 4.75 in. - the average distance between points on opposite sides of the fracture plane to which the two components of the LVDTs were attached. The displacement over 4.75 in. owing to rock strain was calculated by using an average Young's modulus of 5.85×10^6 psi. The calculated δ_R was then subtracted from the total displacement measured ($\delta_R + \Delta 2b$) to give the average fracture deformation $\Delta 2b$.

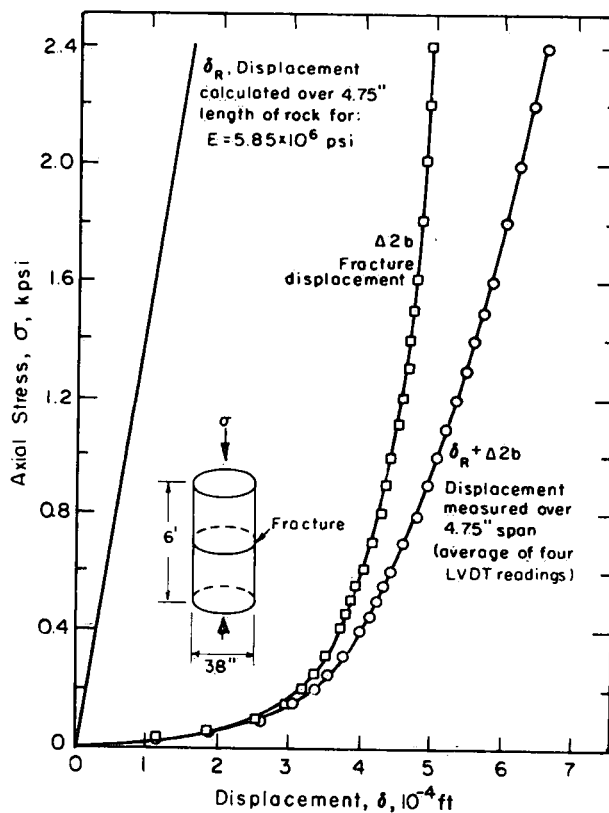


Figure 64. Fracture and rock deformation in saw-cut fracture surface.

The fracture displacement data in Figure 64 show the highly nonlinear nature of the normal force-normal displacement relationship for this fracture. The fracture almost reached a maximum closure condition for an axial stress of 600 psi. The greatest percentage of fracture closure occurred below an axial stress of 200 psi. Using the displacement produced by an axial stress of 200 psi, a K_N value of 9.0×10^7 psf/ft can be calculated. Because of the nonlinear nature of the force-displacement curve, no single K_N value can be used to characterize the curve.

Figure 65 presents the changes in flow rate and changes in fracture aperture as a function of effective stress ($\sigma_e = \sigma - P_2$). No attempt has been made to account for the changes in effective stress resulting from P_1 , the fluid pressure in the centre borehole, not being equal to P_2 , the fluid pressure surrounding the sample, during fluid injection and withdrawal. The changes in fracture aperture were measured at the centre borehole from a series of tests conducted over a period of several days. All of the flow rates were measured when the difference in fluid pressures ($\Delta P = P_1 - P_2$) was ± 40 psi.

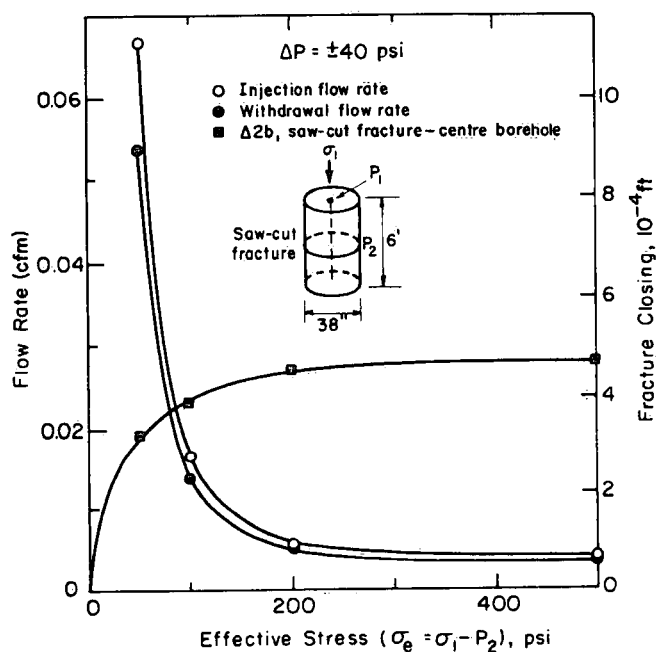


Figure 65. Change in flow rate and fracture aperture as a function of effective stress in saw-cut fracture surface.

The flow rates show a rapid decrease with increasing effective stress, approaching a minimum value at an effective stress of 200 psi. In addition, the difference between the flow rates during fluid injection and withdrawal is the greatest at the lowest effective stress levels. It should be noted that a ΔP value of ± 40 psi represents a greater percentage of the initial effective stress at the lower stress levels than at the higher stress levels. Thus one possible objective of ongoing research with the large rock cores would be to investigate this effective stress-flow rate relationship by maintaining effective stress constant while increasing axial stress and fluid pressure around the sample.

The changes in flow rate and fracture aperture for different injection and withdrawal pressures are given in Figure 66. These results are for a constant axial stress of 200 psi and an external fluid pressure of 100 psi. The clamp to which the LVDT was attached in the centre borehole was slightly unstable and thus this LVDT did not give reliable measurements of small changes in the fracture aperture. Therefore the changes in fracture aperture in Figure 66 are the averages of those measured by the three LVDTs around the sample perimeter.

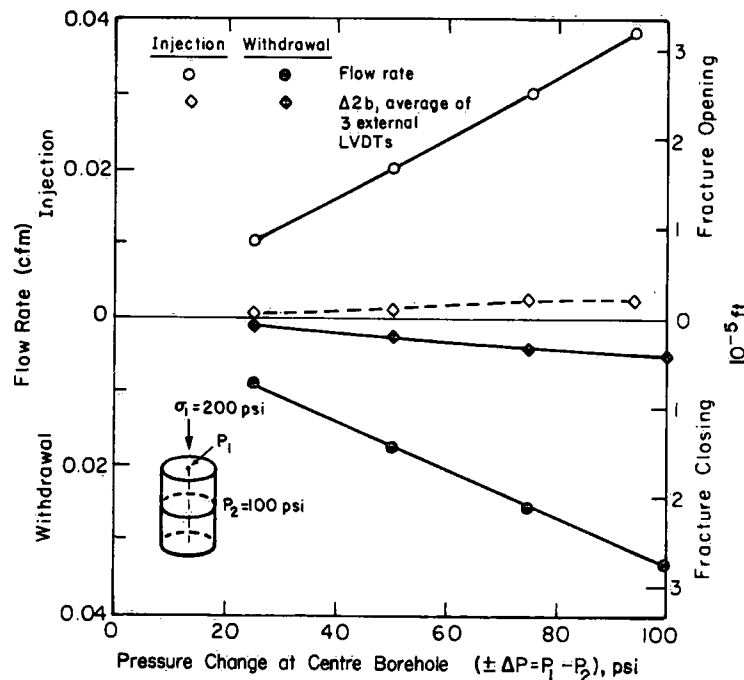


Figure 66. Changes in flow rate and fracture aperture for different injection and withdrawal pressures with a constant axial stress of 200 psi in saw-cut fracture surface.

Figure 67 presents the fluid pressures (P) measured along two radii at 5 in. from the edge of the borehole. These fluid pressures are presented as a percentage of the fluid pressure increase or decrease in the centre borehole, i.e., as $(P - P_2)/(P_1 - P_2) \times 100$. In this Figure, the greatest drop in fluid pressure occurs perpendicular to the striations in the fracture plane. Parallel to the striations or grooving, approximately 70% of the change in fluid pressure at the centre borehole has been dissipated over a distance of 5 in. (radius of borehole ≈ 1.6 in.). Perpendicular to the striations, approximately 95% of the change in fluid pressure at the centre borehole has been dissipated over the same radial distance. Thus flow in the saw-cut fracture is highly anisotropic. Also, because of the rapid changes of fluid pressure away from the borehole, very

little force was developed with which to deform the fracture. To develop greater forces, the saw-cut surface was sandblasted over a circular area 14 in. in diameter. This created a nonuniform aperture with the largest opening near the well.

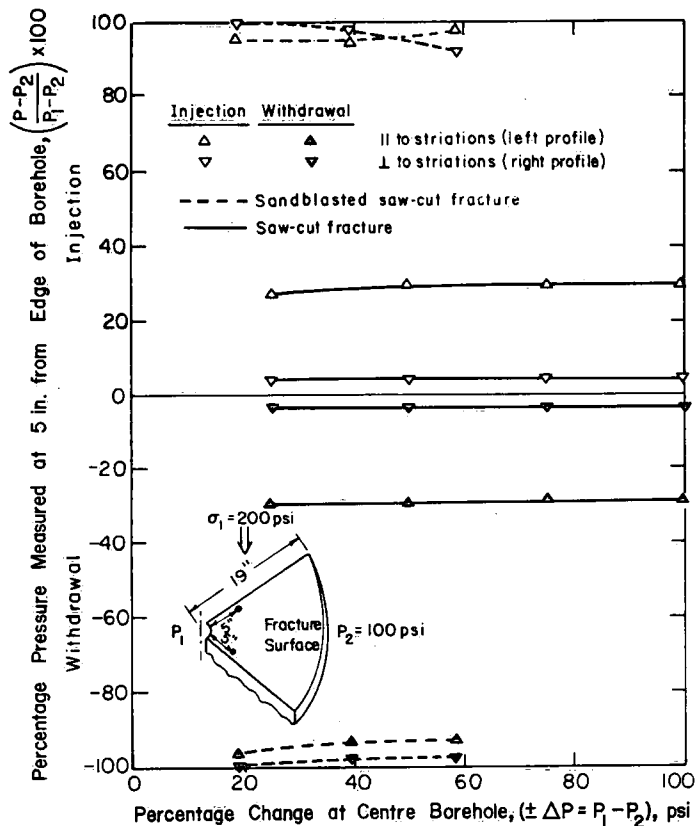


Figure 67. Percentage of pressure measured at 5 in. from edge of centre borehole for different injection and withdrawal pressures.

Saw-cut and Sandblasted Fracture Surface - "Nonuniform Aperture"

Figure 68 shows the force-normal displacement results for the saw-cut fracture after part of the fracture plane had been sandblasted (Fig. 63). This saw-cut and sandblasted surface is only slightly softer than the saw-cut surface itself. This difference may have been reduced by the repeated loadings during tests on the saw-cut fracture. For an axial stress of 200 psi, the K_N value is 8.66×10^7 psf/ft.

The flow rate and aperture changes for this "nonuniform" fracture aperture are given in Figure 69 as a function of effective stress. Although the changes in aperture are approximately the same as those measured for the saw-cut surface, the flow rates in this "nonuniform" aperture are from one to two orders of magnitude greater. In both fractures the flow rates approach a minimum value as the apertures approach a maximum closure value. This is undoubtedly the result of bridging owing to asperities in the fracture

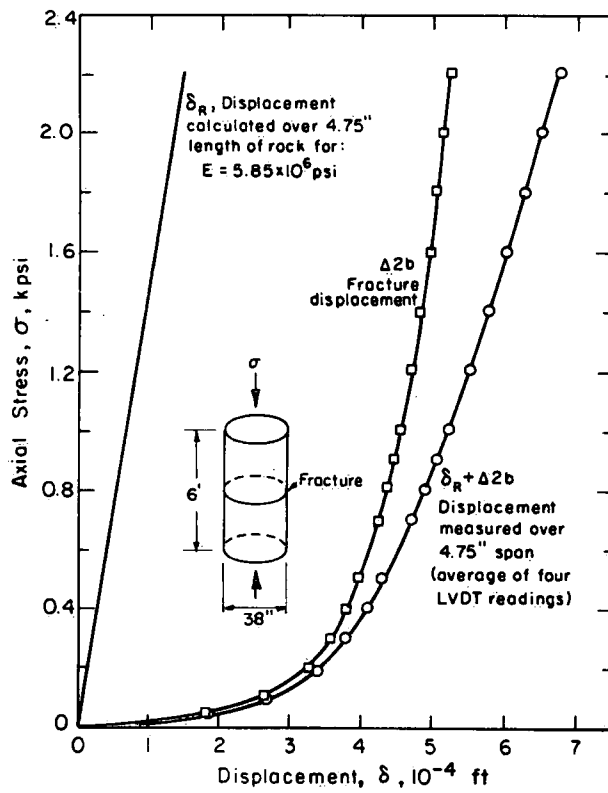
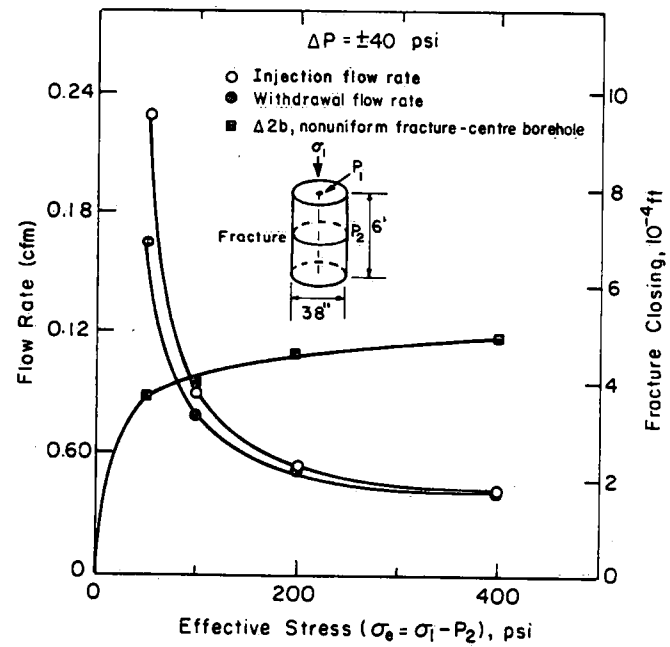


Figure 68. Fracture and rock deformation in sandblasted saw-cut surface.

Figure 69. Changes in flow rate and fracture aperture as a function of effective stress in sandblasted saw-cut fracture surface.



plane (grooving in this case). This bridging effect was observed by Pratt, Swolfs and Black during large-scale field tests on natural fractures. The changes in fracture aperture were measured at the centre borehole over a period of several days.

Figure 70 shows the flow rates and the corresponding changes in fracture aperture for three different injection and withdrawal pressures. The axial stress was kept constant at 200 psi and the external fluid pressure was maintained at 100 psi. There is a considerable difference in the injection and withdrawal rates for equivalent fluid pressure gradients. The changes in fracture aperture shown are the averages of the three external LVDT readings. The centre LVDT holding device was not corrected until both the "nonuniform" and the tension fracture were tested. Although the changes in aperture are small, they do show the fracture opening during injection and closing during withdrawal.

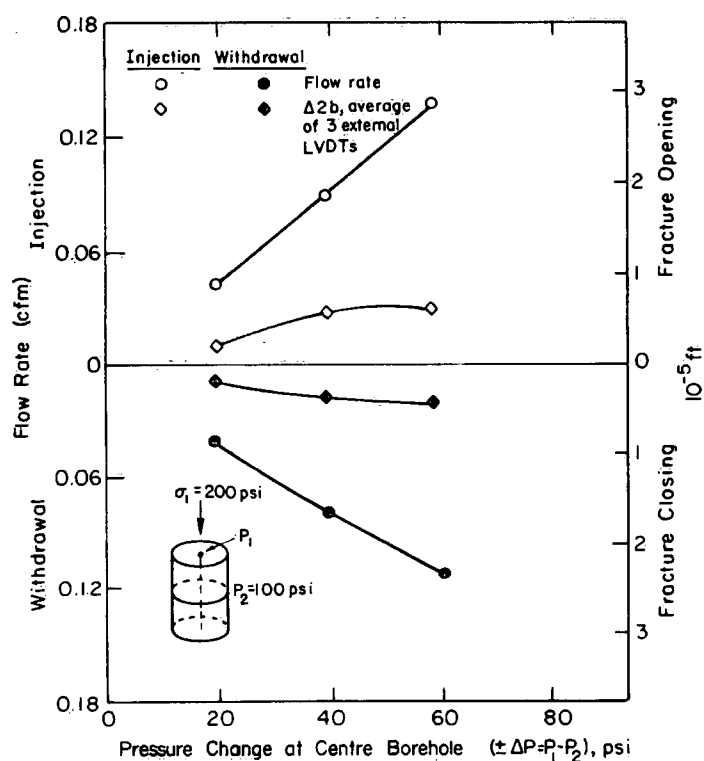


Figure 70. Changes in flow rate and fracture aperture for different injection and withdrawal pressures with a constant axial stress of 200 psi in sandblasted saw-cut surface.

The percentage of the injection and withdrawal pressure measured at 5 in. from the edge of the borehole for the different changes in fluid pressure is given in Figure 67. These fluid pressures indicate that the sandblasting did create a "nonuniform" fracture aperture, since more than 90% of the injection or withdrawal pressures are measured at 5 in. from the edge of the borehole.

Tension Fracture and Nonuniform Fracture

The core was split perpendicular to its axis by driving wedges into the 3-in. deep holes drilled 8 in. to 10 in. apart around the surface of the core. Figure 71 indicates the rough nature of the tension fracture surface. The metal guides allowed the two surfaces to be properly rematched.

It should be noted that for these last two remaining tests the LVDT holders in the centre borehole were replaced. Expansion rings were glued to the borehole walls with the LVDTs clamped to the centre of the rings. This configuration enabled stable and consistent measurements of displacement normal to the fracture surface.

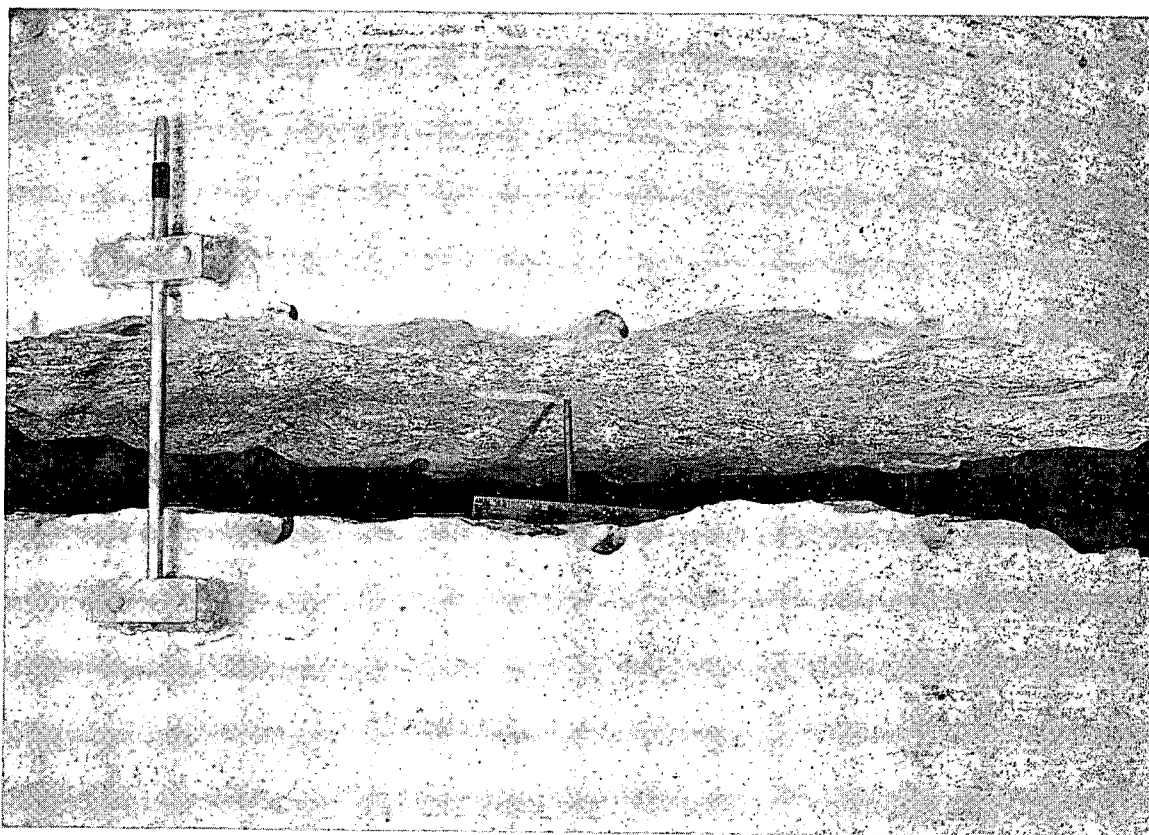


Figure 71. Tension fracture. Note the 6-in. scale resting on the fracture surface.

The fracture displacement data in Figure 72 show the highly deformable nature of the tension fracture. The measurements were made during the first loading cycle and the displacements measured for an axial stress of 200 psi give a K_N value of 3.7×10^7 psf/ft.

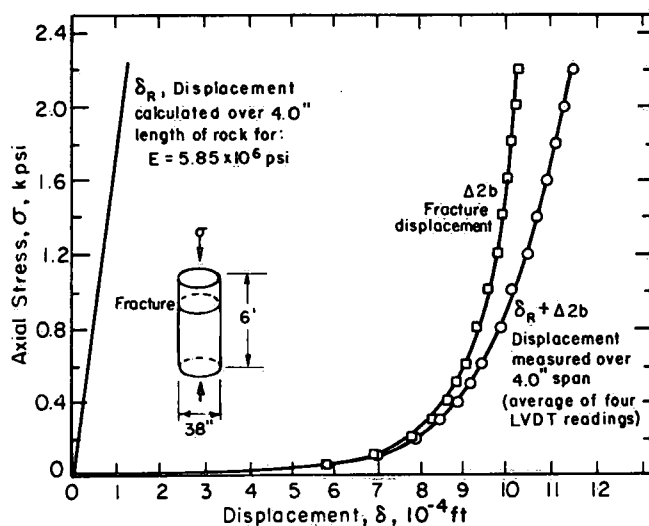


Figure 72. Fracture and rock deformation in tension fracture.

Figure 73 shows the total flow rates through both the tension fracture and the "nonuniform" fracture and the change in each aperture for different levels of effective stress. These measurements were made after several loading cycles, and nonrecoverable deformation with repeated loadings may account for the differences in the fracture closure being considerably less than those shown by the force-displacement curves (Figs. 68 and 72). Figure 74 presents the flow rates and changes in fracture aperture for four different injection and withdrawal pressures. The axial stress was held constant at 200 psi and the external pressure was fixed at 100 psi. The aperture changes were measured at the centre borehole. These aperture changes show that the nonuniform fracture opened during injection and closed during withdrawal, while the tension fracture showed a small closure during injection as well as during withdrawal. For qualitative comparison of the magnitude of the aperture change measured during this test with the changes measured during the previous two tests, the average displacement as measured at the three external LVDTs has been plotted for the nonuniform fracture.

The fracture displacement pattern observed during this test is consistent with the changes in fluid pressures observed 5 in. from the edge of the borehole in both fractures (Fig. 75). For example, there was a slight increase in the percentage of fluid pressure measured 5 in. from the well in the nonuniform aperture as the injection pressure was increased from 20 psi to 40 psi. In the tension fracture there was a slight decrease in the percentage of fluid pressure measured. An increase in the percentage of fluid pressure is consistent with fracture opening and a decrease is consistent with fracture

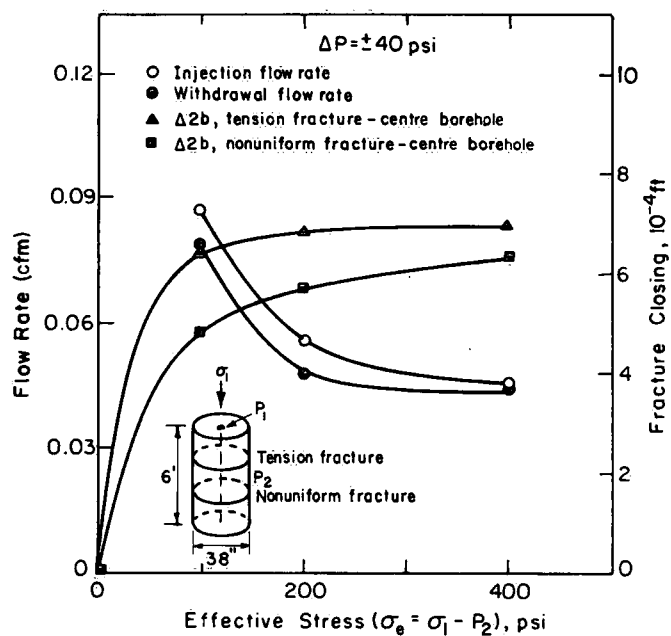
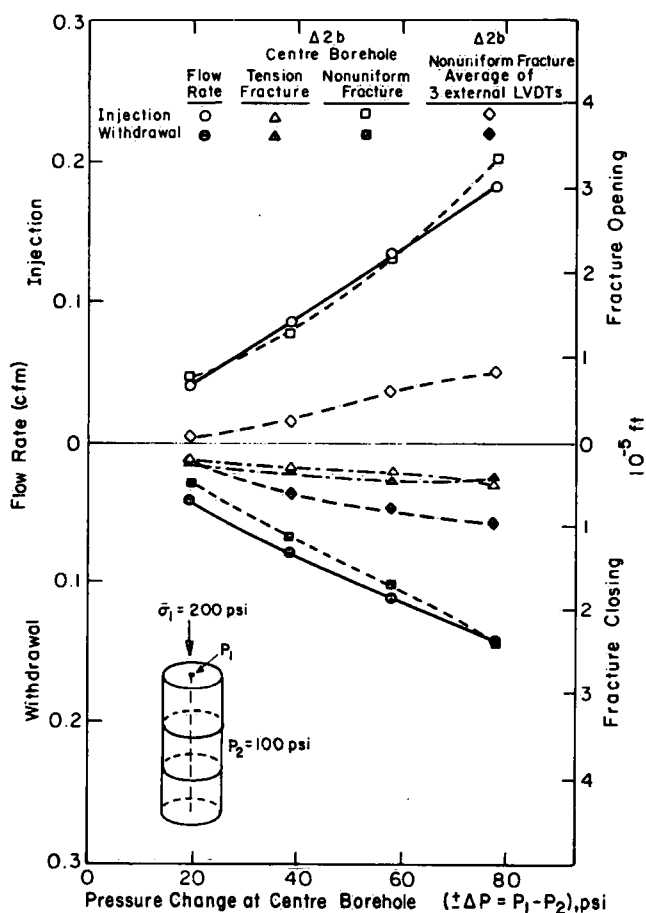


Figure 73. Changes in flow rate and fracture aperture as a function of effective stress in both tension and sandblasted saw-cut fractures.

Figure 74. Changes in flow rate and fracture aperture for different injection and withdrawal pressures with a constant axial stress of 200 psi in tension fracture and sandblasted saw-cut fracture.



closing (Chapter 3). The sudden decrease in the percentage of fluid pressure measured in the fracture plane when the injection pressure was increased to 60 psi suggests the onset of turbulent flow. The sandblasted part of the fracture plane near the well bore is quite rough and Reynolds numbers were calculated to be greater than 100 near the borehole. The fluid pressure in the tension fracture plane suggests a decrease in the rate of fracture closure when the injection pressure is greater than 60 psi. This would be consistent with the reduction in the percentage of fluid pressure measured in the "nonuniform" fracture plane for these higher injection pressures.

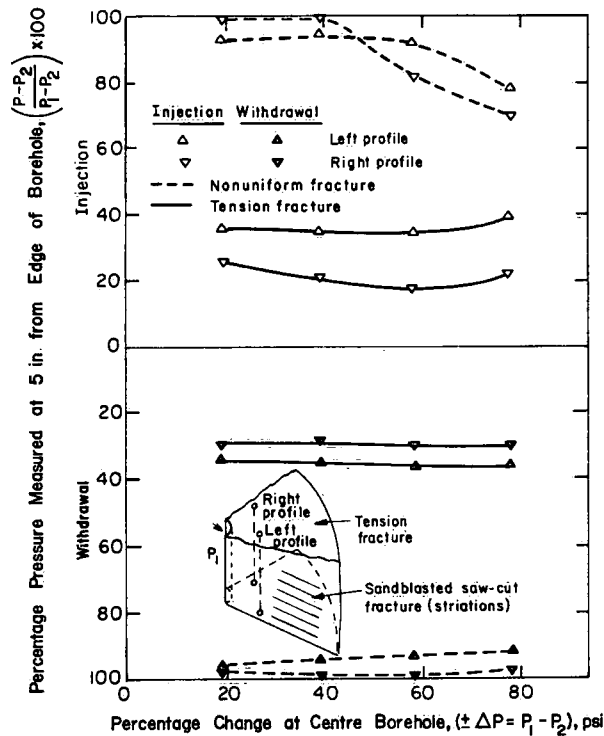


Figure 75. Percentage of pressure measured at 5 in. from edge of centre borehole for different injection and withdrawal pressures.

Tension Fracture

A rubber gasket, 2 in. wide and 3/16 in. thick, was placed around the centre borehole in the plane of the sandblasted saw-cut fracture so that the tension fracture could be observed separately. Because of the stiffness of the rubber and the thickness of the rubber gasket, all of the effective stresses were transmitted across the saw-cut fracture through the rubber gasket. This resulted in a very high and complex pattern of stresses around the centre borehole. Thus the results presented for the tension fracture are dominated by this stress pattern and are only presented to give the order of magnitude of the flow rates in the tension fracture.

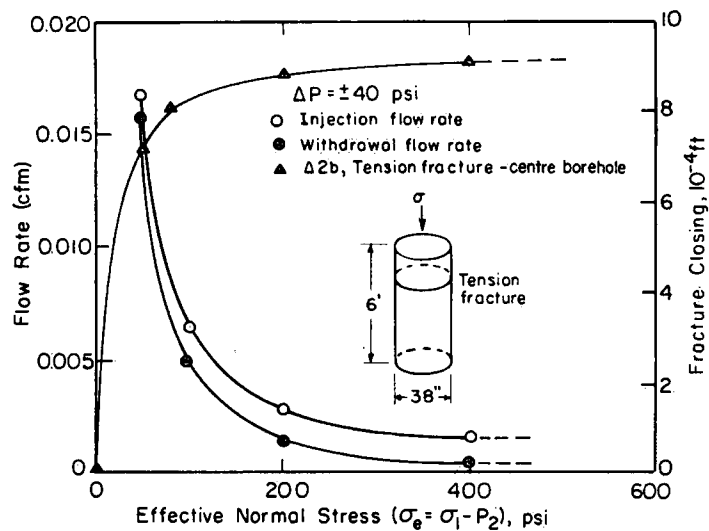


Figure 76. Change in flow rate and fracture aperture as a function of effective stress in tension fracture only.

Figure 77. Changes in flow rate and fracture aperture for different injection and withdrawal pressures and a constant axial stress of 200 psi in tension fracture only.

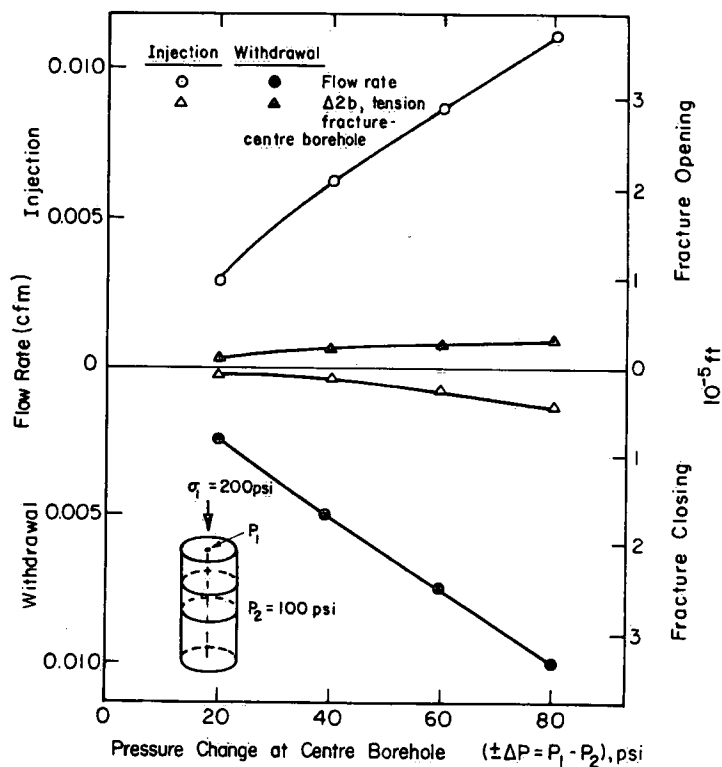


Figure 76 shows the flow rates and fracture closure as a function of effective stress. For an axial stress of 200 psi and an external fluid pressure of 100 psi, the flow rates and changes in aperture for different injection and withdrawal pressures are presented in Figure 77. The percentage of fluid pressure in the tension fracture plane for the same injection and withdrawal pressures is given in Figure 78.

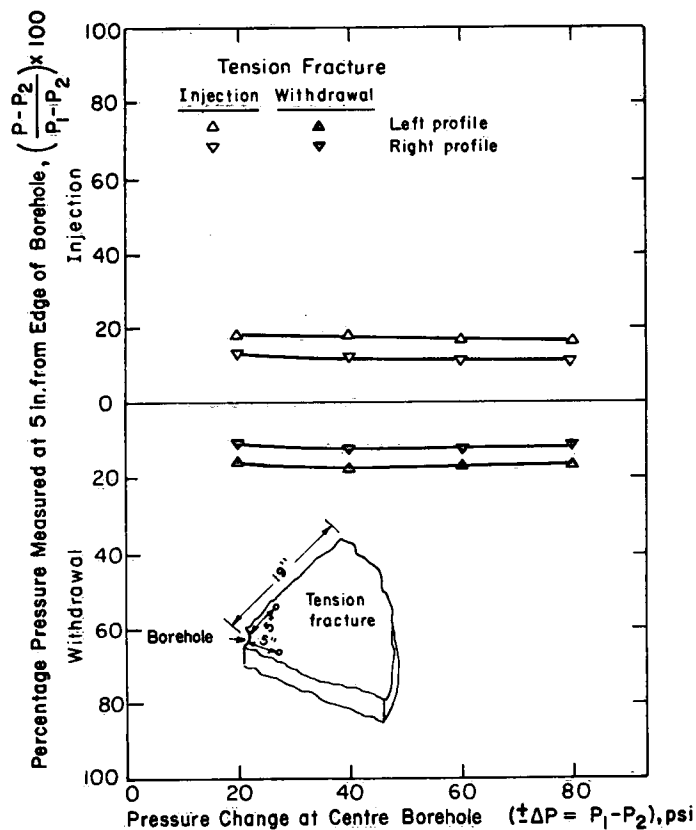


Figure 78. Percentage of pressure measured at 5 in. from edge of centre borehole for different injection and withdrawal pressures.

Figure 77 shows that the tension fracture closed during fluid injection as a result of the stresses owing to the rubber gasket. Figure 78 indicates that the percentage of the injection pressure measured in the fracture plane decreases slightly. This change in fluid pressures is consistent with the measured fracture closing. The overall fluid pressures during fluid withdrawal do not have a similar consistent pattern.

SUMMARY

Results from this series of laboratory tests demonstrate that measurable changes of fracture aperture do occur owing to changes of fluid pressure within the fracture plane. In addition, changes of fluid pressure within the plane of one fracture can affect the fluid pressures in an adjacent fracture by changing the fracture aperture. The relative

distribution of fluid pressures within each fracture plane determines which fracture will open or close at the expense of the nearby fractures. If the fractures have uniform apertures, then very little deformation occurs. As the aperture becomes more nonuniform the fluid pressures are propagated over a greater distance and hence the larger forces produce greater deformations.

The measured flow rates reflect a considerable difference between injection and withdrawal in the same fracture system. The flow rates show a rapid decrease with increasing effective stress. Also the difference between the injection and withdrawal flow rates decreases with increasing effective stress.

The fluid pressure distribution in the fracture plane, when expressed as a percentage of the injection or withdrawal pressure, is very sensitive to changes in aperture and deviations from laminar flow. Thus, by observing the fluid pressures in individual fractures around a pumping well, one should be able to determine which fractures are opening or closing.

The aperture changes measured in the laboratory were almost an order of magnitude less than those measured in the field. This is partly the result of the artificial fractures being stiffer. As well, the laboratory tests were conducted with higher initial effective stresses than those acting in the field situation. Also, fluid pressures were acting over a much greater area of the fracture surface in the field than in the laboratory.

Neither the flow rates nor the aperture changes showed a distinct nonlinear relationship to the fluid pressures during laboratory tests. This agrees with the field observations and shows that fractures deform under small changes in fluid pressure and that it is not necessary to have fluid pressure approaching overburden stress before the fractures open.

Summary and Conclusions

The mathematical approach used in this investigation shows the effectiveness of the Galerkin method in arriving at a finite-element formulation directly from the governing equations without having to obtain and prove the existence of an appropriate variational principle. The numerical model presented in Chapter 2 is a powerful tool for analyzing the interaction between rock stresses and fluid pressures in deformable fractured rock masses.

Investigation of idealized fracture systems shows that in deformable systems there is a considerable difference in the flow rates and pressure distributions resulting from fluid injection and withdrawal. This difference is highly dependent on the deformability of the fractures and the magnitude of the fluid pressure changes relative to the magnitude of the initial effective stress. A fracture opening during injection allows the fluid pressure to propagate greater distances, whereas a fracture closing during withdrawal tends to reduce the area over which the initial fluid pressures are affected. Comparison of equivalent uniform fracture apertures with corresponding nonuniform apertures indicates that in deformable systems there is a considerable difference in the flow rates and the pressure distributions in the two systems. This difference in pressure distribution results in greater fracture deformations in the nonuniform fracture system. Thus, on a local scale, fractures having nonuniform apertures cannot be replaced with fractures having equivalent uniform apertures. These observations have a considerable bearing on attempts to determine how the stability of fractured rock slopes is affected by fluid pressures or how effective a particular drainage system would be in stabilizing a given rock slope.

The numerical model results clearly demonstrate that changes in the effective stress resulting from drawdown in a well can cause a significant decrease in the permeability of the fracture system.

Results from injection tests during the field investigation show that changes in fracture aperture were indicated by changes in the shape of the fluid pressure profile as measured in nearby observation wells. In addition, measuring fluid pressure at several points away from the injection well enables the calculation of the variation in fracture aperture. The amount of detail obtained is limited to the number of available observation wells.

In most low-capacity wells, such as those usually found in fractured-rock aquifers, it is extremely important that the well discharge be kept at a constant rate during a pump test. A constant-head discharge control tank (Gale and Welhan, 1975c) was a much-needed piece of equipment for controlling well discharge during this study. Knowledge of the permeability profile of a well was an important prerequisite to the analysis of drawdown data. The modification of the inflatable packer assembly described in the Appendix should provide a simple and inexpensive tool for measuring the relative permeability profile of wells completed in fractured rock aquifers. With data obtained using both of the above tools, one should be able to determine the effect that fracture deformation and the resulting change in fracture permeability have on drawdown during pump tests. Collection of such data is a necessary step in improving methods of analyzing pump test data from fractured rock aquifers.

The "fracture deformation gauge" developed during the field investigation provides a means of measuring *in situ* changes in fracture aperture. Using this instrument, fracture closure of the order of 5×10^{-5} ft was measured for a reduction in fluid pressure of approximately 7.5 psi. Fracture openings of approximately 3×10^{-4} ft were measured for fluid pressure increases of approximately 20 psi. All of the field measurements of fracture deformation were obtained on fractures located within 30 ft of the ground surface. These measurements show that fracture deformation does occur as a result of changes in fluid pressures and is a significant percentage of the initial fracture apertures that are calculated from injection test results. In addition, when a number of fractures intersect a well, the field measurements demonstrate that the relative fluid pressure distribution within the fracture plane results in a preferential opening of some of the fractures. The fluid pressure distribution is directly related to the variation in fracture aperture away from the injection well. Also, the field results demonstrate that fractures open or close under very small changes in fluid pressure and thus fluid pressures approaching overburden stress are not necessary before fracture deformation occurs.

Very good agreement was attained between the field measurements of fracture deformation and the deformation calculated using a numerical model of the fracture system at the Sambro test site. The normal stiffness values for the fractures were calculated from the field measurements of changes in fracture aperture and the corresponding changes in fluid pressures. Thus this approach provides a method for obtaining *in situ* measures of the normal stiffness that should be more representative than those values determined from small samples in the laboratory. In addition, comparison of the field and the numerical model results demonstrates the shortcomings of the straight-line approximation to the K_N values that is the basis of the stiffness perturbation method used to model the force-displacement characteristics of fractures. The straight-line approach does not permit accurate modelling of the nonlinear nature of the fracture deformation, especially when the

change in effective stress is a significant percentage of the initial effective stress. A constitutive relationship that follows the real force-displacement curve would give better results when comparing field or laboratory data with numerical model results.

The numerical results presented in Chapter 4 demonstrate the importance of determining the permeability profile of a well. The dominating effect of the larger fractures is clearly shown by these somewhat idealized examples.

Results obtained from the laboratory tests with the large-diameter rock core agree with the pattern of fracture deformation observed in the field as well as with that predicted using the numerical model. The laboratory results presented in Chapter 5 show aperture changes in the order of 10^{-5} ft. It should be noted that initial effective stresses during these tests were approximately five times greater than those present during the field tests and that the fractures were stiffer. The laboratory results clearly demonstrate the decrease in flow rate with an increase in effective stress and the increase in the difference between injection and withdrawal flow rates with an increase in fluid pressures.

The laboratory results also point out the importance of aperture uniformity on fracture deformation. The laboratory tests show that fluid pressure profiles within the fracture plane are very sensitive to changes in fracture aperture. Thus, by measuring fluid pressures at several points within a fracture plane and comparing the fluid pressure profiles, one should be able to determine whether the fractures are opening or closing during field injection and withdrawal tests.

This study has been concerned only with steady-state events. It is obvious that an investigation of transient effects in deformable fracture systems, especially in porous fractured rocks, would contribute significantly to an understanding of well behaviour in fractured rock aquifers. It is hoped that the field instrumentation and data and the laboratory and numerical model results presented in this report will provide some additional aids and insights to future extensions of this work.

References

- Barenblatt, G., U.P. Zheltov and G.H. Kochina. 1960. Basic concepts in the theory of seepage of homogeneous liquids in fractured rocks. *Prikl. Mat. Mekh.* 24:852-864. In Russian.
- Bear, J. 1972. *Dynamics of Fluids in Porous Media*. New York: American Elsevier Publishing Co.
- Becker, E., C.K. Chan and H.B. Seed. 1972. Strength and Deformation Characteristics of Rockfill Materials in Plane Strain and Triaxial Compression Tests. *Geotechnical Engineering Report No. 72-3*, University of California, Berkeley.
- Benko, K.F. 1966. Instrumentation in rock grouting for Portage Mountain Dam. *Water Power* 18(10):407-414.
- Bernaix, J. 1967. *Étude géotechnique de la roche de Malpasset*. Paris, Dunod, p. 215.
- Bianchi, L. and D.T. Snow. 1968. Permeability of crystalline rock interpreted from measured orientations and apertures of fractures. *Ann. Arid Zone* 8(2):231-245.
- Biot, M.A. 1940. General theory of three-dimensional consolidation. *J. Appl. Phys.* 12:155-164.
- Daniel, E.J. 1954. Fractured reservoirs of the Middle East. *Bull. Am. Assoc. Petrol. Geol.* 38(5):774-815.
- Davis, S.N. and G.W. Moore. 1965. Semidiurnal movement along a bedrock joint in Wool Hollow Cave, California. *Bull. Nat. Speleol. Soc.* 27(4):133-142.
- Davis, S.N., F.L. Peterson and A.D. Halderman. 1969. Measurement of small surface displacements induced by fluid flow. *Water Resources Res.* 5(1):129-138.
- Desai, C.S. and J.F. Abel. 1972. *Introduction to the Finite Element Method*. New York: Van Nostrand Reinhold Ltd.

- Douglas, J. and T. Dupont. 1970. Galerkin methods for parabolic equations. *J. Numer. Anal.*, SIAM 7(4):575-626.
- Duguid, J.O. 1973. Flow in fractured porous media. Ph. D. Thesis, Princeton University.
- Evans, D.M. 1966. The Denver area earthquakes and the Rocky Mountain Arsenal well. *M. Geol.* 3(1).
- Faribault, E.R. 1907. *Geology of Halifax County, Prospect Sheet No. 69.* Geological Survey of Canada.
- Finlayson, B.A. 1972. *The Method of Weighted Residuals and Variational Principles.* New York: Academic Press.
- Gale, J.E. and J.A. Welhan. 1975a. Development and use of an instrument for measuring *in situ* changes of fracture aperture. In Research Program, Hydrology Research Division - Summaries of Progress and Short Research Reports, Inland Waters Directorate, *Report Series No. 42*, pp. 17-21.
- Gale, J.E. and J.A. Welhan. 1975b. Construction of a simple inflatable packer for use in shallow wells. Inland Waters Directorate, *Report Series No. 42*, pp. 22-25.
- Gale, J.E. and J.A. Welhan. 1975c. Controlling well discharge with a constant head tank. Inland Waters Directorate, *Report Series No. 42*, pp. 26-29.
- Ghaboussi, J., E.L. Wilson and J. Isenberg. 1973. Finite element for rock joints and interfaces. *J. Soil Mech. Foundation Div.*, ASCE 99(SM10):833-848.
- Goodman, R.E. 1970. The deformability of joints. *Determination of the In Situ Modulus of Deformation of Rock*, ASTM STP 477, American Society for Testing and Materials, pp. 174-196.
- Goodman, R.E. 1974. The mechanical properties of joints. *Proc. 3rd Congress of the Int. Soc. of Rock Mechanics*, Vol. 1, pp. 127-140.
- Goodman, R.E. and J. Dubois. 1972. Duplication of dilatancy of jointed rocks. *J. Soil Mech. Foundation Div.*, ASCE 98(SM4):399-422.
- Goodman, R.E., R.L. Taylor and T. Brekke. 1968. A model for the mechanics of jointed rock. *J. Soil Mech. Foundation Div.*, ASCE 94(SM3):637-659.

- Gringarten, A.C. and P.A. Witherspoon. 1972. A method of analyzing pump test data from fractured aquifers. *Proc. Symp. of Int. Soc. of Rock Mechanics*, Percolation through Fissured Rock, Stuttgart, p. T2-C.
- Hantush, M.S. 1966. Wells in homogeneous anisotropic aquifers. *Water Resources Res.* 2(2):273-279.
- Hantush, M.S. and R.G. Thomas. 1966. A method for analyzing a drawdown test in anisotropic aquifers. *Water Resources Res.* 2(2):281-286.
- Helm, D.C. 1974. Evaluation of stress-dependent aquitard parameters by simulating observed compaction from known stress history. Ph. D. Thesis, University of California, Berkeley.
- Heuzé, F., R.E. Goodman and A. Borenstein. 1971. Joint perturbation and no tension solution. *Rock Mech. J., ISRM* 2(5).
- Hodgson, R.A. 1961a. Regional study of jointing in Comb Ridge, Navajo Mountain area, Arizona and Utah. *Bull. Am. Assoc. Petrol. Geol.* 45(1):1-38.
- Hodgson, R.A. 1961b. Classification of structures on joint surfaces. *Am. J. Sci.* 259(7):493-502.
- Hutton, S.G. and D.L. Anderson. 1971. Finite element method: A Galerkin approach. *J. Eng. Mech. Div., ASCE* 97(EM5):1503-1520.
- John, K.W. 1969. Civil engineering approach to evaluate strength and deformability of regularly jointed rock. *Proc. 11th Symp. on Rock Mechanics*, Rock Mechanics - Theory and Practice, edited by W.H. Somerton, Soc. Min. Eng., Berkeley, California.
- Jouanna, P. 1972. Effet des sollicitations mécaniques sur les écoulements dans certains milieux fissurés. Thèse, Docteur ES-Sciences Physiques, Université de Toulouse, France.
- Kantorovich, L.A. and V.D. Krylov. 1958. *Approximate Methods of Higher Analysis*. New York: Interscience.
- Karanjac, J. 1971. Elastic storage in aquifers. Ph.D. Thesis, Princeton University.
- Kazemi, H. 1969. Pressure transient analysis of naturally fractured reservoirs with uniform fracture distribution. *Soc. Petrol. Eng. J.* 9(4):451-462.

- Kazemi, H., M.S. Seth and G.W. Thomas. 1969. The interpretation of interference tests in naturally fractured reservoirs with uniform fracture distribution. *Soc. Petrol. Eng. J.* 9(4):463.
- Király, L. 1969. Statistical analysis of fractures (orientation and density). *Sonderdruck aus der Geologischen Rundschau* 59(1):125-151.
- Law, J. 1944. Statistical approach to the interstitial heterogeneity of sand reservoirs. *Trans. Am. Inst. Min. Met. Eng.* 155:202.
- Lewis, D.C. and R.H. Burgoyne. 1964. Hydraulic characteristics of fractured and jointed rock. *Ground Water* 2(3):4-9.
- Lomize, G.M. 1951. *Flow in Fractured Rocks*. All-Union Energetics Publishers, Moscow/Leningrad, pp. 7-127.
- Louis, C. September 1969. A Study of Groundwater Flow in Jointed Rock and its Influence on the Stability of Rock Masses. *Rock Mechanics Research Report No. 10*, Imperial College of Science and Technology, University of London.
- Louis, C. 1974. Introduction. In *Hydraulique des roches*, Publication, Bureau de recherches géologiques et minières, Orléans, France.
- Louis, C. and Y.N. Maini. 1970. Determination of *in situ* hydraulic parameters in jointed rock. *Proc. 2nd Congress of Int. Soc. of Rock Mechanics*, Belgrade, pp. 1-32.
- Louis, C. and M. Pernot. 1972. Three-dimensional investigation of flow conditions of Grand Maison Dam site. *Proc. Symp. of Int. Soc. of Rock Mechanics*, Percolation through Fissured Rocks, Stuttgart.
- MacDougall, J.I., D.B. Cann and J.D. Hilchey. 1963. Soil Survey of Halifax County, Nova Scotia. *Report No. 13*, Nova Scotia Soil Survey, Truro, Nova Scotia.
- Mahtab, M.A. *et al.* 1972. Analysis of Fracture Orientations for Input to Structural Models of Discontinuous Rock. United States Department of the Interior, Bureau of Mines Report Investigation No. 7669.
- Maini, Y.N.T. 1971. *In situ* hydraulic parameters in jointed rock - their measurement and interpretation. Ph.D. Thesis, Imperial College, University of London.

- Mikhlin, S.G. 1964. *Variational Methods in Mathematical Physics*. New York: Macmillan Co.
- Morgenstern, N.R. and H. Guther. 1972. Seepage into an excavation in a medium possessing stress-dependent permeability. *Proc. Symp. of Int. Soc. of Rock Mechanics*, Percolation through Fissured Rocks, Stuttgart, p. T2-C.
- Muskat, M. 1946. *The Flow of Homogeneous Fluids through Porous Media*. Ann Arbor, Michigan: J.W. Edwards, Inc.
- Noorishad, J., P.A. Witherspoon and T.L. Brekke. 1971. A Method for Coupled Stress and Flow Analysis of Fractured Rock Masses. *Geotechnical Engineering Publication No. 71-6*, University of California, Berkeley.
- Ohnishi, Y. 1973. Laboratory measurement of induced water pressures in jointed rocks. Ph.D. Thesis, University of California, Berkeley.
- Ohnishi, Y. and R.E. Goodman. 1974. Results of laboratory tests on water pressure and flow in joints. *Proc. 3rd Congress of the Int. Soc. of Rock Mechanics*, Vol. II-A, pp. 660-666.
- Papadopoulos, I.S. 1967. Nonsteady flow to a well in an infinite anisotropic aquifer. *Proc. Dubrovnik Symp. on Hydrology of Fractured Rocks*, Vol. 1, No. 73, IASH.
- Parizek, R. and S.H. Siddiqui. 1970. Determining the sustained yield of wells in carbonate and fractured aquifers. *Ground Water* 8(5).
- Parsons, M.L. 1972. Determination of hydrogeological properties of fissured rocks. *Proc. 24th Geol. Congress, Montreal, Section II, Hydrogeology*, pp. 89-99.
- Parsons, R.W. 1966. Permeability of Idealized Fractured Rock. *Am. Inst. Min. Met. Eng.*, Paper No. 1289.
- Polubarinova-Kochina, P. Ya. 1962. *Theory of Groundwater Movement*. Translated by R.J.M. De Wiest. Princeton: Princeton University Press.
- Pratt, H.R., H.S. Swolfs and A.D. Black. 1974. Properties of *In Situ* Jointed Rock. *Final Technical Report No. TR54-57*, Terratek, Salt Lake City, Utah. Submitted to Environmental Sciences Division, United States Army Research Office, Durham, North Carolina, Contract No. DAH C04 72 C 0049.

- Rayneau, C. 1972. Contribution à l'étude des écoulements autour d'un forage en milieu fissuré. Thèse, Docteur-Ingénieur Université des Sciences et Technique du Languedoc, Académie de Montpellier, France.
- Rodatz, W. and W. Wittke. 1972. Wechselwirkung Zwischen Deformation und Durchströmung un Klüftigen, Anisotropen Gebirge. *Proc. Symp. of Int. Soc. of Rock Mechanics*, Percolation through Fissured Rock, Stuttgart, p. T2-1.
- Rofail, N. 1967. Analysis of pumping tests in fractured rocks. *Proc. Dubrovnik Symp. on Hydrology of Fractured Rocks*, Vol. 1, No. 73, IASH.
- Romm, E.S. and B.V. Pozinenko. 1963. Investigation of seepage in fractured rocks. *Tr. Vnigri*, No. 214, Leningrad. In Russian.
- Sarda, J.P., P. Le Tirant and G. Baron. 1974. Influence des contraintes et de la pression de fluide sur l'écoulement dans les roches fissurées. *Proc. 3rd Congress of Int. Soc. of Rock Mechanics*, Vol. II-A, pp. 667-673.
- Serafim, T.L. 1968. Influence of interstitial water on the behaviour of rock masses. In *Rock Mechanics in Engineering Practice*, edited by K.G. Stagg and O.C. Zienkiewicz. New York: John Wiley and Sons.
- Sharp, J.C. 1970. Fluid flow through fissured media. Ph.D. Thesis, Imperial College of Science and Technology, University of London.
- Shehata, W.M. 1971. Geohydrology of Mount Vernon Canyon area, Jefferson County, Colorado. Ph.D. Thesis, Colorado School of Mines, Golden, Colorado.
- Smitheringale, W.G. 1960. Geology of Nictaux-Torbrook Map Area, Annapolis and Kings Counties, Nova Scotia. Geological Survey of Canada, Paper 60-13.
- Snow, D.T. 1965. A parallel plate model of fractured permeable media. Unpublished Ph.D. Dissertation, University of California, Berkeley.
- Snow, D.T. 1966. Threshold pressure test for anisotropic foundation permeability. *Felsmech. Ingenieurgeol.* 4:298.
- Snow, D.T. 1968a. Fracture deformation and changes of permeability and storage upon changes of fluid pressure. *Quart. Colo. Sch. Mines* 63(1):201.
- Snow D.T. 1968b. Rock fracture spacings, openings, and porosities. *J. Soil Mech. Foundation Div., ASCE* 94(1):73-91.

- Snow, D.T. 1969. The frequency and apertures of fractures in rocks. *Int. J. Rock Mech. Min. Sci.* 6(4):23-40.
- Trainer, F.W. and J.E. Eddy. 1964. A periscope for the study of borehole walls, and its use in groundwater studies in Niagara County, New York. *Geol. Sur. Res., USGS Professional Paper 501D*, p. 203.
- Verruijt, A. 1969. Elastic storage of aquifers. In *Flow through Porous Media*, edited by R.J.M. De Wiest, pp. 331-376. New York: Academic Press.
- Verruijt, A. 1970. *Theory of Groundwater Flow*. New York: Gordon and Breach Science Publishers.
- Warren, J.E. and H.S. Price. 1961. The behaviour of naturally fractured reservoirs. *J. Soc. Petrol. Eng.* 3(3):245-255.
- Warren, J.E. and P.J. Root. 1963. The behaviour of naturally fractured reservoirs. *Trans. AIME* 228:245.
- Weeks, L.J., Consulting Geologist. 1965. *Geological Map of the Province of Nova Scotia*. Nova Scotia Department of Mines, Halifax.
- Wilkinson, W.M. 1953. Fracturing in Spraberry Reservoir - West Texas. *Bull. Am. Assoc. Petrol. Geol.* 37:250.
- Wilson, C.R. and P.A. Witherspoon. 1970. An Investigation of Laminar Flow in Fractured Rocks. *Geotechnical Report No. 70-6*, University of California, Berkeley.
- Witherspoon, P.A. et al. 1974. *Investigation of Fluid Injection in Fractured Rock and Effect on Stress Distribution*. Annual Report for period March 13, 1973, through June 12, 1974, to United States Geological Survey under Contract 14-08-001-12727, ARPA Order No. 1648.
- Wolff, R.G. 1970. Relationship between horizontal strain near a well and reverse water level fluctuation. *Water Resources Res.* 6(6):1721-1728.
- Zienkiewicz, O.C. 1971. *The Finite Element Method in Engineering Science*. London: McGraw-Hill.

Proposed Modification of Inflatable Packer Assembly for Determining the Permeability Profile of a Well

Parizek and Siddiqui (1970) have demonstrated the importance of determining at what point the main producing fractures intersect the well in fractured rock aquifers. This knowledge of the permeability profile of a well is essential to a detailed interpretation of the rate of drawdown in a pumping well, especially for wells that can only sustain a low pumping rate and where the water is obtained from only a few fractures (i.e., in crystalline and metamorphic rocks). In general, determination of the distribution of fractures in a well requires either television camera logging or caliper logging in conjunction with an injection test program. This sort of a program is both expensive and time consuming.

The inflatable packer assembly described by Gale and Welhan (1975b) can be modified to provide a rapid and inexpensive measure of the permeability profile. This modification is shown in Figure A-1. Using the upper and lower packers of a double packer assembly, the injection pipe between the packers is replaced by a 10- to 15-ft highly inflatable packer, about 1.5 in. in diameter. Each length of the well is tested by first inflating the upper and lower packers and seating them in place. The pressure in what is now the injection cavity can be measured with a pressure transducer or with a pressure gauge connected to a small-diameter plastic tube that opens in the injection cavity. The small central packer is now inflated with the rate being controlled in order to maintain a constant water pressure in the injection cavity. For a 6-in. well with a 1.5-in. central packer, and a 10-ft packer interval, approximately 10 Imperial gallons would be available for the injection test. The test uses the water in the well and thus the only equipment needed is the double packer assembly, a compressed air tank, and a water pressure measuring system.

A simple laboratory program would be appropriate to familiarize the operator with the method of controlling the water pressure with air pressure in the packer. To prevent differential expansion of the central packer from sealing off parts of the borehole, a small-diameter rod should be attached to the outside of the central packer, thus ensuring hydraulic connection along the entire length of the injection cavity with the central packer completely expanded.

It should also be noted that when the air pressure in the packer is released, a small pumping test would be performed as the water moves back into the injection cavity.

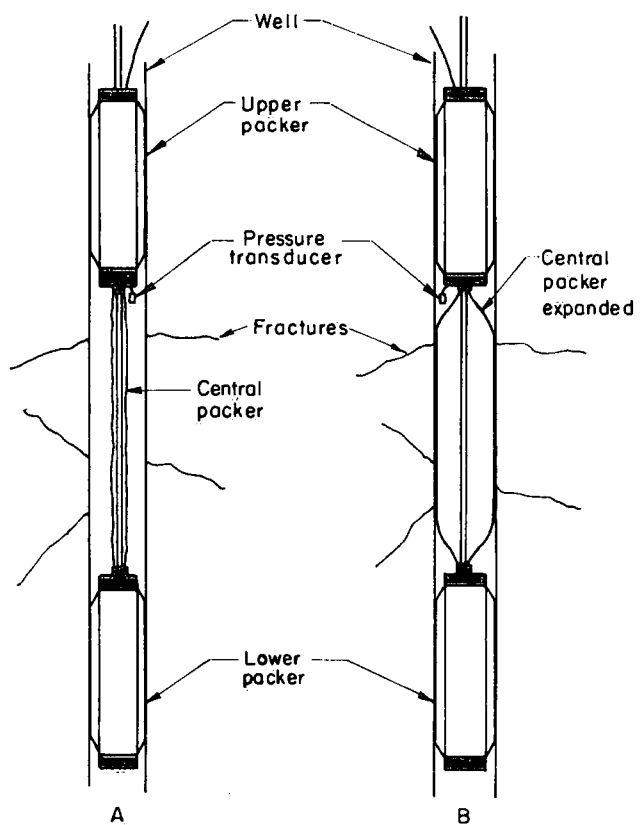


Figure A-1. Double packer assembly modified for permeability profile measurements:
 A - packer in place and
 B - central packer expanded.

Environment Canada Library, Burlington



3 9055 1017 3064 5